



ScuDo
Scuola di Dottorato - Doctoral School
WHAT YOU ARE, TAKES YOU FAR



Doctoral Dissertation
Doctoral Program in Metrology (32nd cycle)

Speed of Sound Measurements of liquid methane at cryogenic temperature

Giuseppe Cavuoto

* * * * *

Supervisors

Dr. Simona Lago, Supervisor
Prof. Candido Pirri, Co-supervisor

Politecnico di Torino

This thesis is licensed under a Creative Commons License, Attribution - Noncommercial-NoDerivative Works 4.0 International: see www.creativecommons.org. The text may be reproduced for non-commercial purposes, provided that credit is given to the original author.

I hereby declare that the contents and organisation of this dissertation constitute my own original work and does not compromise in any way the rights of third parties, including those relating to the security of personal data.



.....
Giuseppe Cavuoto
Turin, November 7, 2019

Summary

This thesis reports speed of sound experimental measurements in liquid methane (CH_4) along five isotherms, in the temperature range of (130 and 162) K, and for pressures up to 10 MPa. A dedicated experimental apparatus, custom-designed for accurate speed of sound measurement at cryogenic temperatures and high pressures, has been developed and the *double pulse-echo* technique has been adopted. In order to characterize this new apparatus and its performance, experimental results have been compared with speed of sound values of liquid methane available in literature. A further comparison has been made between the experimental measurements and the speed of sound values obtained using the reference equation of state of methane of Setzmann and Wagner, as well as the GERG-2008 model. The relative expanded uncertainty ($k=2$) associated to the obtained results is in the order of 0.4 %, mainly influenced by the repeatability of the measurements. Finally, density measurements of two different multi-component LNG mixtures along four isotherms (100, 120, 140 and 160) K and for pressures up to 10 MPa have been reported. Then, the obtained results, with an uncertainty of about 0.04 %, have been compared with the predicted values, calculated by using four different equations of state: the COSTALD3 equation of state, the ERKM equation of state, the GERG-2008 model, and the EOS-LNG model.

Acknowledgements

I would like to acknowledge INRIM researchers and technicians for their contribution to the design and development of the experimental apparatus that has been produced in this work. I would also like to thank Prof. Dr.-Ing Markus Richter and all the researches of the Department of Thermodynamics of Ruhr-Universität Bochum, Germany, for giving me the opportunity to carry out density measurements using the special magnetic-suspension single-sinker densimeter, developed by their University.

*"Ai miei fratelli, che ci sono stati e che
ci saranno sempre .*

*A mia sorella, che porta il buonumore
ovunque vada e che è capace di farmi
ridere anche nei giorni più grigi.*

*A mio padre, che mi ha trasmesso il
dono più grande: la curiosità.*

*A mia madre, che mi ha insegnato che
non esistono sfide troppo grandi e,
soprattutto, che vivere inseguendo le
aspirazioni è infinitamente meglio che
aspirare inseguendo la vita."*

Contents

1	Introduction to LNG flow rate measurements	5
2	Historical Background of methane measurements	11
3	Equations Of State	15
3.1	The Equations of State classification	15
3.2	Cubic Equations	17
3.3	Equation of State for pure Methane by Setzmann and Wagner	19
3.4	GERG-2008 model for Natural Gas	26
4	Speed of Sound and Thermodynamical properties of fluids	29
5	Speed of Sound Measurement experimental methods	35
5.1	Steady-state techniques	35
5.1.1	Spherical resonators	36
5.1.2	Ultrasonic interferometers	37
5.2	Transient techniques. Single pulse method or multiple pulse	38
5.2.1	Single and multiple pulse-echo technique	40
6	The <i>double pulse-echo</i> technique	43
6.1	Time of flight measurement	45
6.2	Acoustic path determination	48
7	State of the art of Speed of Sound Measurements of Liquid Methane	51
7.1	First investigations of liquid methane	52
7.2	Accurate measurements at cryogenic temperatures	53
8	Experimental Apparatus	61
8.1	The ultrasonic cell	61
8.2	Thermostatting system	63
8.3	Experimental apparatus and procedure	72

9 Results and comments	75
9.1 Uncertainty analysis	76
9.2 Comparison of experimental SoS values to available data	78
9.3 Comparison of the results with equations of state predictions	82
10 Density measurements of LNG mixtures	87
10.1 Density measurement technique	88
10.2 Experimental apparatus	90
10.3 Pressure measurements	91
10.4 Temperature measurements	92
10.5 Filling procedure	93
10.6 Uncertainty budget	94
10.7 Preliminary results and comments	95
Tables of experimental speed of sound measurements	103
Technical drawings	113
Bibliography	117

Introduction

This work describes the realization of an innovative experimental apparatus, specifically developed to measure the speed of sound in liquid methane at cryogenic temperature up to high pressure.

Since methane is the main component of liquefied natural gases (LNG), accounting for more than 80 % of the average content of LNG mixtures, the determination of methane thermodynamic properties impacts on calculations adopted in the research and development of sustainable energy and energy transport. At the same time, accurate transfer sensors like the one here described and, specially conceived for the monitoring of thermodynamic properties, are widely demanded by LNG industry. Methane is in fact the best candidate to be used as a reference fluid to calibrate commercial measuring instruments involved in storage and transport processes of LNG (e.g. densimeters and flowmeters). Nowadays, LNG is one of the most promising sources of energy in terms of environmental sustainability, mainly because a transition to the use of LNG as a substitute for heavy oil and diesel fuel can lead to the reduction of greenhouse gases, nitrogen oxides, sulphur dioxide and fine dusts emissions. Moreover, the carbon footprint of natural gases is lower than of other fossil fuels or coal. This makes them, along with liquefied biogas (LBG), one of the best and most encouraging choices to achieve the goal of meeting the increasingly strict regulations on the reduction of emissions into the atmosphere [1]. In addition to the positive environmental impact, the increase of natural gas use in industrial processes also leads to significant advantages in energy transport. Being colourless, odourless, non-toxic and non-corrosive, LNG can be handled under safer conditions throughout the whole transfer chain. Moreover, when liquefied, natural gas occupies a volume of about six hundred times smaller than the volume it occupies in gaseous phase. This property allows to store and transport large amount of LNG in relatively small spaces. Within this scenario, the European Association of National Metrology Institutes (EURAMET), in the frame of the European Metrology Programme for Innovation and Research (EMPIR), focused their attention on the characterization of LNG to meet the demand for new and accurate measurements of its thermodynamic properties for supporting the custody transfer process. The realization of the new experimental apparatus for speed of sound measurements of methane at cryogenic temperatures is therefore a part of this project. A further aim of this Joint Research Protocol was to provide an instrument capable of delivering measurements with a relative uncertainty of a few parts per thousand, that is about one order of magnitude smaller than that achievable with any industrial instruments currently on the market. This, together with the difficulty of working at extreme temperature conditions, increases the level of complexity of the desired measurements still further.

The newly implemented experimental apparatus implements on the *double pulse-echo* technique, which is a well-established method that is particularly suited for

speed of sound measurements of fluids in liquid phase at extreme thermodynamic conditions. Speed of sound in liquid methane has been measured for temperatures between (130 and 162) K and for pressures up to 10 MPa, with an expanded relative uncertainty of 0.42 % ($k = 2$). The obtained results have been compared with the values predicted by the reference equation of state of methane and with those of GERG-2008 model, which is the ISO standard for the calculation of thermodynamic properties of LNG. These comparisons have shown that experimental speed of sound are in good agreement with the predicted values for temperatures above 150 K, while they are not consistent for temperatures below 140 K. Particularly, at a temperature of 130 K, where no other experimental values of speed of sound are available in literature, deviations are larger than 1.5 %. A further comparison was made with the speed of sound data available over the investigated temperature and pressure range, showing that the experimental results are in good agreement with all available data, except those published by Van Itterbeek in 1967. Since all reference equations for methane are based on these last measurements, the disagreement between the obtained results and those predicted by the equations can be explained.

This work includes also the results of density measurements of an LNG mixture of methane and isopentane carried out using a special densimeter which works with a magnetic suspension, manufactured at the University of Bochum (Germany) and specifically designed for measurements at cryogenic temperatures.

Chapter 1 describes the practical applications that can be achieved by employing the acoustic sensor used in this work for speed of sound measurements. In particular, it illustrates how it can be used to provide reference values for calibrating, directly on-line, the ultrasonic flowmeters used in the LNG transfer. Chapter 2 provides a brief overview on the evolution in the study of acoustical phenomena in history, from the first rudimentary observations carried out by the ancient Greeks in the 6th century B.C., up to the first experimental measurements of speed of sound in water, carried out by Colladon and Sturm in 1862. A description of the most common physical principles used for speed of sound measurements is presented in Chapter 5. Chapter 6 describes in detail the double *pulse-echo* technique adopted in this work, as well as the basic principles of the most commonly used methods for measuring the speed of sound in both gases and liquids. Chapter 3 contains a theoretical discussion that describes the role played by speed of sound measurements when equations of state are developed. Subsequently, Chapter 4 provides the today's well established mathematical methods for the determination of thermodynamic properties by using accurate speed of sound measurements. Chapter 7 lists and describes some of the most important experiments carried out in the second half of the twentieth century, by which the speed of sound of methane was measured at temperatures below 190.6 K, its critical temperature.

In Chapter 8, the new experimental apparatus, developed during this work, is described, focusing on the ultrasonic cell, which is the core element of the entire instrument, describing the temperature control system and, finally, showing the experimental procedures adopted during the measurements to ensure temperature and pressure stability, as well as to ensure safe working conditions during the experiment.

Chapter 9 provides a discussion on the uncertainty associated with the experimental measurements obtained by using the experimental apparatus described above, as well as a discussion on the experimental results. Finally, Chapter 10 describes the work I have done during my foreign research period at the Ruhr-Universität, in Bochum, Germany, during 2018. This research has been focused on density measurements of different multi-component LNG mixtures. Although this chapter may seem slightly disconnected from the rest of this work, I decided to add it anyway, to provide a more complete description of the activities I carried out during my Doctoral course. Therefore, this chapter describes the working principle of the special densimeter used for the LNG mixture density measurement, as well as the preliminary results obtained for a mixture of methane and isopentane.

Chapter 1

Introduction to LNG flow rate measurements

The development of the new experimental apparatus has been characterized by high complexity and has required considerable effort to make it working. In fact, its realization has required many tests both in designing and in solving the various problems encountered during its working time. The aim of this project was in fact to realize an instrument capable of carrying out accurate speed of sound measurements at high pressures and extreme temperatures.

In general, under these conditions it is difficult to obtain accurate measurements from a metrological point of view, since in order to minimize the sources of uncertainties, especially those relating to the determination of the temperature to be associated to experimental measurements, it is necessary to introduce additional precautions compared to what normally happens when measuring thermodynamic properties at intermediate temperatures and at low pressures. When the entire system is assembled, it is light enough (the entire apparatus weighs less than 30 kg) and compact to be inserted into a vacuum chamber less than a metre high, as shown in Figure 1.1. The speed of sound sensor, is compact and a relatively easy to handle instrument. Its dimensions, in fact, do not exceed 15 cm. In addition, it does not require special precautions or complex procedures to operate. Basically, it is sufficient to have a function generator connected to the acoustic transducer, in order to excite it, and a digital oscilloscope to sample the signals obtained as a response to the emission of the ultrasonic wave. This ease of use and transport makes it particularly suitable for in situ measurements. In particular, the advantage of such a sensor is that it is possible to carry out on-line measurements of speed of sound, when mounted on transport equipments and vehicles involved during the LNG custody transfer processes, such as pipelines, LNG carriers and LNG trucks: in general, in the nearby of the LNG power plant facilities. Measuring the speed of sound of LNGs, while they are transported and fed into the distribution network, has significant advantages in determining some of the thermodynamic properties



Figure 1.1: Vacuum chamber used during the experiment.

that are of primary interest both in terms of industry and cost efficiency. According to the *GIIGNL–LNG Custody Transfer Handbook, v. 5.00 (2017)*, the transferred energy due to the loading of a certain amount of natural gas from production facilities into LNG carriers is calculated as follows:

$$E = V \cdot \rho \cdot G - E_{\text{disp}} \pm E_{\text{ER}}, \quad (1.1)$$

where E is the total net energy transferred from the loading facilities to the LNG carrier, from the LNG carrier to the unloading facilities or from one LNG carrier to another LNG carrier, V is the volume of LNG loaded or unloaded, ρ is the density of LNG loaded or unloaded, G is the the gross calorific value of the LNG loaded or unloaded, E_{disp} is the net energy of the displaced gas and E_{ER} is the energy of the gas consumed in the LNG carrier's engine room. While for the measurement of loaded or unloaded LNG volume sensors are typically used for the determination of the fluid level in the LNG tankers (by using suitable tank tables), thus measuring the volume before and after the loading or discharging operations, for density and gross calorific value it is essential to know the average composition of the LNG, which can be obtained by continuous or discontinuous sampling of LNG in the LNG transfer lines between the LNG custody transfer operators or by gas chromatographic analysis. In this way, by measuring temperature and pressure inside the tanks that contain natural gas, it is possible to obtain, by means of special mathematical models, both ρ and G . An alternative method for calculating the energy transferred during the distribution of the LNG is to use in line LNG flow

meters (e.g. ultrasonic flow meters or Coriolis) to determine the volume transferred, instead of using the cargo tank tables of the LNG carrier.

For Coriolis meters, which measure mass flow directly, no density calculations are needed, but they are affected by size and pressure drop limitations. These measurements also depend on the tube shape, on elastic properties of the materials used to manufacture Coriolis pipes and, in general, on the specific thermodynamic conditions involved during the measurement.

On the other hand, ultrasonic meters have no size or pressure drop limitations, but density and compositions calculations are needed. The operating principle of these instruments is illustrated in figure 1.2 Two (or more) transducers, acting as both

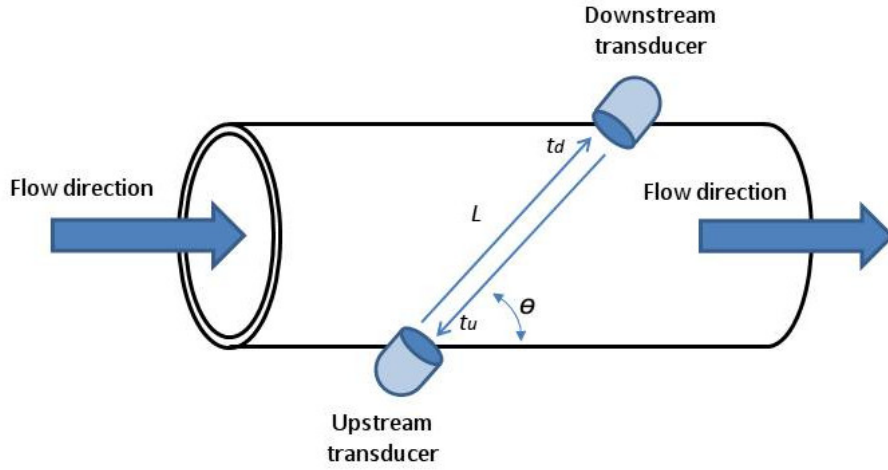


Figure 1.2: Ultrasonic flowmeter diagram.

transmitter and receiver, are placed on the pipe wall, one on the upstream and the other on the downstream. The time for acoustic waves to travel from the upstream transducer to the downstream transducer t_d is shorter than the time it requires for the same waves to travel from the downstream to the upstream t_u . The larger the difference, the higher the flow velocity. Using these two transit times, the distance between receiving and transmitting transducers L and the inclination angle θ , both the averaged flow velocity v and the speed of sound w can be calculated by using the following set of equations:

$$\begin{cases} w - v \cos \theta = \frac{L}{t_u} \\ w + v \cos \theta = \frac{L}{t_d} \end{cases} \quad (1.2)$$

Then, by adding and subtracting the above equations, v can be calculated as

$$v = \frac{L}{2 \cos \theta} \frac{t_u - t_d}{t_u t_d}, \quad (1.3)$$

and w as

$$w = \frac{L}{2} \frac{t_u + t_d}{t_u t_d}. \quad (1.4)$$

The ultrasonic flowmeters are calibrated determining $L/2$ from expression 1.4 at ambient condition and using a reference fluid with known speed of sound, usually pure water. The value $L/2$ is uploaded to flowmeters memory and then corrected for temperature and pressure. The sensor developed in this work will allow to eliminate the term $L/2$ from equation 1.3 and 1.4, allowing the on-line calibration of the ultrasonic flowmeter while operating at cryogenic temperature. In fact, after characterizing the ultrasonic cell in laboratory conditions, it is then possible to easily use it on-line, connecting it directly on the pipeline by using a fitting pipe, in the nearby of the ultrasonic flowmetr sensors (see Figure 1.3).

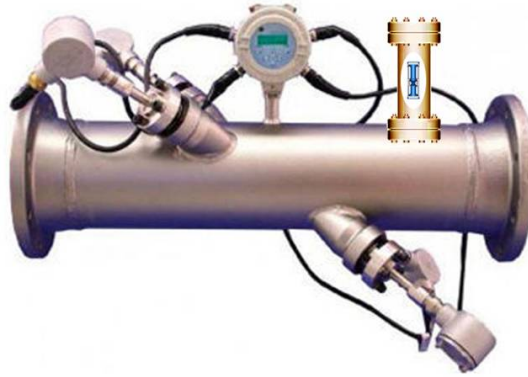


Figure 1.3: Configuration for the calibration of an ultrasonic flowmeter by using the ultrasonic cell.

The important improvement of this calibration is the capability to directly measure the speed of the sound of the LNG flowing in the pipe, in a portion of the system where the fluid is already at rest. In addition, this method also allows to measure the speed of sound w without any prior knowledge of the LNG mixture composition. This simplification results in a significant improvement of the uncertainty associated with the LNG flow rate measurements. In fact, while with the current ultrasonic flowmeters the speed of sound in the fluid can be calculated with an uncertainty of about a few percent [2], using the ultrasonic cell it is possible to achieve uncertainties of a few parts per thousand, therefore with an improvement of about one order of magnitude.

Chapter 2

Historical Background of methane measurements

Establishing the physical properties of acoustic phenomena has been a problem that has involved scientists over long time. In particular, the physical description of propagating acoustic waves and their speed was a challenge that has involved a large number of studies and experimental observations.

One of the first documents go back to the 6th century B.C. when some early studies on acoustics have been carried out by the Pythagorean school [3]. In fact, it dates back to that period the discovery of some relationships between length, weight and tension of a vibrating string and the pitch, or frequency, of the sound heard by the ear. However, it was necessary to arrive at the beginning of the 17th century to begin to investigate the physical aspects of acoustics. One of the first topics to be debated was the necessity of a medium for sound transmission. In 1645 Otto von Guericke devised a special apparatus capable to ring a bell inside a vacuum chamber [4]. With this experiment he definitively demonstrated that a material medium is indispensable for the propagation of sound. In the same century, other observations on the quantitative relationships between length and frequency of vibration of a strings were obtained by Galileo Galilei [5] and Marin Mersenne [6]. In particular, Mersenne, around 1636 carried out the first measurement of speed of sound in air [7], by measuring the time delay between the emission of a sound and its echo obtained from a reflecting surface at a known distance. Similarly, in the same years, Pierre Gassendi succeeded in measuring the interval of time between the instants in which the appearing of the lightning and the hearing of the burst from a distant rifle [7]. In this way, he obtained a sound velocity value of approximately 478.4 m s^{-1} , while Mersenne's was about 450 m s^{-1} . These values were both too high but Borelli and Viviani, in 1650, obtained a much better value, measuring a sound speed of 350 m s^{-1} , repeating the same type of experiment.

In 1687 Isaac Newton described in the *Principia Mathematica* a first mathematical treatise that led to the formalization of the physics of sound and the propagation

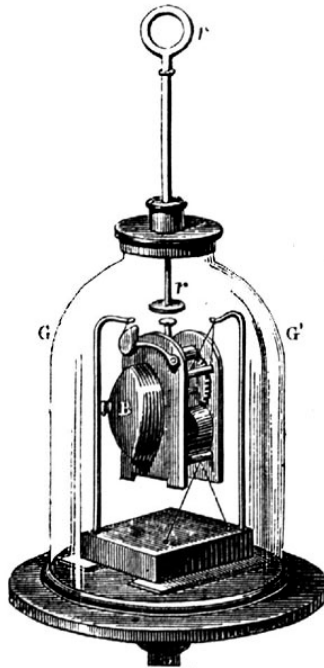


Figure 2.1: Sketch of the apparatus designed by von Guericke [4]

of motion through fluids. This is considered the birth of the first real theory on sound. He discovered that the propagation of sound through any fluid depends only on measurable physical properties, such as the elasticity and density, of the medium through which it propagates. Moreover, he was also able to calculate the speed of sound in air using only mathematical assumptions and obtaining a value of 298 m s^{-1} . The difference between this result and the value obtained from empirical observations, 348 m s^{-1} , was mainly due to the incorrect assumption that the air temperature during sound propagation remained constant. This error was addressed and solved by Laplace [8]. He observed that sound waves generate a series of compressions and rarefactions within the air. Causing a local variation in temperature so that, for example, as a result of compression, a certain amount of heat is released and absorbed immediately after by the next rarefaction. Because of the rapidity of this process, the heat is released and reabsorbed much faster than the time needed to be dissipated. Thus, the temperature and pressure increase locally approximately adiabatically and the speed of sound results larger than that one Newton had predicted, considering isothermal compressions.

During the eighteenth century, a number of qualitative experiments were carried out investigating the propagation of sound in air and water. At that time it was still debated whether water owned an elasticity. Jean-Antoine Nollet, in 1743, was the first who measured the propagation of sound in the waters of the Seine. Then, modifying the experiment in such a way that it could be repeated in the laboratory,

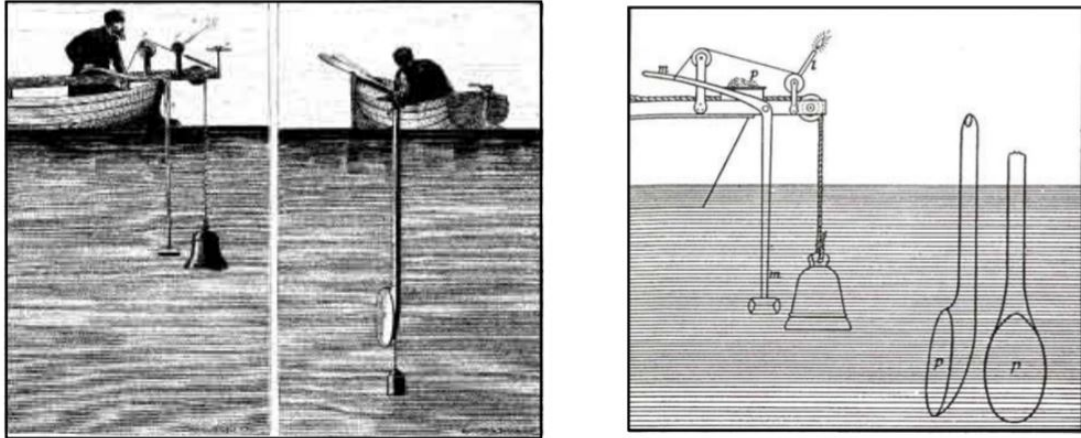


Figure 2.2: Illustration and schematics of Colladon and Sturm's 1862 experiment in Lake Geneva. J. D. Colladon, *Souvenirs et Memoires*, (Albert-Schuchardt, Geneva, 1893). NOAA Photo Library.

he purified the water from the air, concluding that it was not this that led the sound but, actually, the water itself. For the determination of the speed of sound in water it was necessary to wait until the beginning of the 19th century with the experience of Colladon and Sturm in Geneva Lake [9]. In their experiment, an underwater bell was struck at the same time as some gunpowder was ignited on a first boat. The sound of the bell and the flash of the gunpowder were observed about 16 km away on a second boat. The time between the flash and the sound reaching the second boat was used to calculate the speed of the sound in the water, finding a value of 1435 m s^{-1} .

However, it was only in the first half of the 20th century that experimental acoustics and related technology were radically renewed. Technological development and introduction of new electrical and electronic equipment allowed sound waves to be generated and revealed more accurately, without changing the theoretical basis that describes acoustic propagation, which is now completely systematized.

Chapter 3

Equations Of State

3.1 The Equations of State classification

The most used mathematical tool for the calculation of the thermodynamic properties of a fluid are the equations of state (EoS), which can be defined as any class of equations that allow to define the thermodynamic state of a system on the basis of the variables pressure p , temperature T and molar volume ν (or density ρ). Moreover, through thermodynamic derivative relationships, it is possible to determine other properties, such as speed of sound, heat capacity, compressibility, entropy, enthalpy, internal energy, and many more. Conversely, from accurate speed of sound measurements, it is possible to improve the predictions of the EoS. For thermodynamic systems a crucial role in the formulation of EoS is played by thermodynamic potentials, expressed in terms of Gibbs, G free energy or Helmholtz free energy, A . In general, for example considering the Helmholtz free energy, it is possible to define A as $A(T, p) = A^*(T, p) + A_{res}(T, p)$, where the term $A^*(T, p)$ represents the properties of the ideal gas, while the term A_{res} represents the deviations of the real gas from the ideal conditions. Then the following equation can be obtained for the residual term A_{res} :

$$A_{res}(T, p) = A(T, p) - A^*(T, p) = \int_{\nu}^{\infty} \left(p - \frac{RT}{V} \right) dV - RT \ln \frac{pV}{RT}, \quad (3.1)$$

where A^* is the Helmholtz free energy of the ideal gas obtained under the same conditions of temperature and pressure as the actual Helmholtz free energy A , R is the gas constant and V is the volume occupied by the fluid.

Similarly, it is possible to formulate any equation of state which expresses the residual value of a physical quantity as a function of temperature and pressure (or

volume). Also in the case of the residual Helmholtz free energy we have, for example, the equation corresponding to the van der Waals equation of state, which is described in the next section:

$$A(T, p) - A^*(T, p) = RT \ln \frac{\nu - b}{\nu} - \frac{a}{\nu}, \quad (3.2)$$

where a is a parameter which takes into account the attractive forces between molecules, b is the covolume occupied by the molecules and $\nu = V/M$ is the molar volume of a fluid having a mass M .

An equation of state can also be used to predict the phase equilibria of both homogeneous and heterogeneous systems [10], to correlate experimental data as well as to predict values of thermodynamic properties in regions where experimental measurements do not exist yet, or where these measurements are particularly difficult to achieve. Ideally a model should be able to predict the phase equilibrium and whichever thermodynamic properties of a system, under any temperature and pressure conditions, on the basis of some particularly advantageous and easily measurable physical properties. Unfortunately, such an equation of state does not exist and it is not possible to use a single model to predict successfully the characteristics of a fluid in any temperature and pressure points. Because of this, there are several equations of state that are used according to the type of fluid to be examined, the temperature and pressure ranges considered and, in general, the physical properties to be measured.

These can be classified according to the degree of polynomial function used to formulate them, defining cubic and non-cubic state equations. A second classification is related to the nature of the interactions which take place within the system. In this case the equations of state can be divided into three groups: empirical equations, theoretical equations and semi-empirical (or semi-empirical) equations [11]. The empirical equations are formulated by means of correlation with the experimental data. What is obtained in this way is an arbitrary function, usually having a very large number of parameters. These functions are strictly dependent on the experimental data used for their formulation and can be applied only in the pressure and temperature ranges where these data were obtained. On the contrary, theoretical equations are mathematical models that are based on molecular interaction models. Since they are not related to specific experimental data, they can be applied, in a much more general way, to describe the thermodynamic properties of entire families of chemical compounds [12]. The disadvantage of this type of equation is that they are strongly dependent on the type of intermolecular interaction model used to build them. In fact, since these models are only an approximation of the real behavior of a pure fluid as well as of a mixture, it is possible that also the values provided by the equation can diverge considerably from the real values of the physical system to be modelled. Therefore, in most cases it is preferable to use

equations of state implemented by combining the two approaches (semi-empirical equations), starting from theoretical considerations and modifying the behaviour of the model to fit available accurate experimental data. From these observations, the equations of state can be classified into three different groups [13], according to the types of chemical and physical phenomena which are taken into account in their formulation. Thus, it is possible to obtain cubic equations of state (e.g. van der Waals equation of state), where contributions of attraction and repulsion of the fluid particles are included, then, equations based on the evaluation of molecular phenomena and, finally, virial equations of state.

3.2 Cubic Equations

The van der Waals equation of state, proposed in 1873, was the first successful attempt able to predict the presence of a liquid-vapour phase equilibrium. This can be rewritten by deriving the equation 3.2 with respect to the volume, getting:

$$p = \frac{RT}{\nu - b} - \frac{a}{\nu^2}, \quad (3.3)$$

where the following relationship between variation of Helmholtz free energy and molar entropy s has been applied has been applied:

$$dA_H = -sdT - pd\nu. \quad (3.4)$$

The same equation is often expressed in terms of the compressibility factor $z = \frac{p\nu}{RT}$, as follows:

$$z = \frac{\nu}{\nu - b} - \frac{a}{RT\nu}. \quad (3.5)$$

The peculiarity of this equation is that it could be interpreted as the sum of two terms, $z = z^{rep} + z^{att}$. The first, $\frac{\nu}{\nu - b}$ which represents the repulsive forces, and the second, $\frac{a}{RT\nu}$, which takes into account the attractive forces. Unfortunately, even considering the importance of this equation, for which van der Waals received the Nobel Prize in 1910, the author himself observed that it was insufficiently accurate, especially in the proximity of critical points. For this reason many changes have been made over the years to the original equation. Most of these changes concern the attractive term, leaving the repulsive term largely unaltered. Table 3.1 lists the most significant of those equations, sorted by their authors and the attractive terms which appear within each equation.

Authors	Attractive terms
van der Waals	$\frac{a}{RT\nu}$
Redlich-Kwong (1949)	$\frac{a}{(\nu+b)TR^{3/2}}$
Soave (1972)	$\frac{a(T)}{(\nu+b)RT}$
Peng-Robinson (1976)	$\frac{\nu a(T)}{[\nu(\nu+b)+b(\nu-b)]RT}$
Fuller (1976)	$\frac{a(T)}{(\nu+cb)RT}$
Schmidt-Wenzel (1980)	$\frac{\nu a(T)}{(\nu^2+ub\nu+wb^2)RT}$
Harmens-Knapp (1980)	$\frac{\nu a(T)}{[\nu^2+\nu cb-(c-1)b^2]RT}$
Patel-Teja (1982)	$\frac{\nu a(T)}{[\nu(\nu+b)+c(\nu-b)]RT}$
Peneloux (1982)	$\frac{a(T)}{(\nu+t)(\nu+b+2t)}^a$
Adachi (1987)	$\frac{\nu a(T)[\nu-c(T)]}{(\nu-b)[\nu-d(T)][\nu+e(T)]RT}$
Treble-Bishnoi (1987)	$\frac{\nu a(T)}{[\nu^2+(b+c)\nu-(bc+d^2)]RT}$

Table 3.1: List of the attractives terms used within the most significant cubic equations. ^a Example of Peneloux model applied to SRK equation.

Of all the equations derived from the van der Waals equation, it is worth mentioning the Redlich and Kwong equation [14]. In this model the dependence on temperature and volume of the attractive term was changed in order to improve the prediction of the compressibility coefficient. Nevertheless, the values obtained for vapour pressure and density of liquids were still not very accurate. The SKR equation (Soave-Redlich-Kwong) [15] introduced a generic term $a(T)$ 3.6 for the temperature dependence, which depends on critical temperature T_c , critical pressure p_c , reduced temperature $T_r = T/T_c$, and a parameter m , which is related to the acentric factor.

$$a(T) = 0.4274 \frac{R^2 T_c^2}{p_c} \left[1 + m(1 - T_r^{0.5}) \right]^2 \quad (3.6)$$

Over the years, a number of forms were proposed for the term $a(T)$, including the one introduced in the PR equation (Peng-Robinson) 3.7

$$a(T) = 0.42724 \frac{R^2 T_c^2}{p_c} \left[1 + (0.37464 + 1.5422\omega - 0.26922\omega^2)(1 - T_r^{0.5}) \right]^2 \quad (3.7)$$

with ω is used for the acentric factor.

The SRK and PR equations are very common, mainly because of their simplicity of use, resulting from the presence of a limited number of parameters. However, these are not yet sufficiently accurate for many industrial and laboratory uses, since they provide, for example, the same compressibility factor value for all substances as well as they fail to predict density values of fluids in liquid phase. To solve the problem related to the compressibility factor, various equations were introduced. They presented, rather than just parameters a and b , three (e.g. Fuller [16], Harmens and Knapp [17], Schmidt and Wenzel [18], Patel and Teja [19]), four (e.g. Trebble and Bishnoi [20]) or five (e.g. Adachi [21]) parameters.

To improve the models' reliability in describing the volumetric properties of saturated liquids, Peneloux [22] proposed a method in which the molar volume was shifted by a quantity of t , thus replacing the values ν and b with the values $\nu + t$ and $b + t$. The advantage of this correction is that it can be applied with good results to all equations derived from the van der Waals equation.

Finally, cubic equations are widely used because, although they are approximated models, they generally succeed in describing the properties of fluids adequately. In order to improve its validity even further, a large number of corrections for the repulsive term have also been introduced. However, most of the results obtained in this way lead to equations that are no longer cubic.

3.3 Equation of State for pure Methane by Setzmann and Wagner

Today the most accurate description of the thermodynamic behavior of methane in its different phases is expressed by the equation of state explicit in the free Helmholtz energy implemented by Setzmann and Wagner in 1991 [23]. Because of the great importance of methane in many aspects of chemistry, thermodynamics and engineering a great number of experiments have been carried out to measure its properties. As a result, the availability of new experimental data has encouraged the development of many equations of state since the early 1970s [24, 25, 26, 27, 28, 29, 30, 31, 32, 33, 34]. However, all these equations are based mainly on measurements (ρ, p, T) carried out by Goodwin and Prydz [35], Douslin *et al* [36],

and Cheng [37]. In fact, after new (ρ, p, T) investigations carried out by Kleinrahm and Wagner [38] and Kleinrahm *et al.* [39, 40], it was observed that Goodwin's experimental results showed systematic deviations from the most recent data.

In particular, the density values had deviations of up to 0.2 % from the the new state-of-the-art (ρ, p, T) data. In addition, all the equations previously developed for methane were affected by the following issues:

- Were unsuccessful in reproducing the experimental data within their uncertainty
- Had a limited validity temperature and pressure ranges
- Had a complex mathematical description not easy to use
- Did not use the International Temperature Scale of 1990 (ITS-90)

In 1989, Setzmann and Wagner [41] published a new method for improving the structure of empirical thermodynamic correlation equations. Thanks to this optimization procedure, together with the use of the *multi-property fitting* technique, the new equation was capable to represent experimental data reducing the complexity of its mathematical description.

The Setzmann and Wagner's equation represents thermodynamic properties of methane in the temperature range from (90.69 to 625) K at pressures up to 1000 MPa. Fundamental equation explicit in the Helmholtz energy A , are expressed as a function of density, ρ and temperature, T . Specifically, it is possible to define the dimensionless specific Helmholtz energy $\Phi = A/(RT)$ as the sum of the ideal gas part, Φ^o , and the residual part, Φ^r :

$$\frac{A(\delta, \tau)}{RT} = \Phi(\delta, \tau) = \Phi^o(\delta, \tau) + \Phi^r(\delta, \tau), \quad (3.8)$$

where $\delta = \rho/\rho_c$ is the reduced pressure and $\tau = T_c/T$ is the inverse reduced temperature, with $\rho_c = 162.66 \text{ kg/m}^3$ and $T_c = 190.564 \text{ K}$ that are the critical density and temperature, respectively. The ideal gas part of the specific Helmholtz function, A_o , is given, when the ideal gas heat capacity c_p^o is available, by the following equation:

$$A_o = \int_{T_o}^T c_p^o dT + h_o - RT - T \int_{T_o}^T \frac{c_p^o - R}{T} dT - RT \ln(\rho/\rho_o) - T s_o, \quad (3.9)$$

where ρ_o , h_o , s_o are reference density, reference enthalpy and reference entropy, respectively. Starting from equation 3.9, the dimensionless specific ideal gas part, $\Phi^o(\delta, \tau)$ can be expressed as

$$\Phi^o(\delta, \tau) = \ln(\delta) + a_1 + a_2\tau + a_3\ln(\tau) + \sum_{i=4}^8 a_i(1 - e^{-i\Theta_i^c\tau}), \quad (3.10)$$

where the values of the coefficients a_i and $\Theta_i^c = \Theta/T_c$ are given in Table 3.2.

i	a_i	Θ_i^c
1	9.91243972	-
2	- 6.33270087	-
3	3.0016	-
4	0.008449	3.40043240
5	4.6942	10.26951575
6	3.4865	20.43932747
7	1.6572	29.93744884
8	1.4115	79.13351945

Table 3.2: Numerical values of the coefficients of the ideal gas part of the dimensionless specific Helmholtz function

The residual part of the dimensionless specific Helmholtz function, $\Phi = A^r(\delta, \tau)/(RT)$, is more complicated than the ideal term and is obtained as

$$\Phi^r = \sum_{i=1}^{13} n_i \delta^{d_i} \tau^{t_i} + \sum_{i=14}^{36} n_i \delta^{d_i} \tau^{t_i} e^{-\delta^{c_i}} + \sum_{i=37}^{40} n_i \delta^{d_i} \tau^{t_i} e^{-\alpha_i(\delta-\Delta_i)^2 - \beta_i(\tau-\gamma_i)^2}, \quad (3.11)$$

where, the coefficients appearing in the three sum terms of equation 3.11 are listed in Table 3.3.

Equations Of State

i	c_i	n_i	d_i	t_i	α_i	β_i	γ_i	Δ_i
1	-	$0.4367901028 \times 10^{-1}$	1	0.5	-	-	-	-
2	-	0.67092362	1	0.5	-	-	-	-
3	-	$-0.1765577859 \times 10^1$	1	1	-	-	-	-
4	-	0.858233024	2	0.5	-	-	-	-
5	-	$-0.1206513052 \times 10^1$	2	1	-	-	-	-
6	-	0.512046722	2	1.5	-	-	-	-
7	-	$-0.4000010791 \times 10^{-3}$	2	4.5	-	-	-	-
8	-	$-0.1247842423 \times 10^{-1}$	3	0	-	-	-	-
9	-	$0.3100269701 \times 10^{-1}$	4	1	-	-	-	-
10	-	$0.1754748522 \times 10^{-2}$	4	3	-	-	-	-
11	-	$-0.3171921605 \times 10^{-5}$	8	1	-	-	-	-
12	-	$-0.2240346840 \times 10^{-5}$	9	3	-	-	-	-
13	-	$0.2947056156 \times 10^{-6}$	10	3	-	-	-	-
14	1	0.183048791	1	0	-	-	-	-
15	1	0.151188368	1	1	-	-	-	-
16	1	-0.428936388	1	2	-	-	-	-
17	1	$0.6894002446 \times 10^{-1}$	2	0	-	-	-	-
18	1	$-0.1408313996 \times 10^{-1}$	4	0	-	-	-	-
19	1	$-0.3063054830 \times 10^{-1}$	5	2	-	-	-	-
20	1	$-0.2969906708 \times 10^{-1}$	6	2	-	-	-	-
21	2	$-0.1932040831 \times 10^{-1}$	1	5	-	-	-	-
22	2	-0.110573996	2	5	-	-	-	-
23	2	$0.9952548995 \times 10^{-1}$	3	5	-	-	-	-
24	2	$0.8548437825 \times 10^{-2}$	4	2	-	-	-	-
25	2	$-0.6150555662 \times 10^{-1}$	4	4	-	-	-	-
26	3	$-0.4291792423 \times 10^{-1}$	3	12	-	-	-	-
27	3	$-0.1813207290 \times 10^{-1}$	5	8	-	-	-	-
28	3	$0.3445904760 \times 10^{-1}$	5	10	-	-	-	-
29	3	$-0.2385919450 \times 10^{-2}$	8	10	-	-	-	-
30	4	$-0.1159094939 \times 10^{-1}$	2	10	-	-	-	-
31	4	$0.6641693602 \times 10^{-1}$	3	14	-	-	-	-
32	4	$-0.2371549590 \times 10^{-1}$	4	12	-	-	-	-
33	4	$-0.3961624905 \times 10^{-1}$	4	18	-	-	-	-
34	4	$-0.1387292044 \times 10^{-1}$	4	22	-	-	-	-
35	4	$0.3389489599 \times 10^{-1}$	5	18	-	-	-	-
36	4	$-0.2927378753 \times 10^{-2}$	6	14	-	-	-	-
37	-	$0.9324799946 \times 10^{-4}$	2	2	20	200	1.07	1
38	-	$-0.6287171518 \times 10^1$	0	0	40	250	1.11	1
39	-	0.1271069467×10^2	0	1	40	250	1.11	1
40	-	$-0.6423953466 \times 10^1$	0	2	40	250	1.11	1

Table 3.3: Numerical values of the coefficients of the residual part of the dimensionless Helmholtz function

Once the form by which the Helmholtz's energy is established, thermodynamic properties of the fluid can be obtained by deriving equation 3.8. For example, speed of sound is derived as

$$\frac{w^2(\delta, \tau)}{RT} = 1 + 2\delta\Phi_{\delta}^r + \delta^2\Phi_{\delta\delta}^r - \frac{(1 + \delta\Phi_{\delta}^r - \delta\tau\Phi_{\delta\tau}^r)^2}{\tau^2(\Phi_{\tau\tau}^o + \Phi_{\tau\tau}^r)}, \quad (3.12)$$

with $R = R_m/M = 0.5182705 \text{ kJ kg}^{-1} \text{ K}^{-1}$, which is the specific gas constant of methane, expressed as the ratio between molar gas constant, R_m , and the molar mass, M . Terms Φ_{ij}^r and Φ_{ij}^o are the partial derivatives of the dimensionless Helmholtz's energy $\Phi(\delta, \tau)$.

$$\Phi_{\delta} = \left[\frac{\partial\Phi}{\partial\delta} \right]_{\tau}, \Phi_{\delta\delta} = \left[\frac{\partial^2\Phi}{\partial\delta^2} \right], \Phi_{\tau} = \left[\frac{\partial\Phi}{\partial\tau} \right]_{\delta}, \Phi_{\tau\tau} = \left[\frac{\partial^2\Phi}{\partial\tau^2} \right] \text{ and } \Phi_{\delta\tau} = \left[\frac{\partial^2\Phi}{\partial\delta\partial\tau} \right] \quad (3.13)$$

There are several experimental measurements of speed of sound in methane. Most of these were obtained between the 1960s and the 1980s. Those selected by Setzmann and Wagner, together with selected experimental data of other thermodynamic properties, have been used to derive the parameters of the equation of state and are show in Figure 3.1, where their distribution in a $T - p$ diagram is plotted. The relationship between the speed of sound and the Helmholtz free energy, expressed in equation 3.12, was used to determine the values of w at the pressures and temperatures of the experimental measurements obtained in this work. In this way it was possible to compare the experimental results with the values predicted by the equation of state.

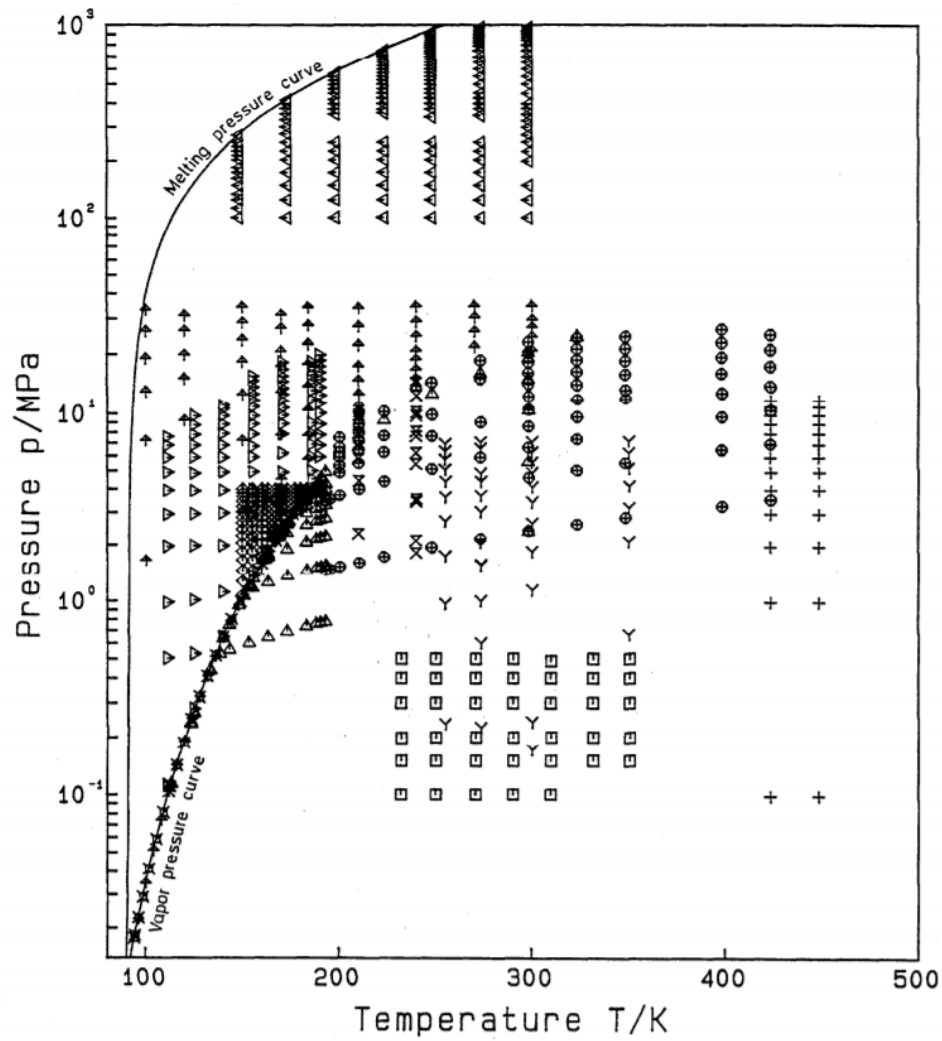


Figure 3.1: $T - p$ distribution speed of sound data used in the formulation of the residual part of the equation of state, Φ^r , as reported in Setzmann and Wagner [23]. Δ Gammon and Douslin [42], \uparrow Straty [43], \triangleright Van Itterbeek *et al.* [44], \diamond Baidakov *et al.* [45], \square Lemming [46], $+$ Terres *et al.* [47], $*$ Van Dael *et al.* [48], \times Straty [49], \triangleleft Kortbeek and Schouten [50], \oplus Sivaraman and Gammon [51], Y Goodwing [52].

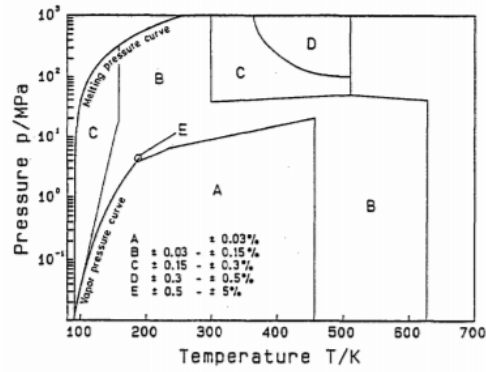


Figure 3.2: Tolerance diagram for speed of sound as reported in [23].

Despite the large number of experimental results of sound velocity in methane, only a few of them were obtained in the range of T and p investigated in this work.

Finally, Figure 3.2 shows the values of the uncertainties associated to each $T-p$ region within the validity range of the equation of state. The uncertainty with which the EoS reproduces the values of speed of sound for temperatures from (130 to 162) K and pressures up to 10 MPa, i.e. the area of the phase diagram investigated, varies from (0.15 to 0.3) %.

3.4 GERG-2008 model for Natural Gas

GERG-2008 model [53] is an equation of state for determining the thermodynamic properties of natural gas mixtures. It is an expanded version of the GERG-2004 model [54] and was developed within the GERG (*Groupe Européen de Recherches Gazières*) project [55] to meet the demand for accurate calculations of properties of natural gas during transport and storage processes. In addition, the equation is intended for use over a wide temperatures and pressures range, for a wide range of mixtures, under homogeneous, supercritical fluid conditions, as well as under vapour-liquid equilibrium (VLE) conditions. The whole project involved several European natural gas companies (E.ON Ruhrgas, Germany; Enagás, Spain; Gasunie, The Netherlands; Gaz de France, France; Snam Rete Gas, Italy; and Statoil, Norway) and was supported by the DVGW (German Technical and Scientific Association on Gas and Water). The GERG-2008 model uses specific equations of state, for 21 components of natural gas mixtures. These are grouped into four main components (methane, nitrogen, carbon dioxide and ethane) and 17 secondary components (e.g. propane, n-butane, isobutane). A new class of equations of state, developed by Klimeck [56] in 2000, is adopted for the calculation of the ideal-gas state and the residual part of the Helmholtz free energy for the main components of natural gases, including methane.

Actually, there are many equations of state that are applied as standards for natural gas in many industrial applications. For example, for several applications involving liquid phase and phase-equilibrium calculations, cubic equations of state, such as the Peng and Robinson [57] equation, are commonly used. Unfortunately, almost all of these equations show poor accuracy in describing the thermodynamic properties of gases, or have a very limited validity range of temperature, pressure and composition (e.g. McCarty [58]).

In addition, most of the applications involving natural gas storage or transport through the use of pipelines, occur mainly in gaseous phase conditions, at temperatures ranging from (250 to 350) K and pressures up to 30 MPa. In this region, the internationally accepted standard for the calculation of natural gas properties is the ISO 20765-1:2005,5 Standard, namely the AGA8-DC92 equation of state of Starling and Savidge [59].

Nevertheless, since 2012 the GERG-2008 has been adopted as ISO Standard (ISO 20765-2/3) for natural gases, particularly for liquid phase applications, as well as processes involving VLE condition. Although this equation of state was developed specifically to evaluate thermodynamic properties of natural gas mixtures, the role of pure methane properties represents the basis which mixtures predictions are calculated on. For this reason, considering the crucial role GERG-2008 plays in the determination of thermodynamic properties of liquefied natural gas, of which methane is the main component, I decided to compare the experimental results

of speed of sound with the values predicted by this model, in addition to those predicted by the equation of state developed by Setzmann and Wagner.

Chapter 4

Speed of Sound and Thermodynamical properties of fluids

From the experimental point of view, speed of sound is a thermodynamic property that can be accurately determined. As a result, it is very advantageous to use speed of sound measurements to determine other thermodynamic properties that are often more complicated to measure directly.

Typically, the thermodynamic properties of a fluid are defined starting from the equation of state of the fluid, which is a function that determines the mutual dependence of temperature, pressure and density in the thermodynamic equilibrium. Therefore, the speed of sound w is a thermodynamic quantity, defined as a function of pressure p and density ρ , as follows

$$w^2 = \left(\frac{\partial p}{\partial \rho} \right)_S, \quad (4.1)$$

where the subscript S indicates that the relationship is valid for adiabatic processes. Thus, equation 4.1 shows that in principle it is possible to determine the function $\rho(T, p)$ by integrating the results of speed of sound measurements.

In general, in order to describe a thermodynamic system, mathematical models (EoS) are used which are defined starting from thermodynamic potentials, such as the Helmholtz free energy (A) or the Gibbs free energy (G). For example, G is defined in terms of differentials, as a function of T and p , as follows

$$dG(T, p) = -SdT + Vdp, \quad (4.2)$$

where S is the entropy and V is the volume occupied by the fluid.

Dividing by the total mass M of the fluid, equation 4.2 can be rewritten in terms

of specific quantities as

$$dg(T, p) = -sdT + \frac{dp}{\rho}, \quad (4.3)$$

where g is the specific Gibbs free energy, while s is the specific entropy. If density measurements ρ are carried out around the thermodynamic point (T_0, p_0) , it is possible to write the relation between g and ρ

$$\left(\frac{\partial g}{\partial p}\right)_T = \frac{1}{\rho}. \quad (4.4)$$

A possible way to write g as a function of temperature and pressure is, for example, the following polynomial

$$g(T, p) = \sum_m \sum_n a_{mn} (T - T_0)^m (p - p_0)^n. \quad (4.5)$$

So, from density measurements in a set of thermodynamic points close to (p_0, T_0) , the coefficients a_{mn} can be calculated by linear regression. In this way it is possible to determine other thermodynamic properties, starting from derivatives of g . For example, from equation 4.3, the specific entropy is defined as

$$s = -\left(\frac{\partial g}{\partial T}\right)_p. \quad (4.6)$$

Nevertheless, the shown method is just a general approach to the problem which, indeed, yields inaccurate results in predicting thermodynamic quantities which are not experimentally measured. As a matter of fact, it has been shown that the coefficients a_{mn} are determined in a more useful way when calculated using measurements of more than one thermodynamic property. In established practice, density, vapour pressure and speed of sound are considered to be the best parameters for the definition of thermodynamic potentials. However, the equation 4.5 described above is only one of the possible formulations in which it is possible to represent the thermodynamic potential. A detailed discussion about the implementation of the fundamental equations of state is reported in Lemmon and Jacobsen [60], as well as in Peleties *et al.* [61]. The following describes some of the thermodynamic relationships and calculation methods used to define thermodynamic properties starting from speed of sound measurements.

Starting from Euler's equations the speed of sound w can be defined for adiabatic transformations (see Equation 4.7), knowing the adiabatic compressibility β_S , as a compression and expansion process caused by the acoustic wave spreading in a fluid

$$\frac{1}{w^2} = \rho\beta_S = \left(\frac{\partial \rho}{\partial p}\right)_S \quad (4.7)$$

Using the 4.7, the density differential can be expressed alternatively as

$$d\rho(S, p) = \left(\frac{\partial\rho}{\partial p}\right)_S dp + \left(\frac{\partial\rho}{\partial s}\right)_p dS = \frac{1}{w^2} dp + \left(\frac{\partial\rho}{\partial s}\right)_p dS. \quad (4.8)$$

In the same way, considering $\rho(T, p)$ as a function of temperature and pressure, $d\rho$ becomes

$$d\rho(T, p) = \left(\frac{\partial\rho}{\partial T}\right)_p dT + \left(\frac{\partial\rho}{\partial p}\right)_T dp. \quad (4.9)$$

So, subtracting the 4.8 and 4.9 and considering that $S=\text{const}$ (then $dS = 0$), we get

$$\frac{1}{w^2} = -\rho\alpha \left(\frac{dT}{dp}\right)_S + \rho\beta_T, \quad (4.10)$$

where $\alpha = -1/\rho(\partial\rho/\partial T)_p$ is the thermal expansion coefficient and $\beta_T = 1/\rho(\partial\rho/\partial p)_T$ is the isothermal compressibility. Instead, considering the differential of entropy dS expressed as a function of temperature T and pressure p , the following is defined

$$\left(\frac{\partial T}{\partial p}\right)_S = -\frac{(\partial S/\partial p)_T}{(\partial S/\partial T)_p} = -\frac{T(\partial S/\partial p)_T}{c_p}, \quad (4.11)$$

where the term $c_p = T(\partial S/\partial T)_p$, namely the isobaric specific heat, has been introduced.

Since Gibbs' energy g is a real function depending on two real variables, then its combined derivatives do not depend on the order in which the derivatives are calculated. So, being g described by equation 4.3, it is possible to define the following set of equations

$$\begin{cases} \frac{\partial}{\partial p} \left(\frac{\partial g}{\partial T}\right) = -\left(\frac{\partial S}{\partial p}\right)_T \\ \frac{\partial}{\partial T} \left(\frac{\partial g}{\partial p}\right) = \frac{\partial}{\partial T} \left(\frac{1}{\rho}\right)_p \end{cases}. \quad (4.12)$$

So, requiring the first equation in 4.12 to be equal to the second, it is possible to define

$$\left(\frac{\partial S}{\partial p}\right)_T = -\frac{\partial}{\partial T} \left(\frac{1}{\rho}\right) = \frac{1}{\rho^2} \left(\frac{\partial\rho}{\partial T}\right)_p = -\frac{\alpha}{\rho}. \quad (4.13)$$

Then, replacing this last equation in equation 4.11 and additionally using equation 4.10, it is possible to define the derivative of the density with respect to the pressure, when the system is subjected to an isothermal transformation:

$$\left(\frac{\partial \rho}{\partial p}\right)_T = \frac{T\alpha^2}{c_p} + \frac{1}{w^2}. \quad (4.14)$$

Analogously to what was done to obtain equation 4.14 for the density derivative with respect to pressure, it is also possible to obtain an equation for the isobaric specific heat capacity c_p , through some thermodynamic relations.

By using equation 4.11 and considering that c_p is defined as

$$c_p = T \left(\frac{\partial S}{\partial T}\right)_p, \quad (4.15)$$

its derivative versus temperature becomes

$$\left(\frac{\partial c_p}{\partial T}\right)_p = \frac{\partial}{\partial T} \left[T \left(\frac{\partial S}{\partial T}\right)_p \right] = \left(\frac{\partial S}{\partial T}\right)_p + T \left(\frac{\partial^2 S}{\partial T^2}\right)_p. \quad (4.16)$$

However, to determine the dependency of specific heat on pressure, some additional observations have to be considered.

Taking into account the relation $(\partial/\partial p)(\partial/\partial T) = (\partial/\partial T)(\partial/\partial p)$ which is valid for a real function, it is possible to define the following equation

$$\frac{\partial}{\partial p} \left(\frac{\partial S}{\partial T}\right) = \frac{\partial}{\partial T} \left(\frac{\partial S}{\partial p}\right) = -\frac{\partial}{\partial T} \left(\frac{\alpha}{\rho}\right) = \frac{1}{T} \left(\frac{\partial c_p}{\partial p}\right)_T, \quad (4.17)$$

where equations 4.13 and 4.15 are used to derive the relationship between the last two terms.

So, from equation 4.17, it is possible to get

$$\left(\frac{\partial c_p}{\partial p}\right)_T = -T \frac{\partial}{\partial T} \left(\frac{\alpha}{\rho}\right) = T \frac{\partial}{\partial T} \left(\frac{1}{\rho^2} \frac{\partial \rho}{\partial T}\right) = T \left[-\frac{2}{\rho^3} \left(\frac{\partial \rho}{\partial T}\right) + \frac{1}{\rho^2} \left(\frac{\partial^2 \rho}{\partial T^2}\right) \right]. \quad (4.18)$$

Then, the following equation for the variation of the isobaric heat capacity with respect to the pressure is obtained

$$\left(\frac{\partial c_p}{\partial p}\right)_T = -\frac{T}{\rho} \left[2 \frac{1}{\rho^2} \left(\frac{\partial \rho}{\partial T}\right)_p - \frac{1}{\rho} \left(\frac{\partial^2 \rho}{\partial T^2}\right)_p \right]. \quad (4.19)$$

Therefore, equation 4.19 can be used to link density ρ to another experimentally measurable thermodynamic property, namely the isobaric specific heat capacity c_p . This relationship becomes useful since, together with equation 4.14, it allows to define a set of equations that can be solved with respect to the unknown variables ρ and c_p , when they are known as a function of the temperature at a reference

pressure p_0 . In fact, functions $\rho(T, p)$ and $c_p(T, p)$ can be calculated by means of numerical integration, within the entire $T - p$ range in which the speed of sound w is known. In practice, it is possible to use speed of sound data as control points to indirectly determine the thermodynamic properties over a wide range of pressure and temperature, by knowing only the two initial conditions, $\rho(T, p_0)$ and $c_p(T, p_0)$. This approach was first used in Davis and Gordon [62] where the thermodynamic properties of mercury at high pressure were determined by integration methods, while the physical principles and the mathematical methods applied to derive the just described equations are described in Trusler [63].

Chapter 5

Speed of Sound Measurement experimental methods

5.1 Steady-state techniques

Nowadays, speed of sound can be measured with great accuracy using experimental techniques that can be divided into two categories: standing-wave measurements and transient, or pulsed, methods. The use of a technique rather than the other depends on the thermodynamic conditions involved and, in particular, on the thermodynamic state of the fluid to be measured.

Steady-state measurement techniques require measuring cells with particular geometrical shapes. If the sound-source is placed inside a simple-shaped resonating cavity filled with the measuring fluid, it is possible to utilize the stationary condition of the acoustic field that is established within it to determine the speed of sound. The establishment of a stationary acoustic field in a chamber is enhanced when the sound reflection that occurs at the interfaces between the propagation medium and the resonator walls is more efficient. This happens when the acoustic impedance of the fluid is significantly different compared to the impedance of the cavity walls as, for example, in the case of a gas inside a metal resonator. For this reason, stationary techniques are mainly suitable for measuring the speed of sound of fluids in the gaseous phase.

Although the speed of sound is formally independent by the amount of substance as well as is immune to absorption effects, for temperatures and pressures close to the saturation curve, pre-condensation processes and thermal relaxation effects can lead to not negligible measurements errors. Another thermodynamic condition that leads to the possibility of systematic measurement errors is near the critical point. In this condition the compressibility of the fluid becomes infinite, since the volume fluctuations do not generate pressure changes. Thus, the fluid's compressibility becomes infinite and the speed of sound goes to zero. To carry out measurements

under these conditions, it is necessary to use instruments that guarantee high performances in terms of both precision and stability of the experiment. Steady-state measurement methods can only be adopted if the resonant cavity has particularly simple shape, actually spherical or cylindrical, because it is necessary to calculate theoretically the eigenvalues needed to normalize the frequency values of normal modes.

5.1.1 Spherical resonators

In the case of spherical resonators, the speed of sound w is obtained by measuring the resonance frequencies and determining the size of the cavity, such as its radius or volume. Considering the simplified case of a perfectly spherical cavity, it is possible to calculate the acoustic resonance frequencies f_{acu} , when the radius a of the sphere is known:

$$f_{\text{acu}} = \frac{w z_{l,n}}{2\pi a}, \quad (5.1)$$

where the terms $z_{l,n}$ ($n = 0, 1, 2, \dots$ and $l = 2, 3, 4, \dots$) are the n -th zeros of the spherical Bessel function of order l . This equation should still be adjusted to take into account the dissipative losses that occur through irreversible heat transfer in the boundary layer.

A very advantageous and accurate method for independent measurement of the cavity size involves the measurement of resonance frequencies of electromagnetic waves that propagate within the resonator. These electromagnetic waves, typically microwaves, have frequencies f_{em} that can be defined, in a similar way as for acoustic waves, as

$$f_{\text{em}} = \frac{c z_{\text{em}}}{2\pi a} \quad (5.2)$$

where c is the speed of light in a vacuum, while the constants z_{em} can be calculated with good accuracy. By combining 5.1 and 5.2, it is thus possible to calculate the speed of the sound independently of the resonator's dimensions.

$$w = c \frac{f_{\text{acu}} + \Delta f_{\text{acu}}}{f_{\text{em}} + \Delta f_{\text{em}}} \times \frac{z_{\text{em}}}{z_{\text{acu}}}, \quad (5.3)$$

where Δf_{acu} is a term which takes into account the dissipative effects on boundary layer, while Δf_{em} indicates a disturbance due to the partial penetration of microwaves into the metal walls of the cavity. Spherical resonators of this type make it possible to achieve such precision as to allow the experimental re-determination

of the Boltzmann k_B constants using accurate measurements of speed of sound. For example, Moldover [64] was the first who used a spherical resonator to determine k_B constant, with an uncertainty of 14 ppm. Among all the applications of spherical resonators, it is useful to mention as an example the work of Gavioso *et al.* [66, 65, 67] that used an quasi-spherical resonator, shown in Figure 5.1 to determine the speed of sound in pure in helium and argon on isotherms near the triple point of water, determining the Boltzmann constant k_b , with an uncertainty of a few parts in 10^{-6} .

5.1.2 Ultrasonic interferometers

Interferometers, on the other hand allow to measure the speed of sound without prior knowledge of the geometric properties of the instrument. The typical frequencies used in this type of apparatus are generally located in the ultrasonic range. An ultrasonic transducer vibrating at its own resonance frequency is used for this purpose. The most commonly used geometric shape is preferably cylindrical, while two types of interferometers can be identified: those with a variable or fixed acoustic path. In variable path interferometers, the frequency of excitation of the acoustic source is kept constant, while the acoustic path, which is the distance between the

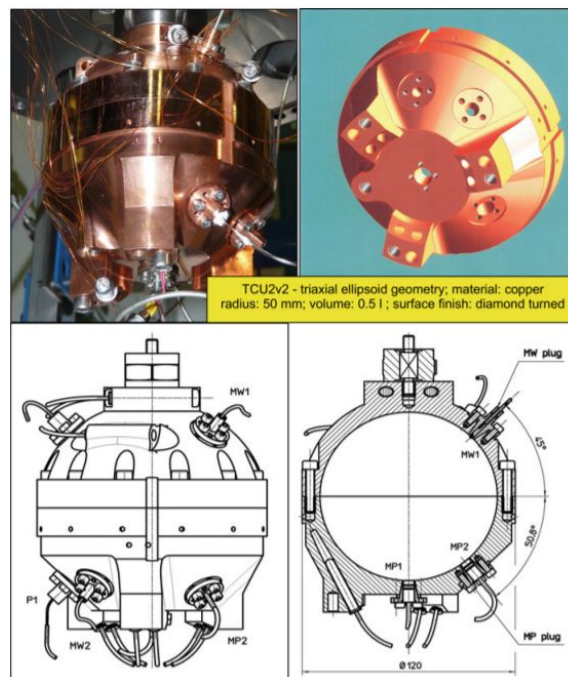


Figure 5.1: Pictures and cross-section of the copper triaxial ellipsoid used by Gavioso *et al.* to determine the Boltzmann constant [65].

transducer and a reflector, is variable. The acoustic source, which also acts as a receiver, emits continuous waves while the reflector is moved until resonances occur. Resonances take place when the length of the cavity L is a multiple of the half-wavelengths $\lambda/2$. Once determined the wavelength λ of the acoustic wave that propagates with a frequency f in the cylindrical cavity, it is possible to calculate the speed w of propagation by means of the relation:

$$w = f\lambda. \tag{5.4}$$

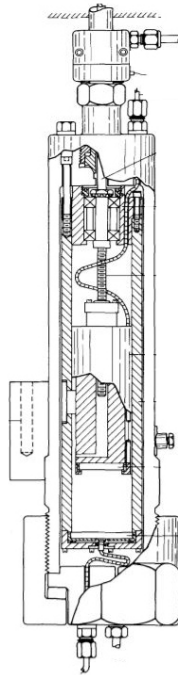


Figure 5.2: Cross-section of the variable acoustic double-transducer interferometer used by Gammon and Douslin in 1976 for absorption and speed of sound measurements [42].

An example of a variable acoustic double-transducer interferometer is the one shown in Figure 5.2 and used by Gammon and Douslin [42], in 1976, to measure the speed of sound in gaseous helium and methane, for temperatures between (110 and 420) K and pressures up to 27 MPa. The accuracy achieved by this instrument is estimated to be around 10 parts per million.

5.2 Transient techniques. Single pulse method or multiple pulse

The problem of measuring the speed of sound in fluids essentially relates to the difference in acoustic impedance between its gaseous and liquid phases. As

previously discussed, acoustic resonators are very well suited to speed of sound measurements in gases, since the ratio between the acoustic impedances of the fluid and that of the resonance cavity walls is generally in the order of 10^{-2} . Uncoupled impedances of acoustic waves on the interfaces between fluid and walls, allow the creation of steady state conditions. The reflection coefficient R on the fluid-solid interface can be calculated by

$$R = \left(\frac{z_s - z_f}{z_s + z_f} \right)^2, \quad (5.5)$$

where z_s and z_f are the acoustic impedance of the solid walls of the cavity and the acoustic impedance of the fluid, respectively. In gases R is in the order of 1, while in liquids this ratio is up to approximately 0.8. For liquids or dense gases, pulsed experimental techniques, or transient techniques, are particularly suitable for investigating fluids. These techniques is implemented with apparatuses operating at ultrasonic frequencies (generally between 500 kHz and 20 GHz) and are based on the direct measurement of the transit time of an acoustic pulse which travels a known distance within the fluid. The speed of sound is determined when the path length L between the acoustic source and the receiver, and the time τ the acoustic pulse needs to cover the distance L , are measured:

$$w = \frac{L}{\tau} = c(L, \tau, p, T). \quad (5.6)$$

In this model L and τ are independent mechanical measurements, while pressure p and temperature T are state variables.

The first and simplest apparatus based on pulsed techniques is the *ultrasonic delay line*. Two parallel plane transducers, held at a known distance by a rigid structure, are immersed in the fluid. One transducer acts as a sound-pulse source while the other is used as a receiver. Unfortunately, instruments of this type are affected by sources of uncertainty that make it complex to determine an accurate time delay between the emission of the acoustic wave and its reception. For example, the use of two acoustic transducers brings an uncertainty to the experiment due to the delay for electronic circuits to convert electrical signals into sound waves and vice versa. To eliminate these additional delays, a reflector can be used to replace the second transducer, thus using a single transducer as both an emitter and a receiver.

In 1976, Papadakis [68, 69] developed a new experimental technique, called *pulse-echo-overlap* which allowed to achieve precisions close to 0.01 % and accuracies of about 0.1 %. With this method, a series of acoustic bursts are emitted by an acoustic transducer, reflected by a reflector and received again by the transducer. The resulting echoes are then visualized by an oscilloscope. The frequency by which

sound pulses are emitted is modified until there is a complete overlap between the echoes, meaning that the trigger interval corresponds to the time difference between two consecutive echoes. Even though this method allows accurate measurement of the time of flight, it still has some limitations. For example, the perfect overlap is determined by direct observation carried out by the operator, thus reducing the possibility for the entire procedure to be automated. Moreover, small wave phase shifts can occur, leading to systematic errors in the determination of the transit time. These problems have been solved by introducing *pulse-echo* methods, after the advent of digital oscilloscopes, when it was possible to significantly improve the accuracy of time of flight measurements, which are typical of pulsed techniques.

5.2.1 Single and multiple pulse-echo technique

Nowadays, *pulse-echo* techniques are the most widely used for speed of sound measurements in fluids in liquid phase. Figure 5.3 shows the general configuration of the sensors used in this technique.

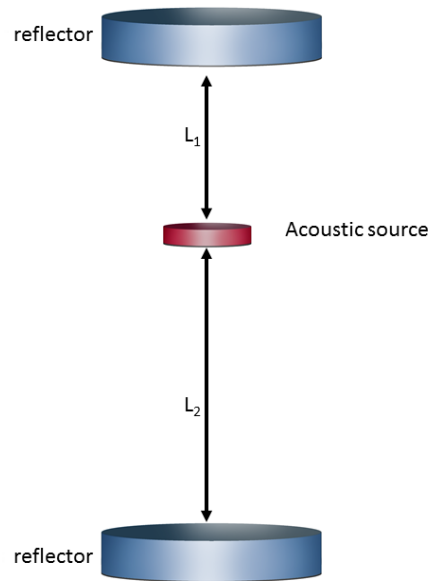


Figure 5.3: General configuration of a *pulse-echo* sensor with double reflectors.

An acoustic transducer vibrates at its resonant frequency while it is immersed within the fluid. An acoustic tone burst is then generated by the vibrational motions of the transducer, propagating in the same direction and in opposite verses,

traveling the paths L_1 and L_2 . A technique that can be applied using this configuration is the *phase-comparison* method. Two acoustic bursts are subsequently emitted from the source. The time τ separating the two pulses is chosen so that the arrive on the transducer of the first echo, namely the one of the pulse which travels the longest acoustic path, coincides with the echo of the second pulse, which travels the shortest distance. Figure 5.4 shows a general scheme describing the operating principle of this technique.

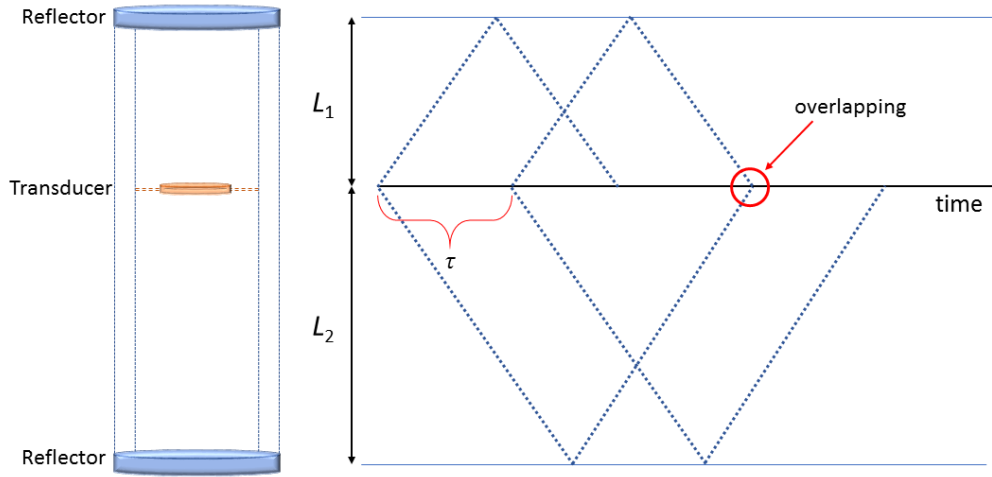


Figure 5.4: Diagram of the *phase-comparison* technique, where two acoustic bursts are emitted after a time delay τ .

The advantage of the *phase-comparison* methods is that it is possible to determine the time delay of τ , with an accuracy of about 100 ppm, by identifying the frequencies f_n where destructive interference occurs and the two echoes cancel each other out. In fact, destructive interference occurs when the phase difference $\Delta\phi$ between the two echoes is equal to

$$\Delta\phi = (2n + 1)\pi, \quad (5.7)$$

so that, being $2\pi f_n = \omega_n$, the following equation holds

$$\left(n + \frac{1}{2}\right) = f_n \tau, \quad (5.8)$$

where ω_n is the angular frequency, while f_n is the frequency where destructive interference occurs. By identifying two successive cancellation frequencies is then possible to get the order n , such as

$$n = \frac{f_n}{\Delta f_n} - \frac{1}{2}, \quad (5.9)$$

where $\Delta f_n = f_{n+1} - f_n$. Finally, by replacing in equation 5.8 the value of n so obtained, it is possible to determine the time τ .

Using modern sophisticated digital oscilloscopes it is possible to determine the time delay simply by analysing the sampled signals by means of a correlation function.

Chapter 6

The *double pulse-echo* technique

The experimental measurement technique adopted in this work to obtain speed of sound measurements is based on the double *pulse-echo* technique. This is a well-established method, widely used for speed of sound measurements in fluids [70, 71, 72].

The measuring cell used, as in the case of the *phase-comparison* technique, is a device that can be described in a simplified way as an ultrasonic acoustic source placed at different distances from two parallel plane reflectors. During measurements, the cell is completely immersed in the fluid under study. This technique makes use of a piezoelectric ultrasonic transducer, working both as an emitter and as receiver. A function generator excites the piezoceramic transducer with a sinusoidal tone-burst. Typically, the carrier frequency of the transmitted signal is set to be equal to the transducer's resonance frequency. Nevertheless, the use of acoustic sources with limited bandwidth leads to signals with a ring-down in the order of 30 cycles or more when the source is excited with 5 cycles. For this reason, it is advantageous to choose acoustic transducers, such as wide-band piezoelectrics, which allow the frequency of the signal to be adjusted in order to produce non-distorted echoes. Commonly, ideal ultrasonic pulses are generated by a function generator that excites the acoustic transducer with variable voltages over time t . Specifically, bursts are extracted from a continuous signal of the type:

$$v(t, \omega_0, \tau) = s(t, \tau)e^{i\omega_0 t}, \quad (6.1)$$

where τ , which is an integer multiple of $\tau = 2\pi/\omega_0$, corresponds to the duration of the acoustic burst and ω_0 is the carrier frequency. Besides, the signal amplitude $s(t, \tau)$ depends on the time as follows:

$$s(t, \tau) = \begin{cases} 0, & \text{if } t < -\frac{\tau}{2} \\ 1, & \text{if } -\frac{\tau}{2} < t < \frac{\tau}{2} \\ 0, & \text{if } t > \frac{\tau}{2} \end{cases} \quad (6.2)$$

After being vibrated, the acoustic transducer yields an acoustic wave that spread simultaneously in opposite directions following two acoustic paths L_1 and L_2 of different lengths. Each acoustic wave burst is reflected back to the transducer. The electrical signal sent by the function generator to the transducer as well as the echoes from the reflectors are sampled by a digital oscilloscope.

Figure 6.1 shows a scheme of the functioning for the double *pulse-echo* technique used. As the acoustic paths, L_1 and L_2 , have different lengths, the pulses reach the fluid-reflector interface after the times τ_1 and τ_2 , respectively, with $\tau_1 \neq \tau_2$.

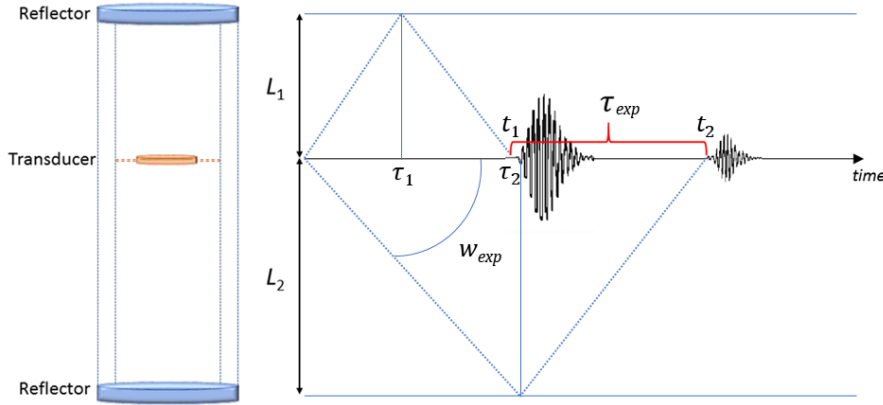


Figure 6.1: General scheme of a double *pulse-echo* technique adopted in this work.

The first echo, which comes from the nearest reflector, travels the distance $2L_1$ taking a time t_1 , while the second echo from the farthest reflector travels the acoustic path $2L_2$ in the time t_2 . Since the measurements occur under thermodynamic equilibrium conditions within a propagation medium that is supposed to be isotropic, the two acoustic pulses travel at the same speed, w , so it is possible to write the following equations:

$$w = \frac{2L_1}{t_1} = \frac{2L_2}{t_2}. \quad (6.3)$$

The quantity to be measured experimentally is the time delay, τ_{exp} , or time of flight, between the first and second echoes. This can be calculated, starting from equation 6.3, in the following simple way:

$$\tau_{\text{exp}} = t_1 - t_2 = \frac{2(L_1 - L_2)}{w}. \quad (6.4)$$

Thus, the experimental speed of sound w_{exp} can be calculated as the ratio between the travelled length $2\Delta L = 2(L_2 - L_1)$ and the time of flight τ_{exp} , between the two echoes.

$$w_{\text{exp}} = \frac{2\Delta L}{\tau_{\text{exp}}}, \quad (6.5)$$

where τ_{exp} is the time delay after which two successive echoes reach the transducer after being reflected.

6.1 Time of flight measurement

Experimental measurement of the time of flight is carried out thanks to the possibility of using a digital oscilloscope to sample the acoustic pulses, when received by the ultrasonic transducer, in the form of digital signals. An example of the shape of the echoes is shown in figure 6.2, where the acoustic pulses, namely the two echoes received by the transducer, are represented on the time axis as two wave packets.

The digital signal $P_1(t_i)$, corresponding to the first echo, is correlated to the second echo $P_2(t_j)$, coming from the farthest reflector, where $t_j = t_i + \tau$, by the temporal correlation function $C(\tau)$.

$$C(\tau) = \int_{-\infty}^{+\infty} P_1(t)P_2(t + \tau)dt, \quad (6.6)$$

where each $\tau \in [-\infty, \infty]$ represents the time shift between the two echoes $P_1(t_i)$



Figure 6.2: The oscilloscope screen used for sampling the echoes.

and $P_2(t_j)$. Then, evaluating the value τ_{exp} that maximizes the function $C(\tau)$, it is possible to determine the time-delay between two consecutive echoes (see Figure 6.3). An easy and useful mathematical method to calculate this value is based on the *Fast Fourier Transform* (FFT) algorithm. Indeed, starting from the properties of Fourier transforms it is possible to state that

$$\mathcal{F}(C) = \mathcal{F}(P_1) * \mathcal{F}(P_2), \quad (6.7)$$

and, then

$$C(\tau) = \mathcal{F}^{-1}[\mathcal{F}(P_1) * \mathcal{F}(P_2)], \quad (6.8)$$

where operator \mathcal{F} represents the Fourier transform of the signal, numerically implemented by the fast Fourier transform, FFT. Operator \mathcal{F}^{-1} is its inverse. So, this expression leads to the possibility of obtaining in a simple way the correlation function $C(\tau)$ as the inverse transform of $\mathcal{F}(C)$.

The accuracy of this experimental measurement still suffers from some side effects which need to be taken into account in order to make the results sufficiently precise. As a matter of fact, a correction has to be introduced to both the experimental time of flight and the difference between the lengths of the ultrasonic cell. In particular the experimental time difference, τ , needs two types of corrections, namely

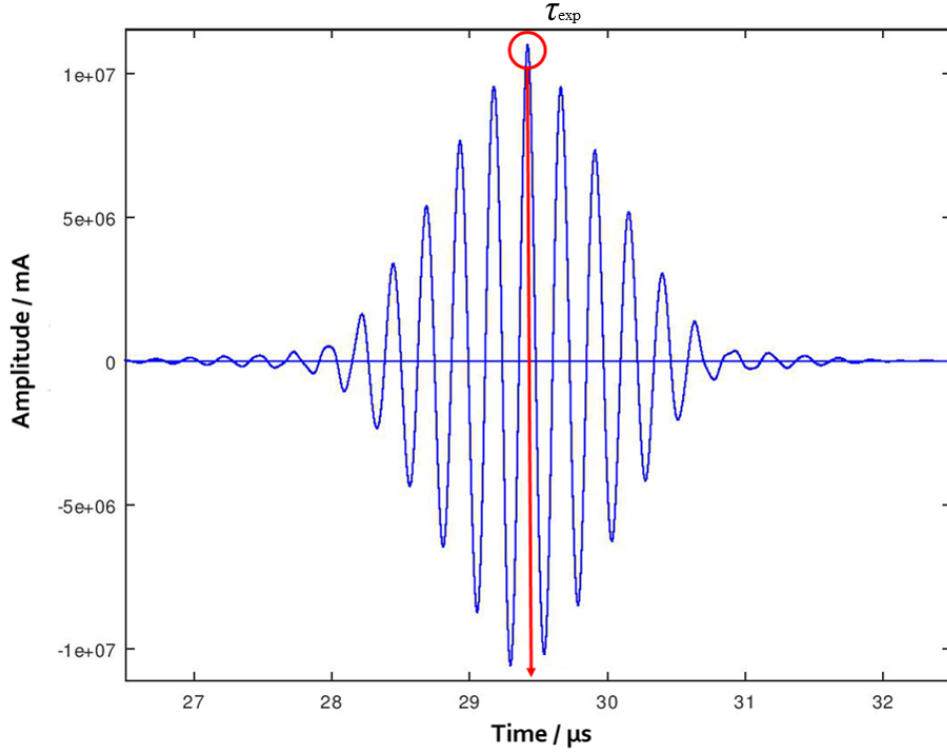


Figure 6.3: Correlation function between two consecutive echoes, P_1 and P_2 .

by the effect of small thermal gradients that occur inside the cell and diffraction effects, caused by the finite dimensions of the acoustic source, in order to match the ideal condition of perfect plane waves travelling in free-space. The following time of flight correction formula is used, to obtain the time-delay τ_g , which occurs in the presence of thermal gradients:

$$\tau_g = \tau_{\text{exp}} \left(1 + \frac{a}{\tau_{\text{exp}} w_{\text{exp}}^2} (L_2^2 - L_1^2) \right). \quad (6.9)$$

This correction is valid under the assumption of $a \ll w_{\text{exp}}$, where a is a term that represents the variation of w with respect to the length z along which the thermal gradient is measured and that can be expressed as:

$$a = \frac{\partial w}{\partial z} = \frac{\partial w}{\partial T} \frac{\partial T}{\partial z}. \quad (6.10)$$

For the specific temperatures involved in this experiment, the term $\partial w / \partial T$ is evaluated, from experimental measurements, to be about $-10.8 \text{ m s}^{-1} \text{ K}^{-1}$, while term $\partial T / \partial z$ is recorded during measurements. For comparison, a gradient of 300 mK

would generate correction in the order of 0.1 % on the time of flight. However, typical gradients during the experiment were kept below 80 mK.

On the other side, the diffraction corrections can be calculated using the following expression:

$$\delta t = \frac{\phi(2L_2) - \phi(2L_1)}{\omega_0}, \quad (6.11)$$

where ω_0 is the pulsation of the carrier wave and $\phi(L)$ is the phase shift related to a plane wave travelling the same distance of the actual wave fronts produced by the transducer.

Once the experimental speed of sound, w_{exp} , is preliminary evaluated, the phase shift, $\phi(L)$, can be calculated as a function of both the dimensions of the cell (L_1 and L_2) and the radius b of the acoustic transducer with the following equation

$$\phi(L) = \text{Arg} \left(1 - \frac{4}{\pi} \int_0^{\pi/2} \exp \left[-i \left(\frac{2\omega_0 b^2}{w_{\text{exp}} L} \right) \cos^2(\theta) \right] \sin^2(\theta) d\theta \right) \quad (6.12)$$

The integral can be solved analytically and the following closed form can be used to determine the phase shift which occurs when an acoustic wave travels the distance L :

$$\phi(L) = \text{Arg} \left[1 - \exp \left(-\frac{iA}{2L} \right) \left(J_0 \left(\frac{A}{2L} \right) + iJ_1 \left(\frac{A}{2L} \right) \right) \right], \quad (6.13)$$

where $A = 2\omega b^2/w_{\text{exp}}$, while J_0 and J_1 are Bessel functions of zero and first order, respectively.

So, finally, the corrected time-delay of our interest becomes

$$\tilde{\tau} = \tau_g + \delta\tau.$$

6.2 Acoustic path determination

The accurate and indirect measurement of the distances from the acoustic source to the reflectors is essential to determine the acoustic path ΔL appearing in equation 6.5. A direct measurement of the acoustic path can therefore be obtained with the use of a coordinate-measuring machine. This type of measuring instrument allows to obtain measurements, with an uncertainty in the order of 0.1 μm . However, for many applications it is more convenient to use indirect measurements, where a reference fluid can be used to determine ΔL with an acceptable accuracy (usually

the relative uncertainty associated to this type of calibration technique ranges from (0.01 to 0.03) %. In this work it has been used pure water to indirectly calibrate the measurement cell. In fact, since thermodynamic properties of water are well known over a wide range of pressures and temperatures, in particular at ambient temperature, T_0 , and atmospheric pressure, p_0 , where the uncertainty in speed of sound is claimed to be ± 0.005 % [73], then it is possible to obtain $\Delta L(T_0, p_0)$, namely the difference $L_2 - L_1$, as

$$\Delta L(T_0, p_0) = w_w(T_0, p_0)\tau_w/2, \quad (6.14)$$

where, w_w is the speed of sound of water and τ_w is the time-delay measured during the calibration.

When measurements are performed at a temperature and pressure different from those of the calibration, ΔL has to be corrected according to

$$\Delta L(T, p) = \Delta L(T_0, p_0) \left(1 + \alpha(T - T_0) - \frac{\beta_T}{3}(p - p_0) \right), \quad (6.15)$$

where β_T is the isothermal compressibility of the AISI-316L stainless steel and α is the thermal expansion coefficient. Below 230 K, this functional form cannot be used since $\alpha(T)$ cannot be considered as constant. Using the values available in the literature [74], $\alpha(T)$ can be calculated by a polynomial fitting function as:

$$\alpha(T) = a + bT + cT^2 + dT^3, \quad (6.16)$$

with $a = 5.867532 \cdot 10^{-7}$, $b = 1.405386 \cdot 10^{-7}$, $c = 5.263604 \cdot 10^{-10}$, $d = 7.604209 \cdot 10^{-7}$. In this way ΔL becomes:

$$\Delta L(T, p) = \Delta L(T_0, p_0) \left(1 + \alpha(T) \exp(\gamma) - \frac{\beta}{3}(p - p_0) \right), \quad (6.17)$$

with $\gamma = (a(T - T_0) + \frac{b}{2}(T^2 - T_0^2) + \frac{c}{3}(T^3 - T_0^3) + \frac{d}{4}(T^4 - T_0^4))$.

Finally, the corrected speed of sound \tilde{w} of methane can be calculated as the ratio

$$\tilde{w} = \frac{2\Delta L(T, p)}{\tilde{\tau}}, \quad (6.18)$$

where $2\Delta L(T, p)$ is the acoustic path corrected for thermal expansion and isothermal compression effects, while $\tilde{\tau}$ is the time of flight adjusted in order to take in account diffraction effects.

Chapter 7

State of the art of Speed of Sound Measurements of Liquid Methane

Methane is a natural gas that has always aroused great interest because of its beneficial properties and the role it can play in a variety of socio-economic areas. It was Alessandro Volta [75] who, in 1778 at Lake Maggiore, discovered what he called marsh gases, since it was isolated for the first time from the gases produced at the bottom of the swamps, as a result of the fermentation of cellulose present in plant debris. However, already in the 4th century B.C., Chinese were drilling the soil in search of natural gas which they used to boil large vats containing a solution of water and salt to obtain salt.

Chinese were also famous for transporting natural gas through bamboo pipes [76], as shown in picture 7.1.



Figure 7.1: Replication of the transport system through bamboo pipelines used to transport natural gas [77].

Despite these first significant innovations, it was not until the 19th century that the commercial exploitation of natural gas began. In 1821, William Hart, known as the “father of natural gas”, commissioned a small natural gas well near Lake

Erie in the northeastern United States. For most of the 19th century, natural gas was used primarily as a fuel for lamps. It would soon shift from being a source of light to its modern role as a source of energy. From the 1890s, since cities began to use electricity for public street lighting, gas producers considered new uses for their product. The invention of the Bunsen burner in 1885 eventually allowed the controlled combustion of natural gas, mixing gas and air in the right proportions, thus giving space to new opportunities for the use of natural gas as a source of heat in different applications, in cooking as well as in heating. It follows that, because of the important role it has played in history, methane is now one of the most studied natural gases.

For this reason, research and measurements of its thermodynamic properties are available since the early 1900s.

7.1 First investigations of liquid methane

Currently, there are a lot of experimental works in literature concerning speed of sound measurements of methane. Unfortunately, only a few of these studies investigated the liquid phase, because of the great complexity required to realize experimental devices capable of operating, with an acceptable level of accuracy, at cryogenic temperature. In fact, while the first speed of sound measurements for gaseous methane date back to the beginning of the last century, it was only around the middle of the twentieth century that the technological and engineering developments allowed to face such a challenge. First attempts to measure speed of sound of methane in gas phase was carried out by Dixton *et al.*, in 1921 [78], while the first investigations into liquid methane under its saturation pressure were published in the late 1940s.

In 1949, A. Van Itterbeek and L. Verhaegen [79] measured the speed of sound by acoustic interferometry methods for pressures below the saturation pressure and for temperatures between (90 and 112) K. In their experiment the gas was condensed and solidified inside a resonator tube, which was cooled with liquid air. Although this work was the first successful attempt in measuring the speed of sound of methane in liquid phase, its experimental results are not reliable, since the declared uncertainty is estimated to be up to 1 %. Despite these results have not been taken into account for the validation of the experimental measurements given in this work, as they do not meet today's quality requirements, they are mentioned in the list of works of great relevance in the context of liquid methane speed of sound determination.

7.2 Accurate measurements at cryogenic temperatures

From the second half of the last century, technological developments, the introduction of more accurate instruments as well as the advance of working equations used for interpreting the measurements, allowed experiments to be carried out with increasingly accuracy. This resulted in the establishment of experimental techniques that today represent the consolidated methods for the measurement of speed of sound in fluids, both in gas and liquid conditions.

As for the speed of the sound of liquid methane, an important experiment was that of Van Dael *et al.* [80], in 1965. This was the first experimental work in which an ultrasonic *pulse-echo* technique was used for speed of sound measurements at cryogenic temperature. In fact, with *pulse superposition* methods they were able to measure this thermodynamic property along the saturated liquid line, for temperatures between triple point and critical point (94 and 190) K and, through the saturation curve, up to 4.6 MPa with a declared uncertainty of 0.1 %. A scheme of the control instruments of the apparatus is described in detail in [81] and shown in picture 7.2. In this configuration, two bariumtitanate discs are separated by an

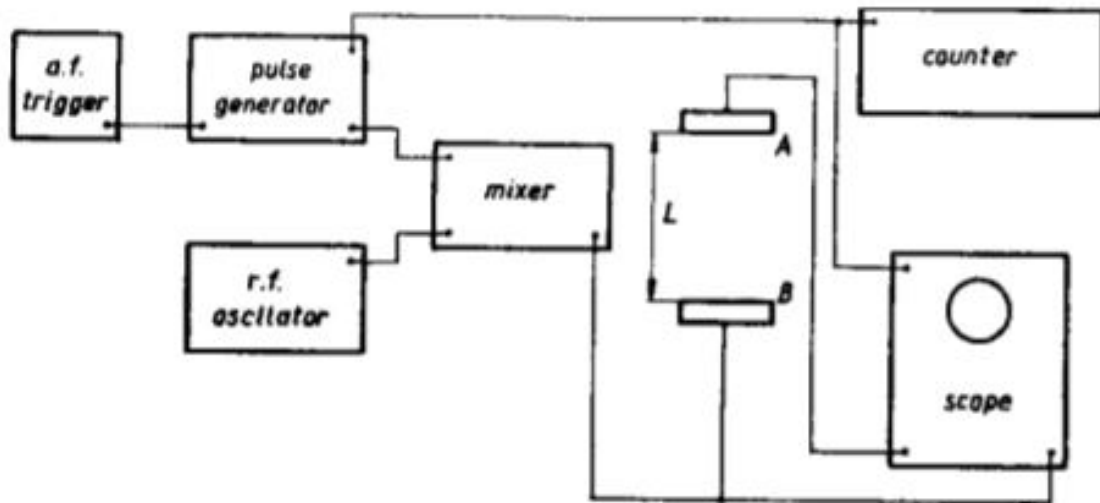


Figure 7.2: Block-scheme of the apparatus used by Van Dael [81].

invar steel tube which is completely filled with the liquid under study. An electrical pulse of 2 MHz frequency is applied to the first disk A, which acts as a acoustic source. An acoustic burst passes through the liquid and reaches the second disk B, which works as a reflector, after a time t .

Thus, the echoes produced by these reflections arrive at A after $2t$. At the same time as this happens, a new electrical pulse is applied to A. In this way, the two

signals are summed together when the time $2t$ is a multiple of the period of the carrier wave, intensifying each other by interference. The repetition frequency of the electrical pulses is regulated so that all the echoes, generated by successive pulses arriving in a period of $2t$ coincide. The pulse repetition frequency is adjusted so that all the echoes that are generated each time by the pulses applied to the first disc, return to A after the same period $2t$. In this way the speed of sound is directly derived from:

$$w = \frac{L}{t} = 2Lf_r$$

where L is the distance between the two discs A and B and f_r is the frequency at which the carrier signal is repeated. Table 2 in Appendix 10.7 shows the speed of sound results published in this paper. Experimental pressures have been recorded for temperatures above 140 K, while for lower temperatures, the pressure values were derived from Keyes *et al.* [82].

Using the same apparatus, Van Itterbeek *et al.* [44] achieved further measurements of sound velocity. This time, however, the data obtained do not refer exclusively to the pressures of saturated liquid, but have been obtained along six isotherms between (91 and 191) K and for pressure up to 18 MPa (see table 3 in Appendix 10.7). Also in this case the declared uncertainty was 0.1 %. In the same year, Blagoi *et al.* [83] carried out speed of sound measurements of liquid methane along the saturation curve, by using an acoustic interferometer in a temperature range from (91 to 178) K and pressures up to 3.2 MPa, with an uncertainties from (0.3 to 1) %. Due to the poor declared accuracy, these measurements were not taken into account in the drafting of the equation of state of methane [23]. Nevertheless, this work is mentioned in this document and its results are listed in table 4 in Appendix 10.7, in order to give a comprehensive overview on all experimental measurements involving liquid methane.

In 1969 another investigation concerning the ultrasonic attenuation in liquid methane was made by Singer [84] using a *variable-path-length* acoustic interferometer. The apparatus used in these measures is described in detail in [85] and shown in figure 7.3. The technique used for adsorption measurements was based on the *single-crystal pulsed-system*, with a variable path. The experimental data of speed of sound (see table 5 in Appendix 10.7) are related to temperatures from (94 to 145) K and pressures from (0.2 to 9) MPa with an overall uncertainty of 0.5 %.

During the mid-1970s two different works were published by Straty. In his first experiment [43] speed of sound measurements were made for saturated liquid methane from its triple point temperature up to 186 K and for compressed fluid from (100 to 300) K and for pressures up to 35 MPa. The estimated uncertainty of

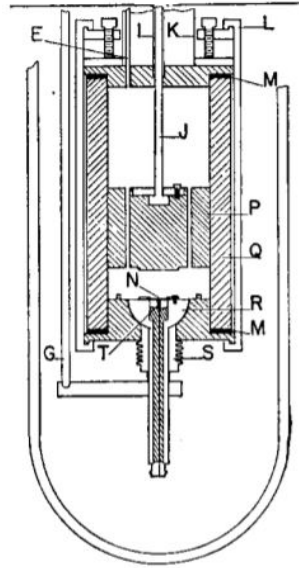


Figure 7.3: Schematics of the apparatus used by Singer and Naugle [85] for ultrasonic attenuation in liquids.

the experimental results is of about 0.05 %. The experimental method was based on the *pulse superposition* technique. The apparatus was the same used by Younglove [86], to measure the speed of sound of Hydrogen. An X-cut quartz crystal, used as emitter, was excited at its resonant frequency of 10 MHz. A sound pulse was emitted and received by a second identical crystal. The two crystals were separated by a fused quartz tube, at a distance that determined the acoustic path of the acoustic signal (see figure 7.4). A stable and adjustable oscillator was operated to control the pulse-repetition rate of the carrier pulse, until the time between two consecutive pulses was equal to the time taken for an acoustic pulse to return to the crystal from which it was generated. The entire apparatus was cooled down through the conduction of gas in a stainless steel tube connected to the sample holder. The final results for the compressed fluid were obtained along nine isotherms and are shown in the table 6 in Appendix 10.7. One year later, Straty performed a further investigation on sound velocity in liquid methane [49], this time using a *Brillouin scattering* technique. Although the accuracy of his results was worse than that achieved in the previous experiment, about 0.5 %, it is useful to mention this work because it was the first time this type of technique was used to measure the speed of sound of methane at cryogenic temperatures.

Another work was the one published by Gammon and Douslin in 1975 [42]. They performed measurements close to the phase boundary reaching a total uncertainty of about 0.01 %, which nowadays is the best accuracy ever obtained for this type of measurement. For this reason the highest number of speed of sound data points

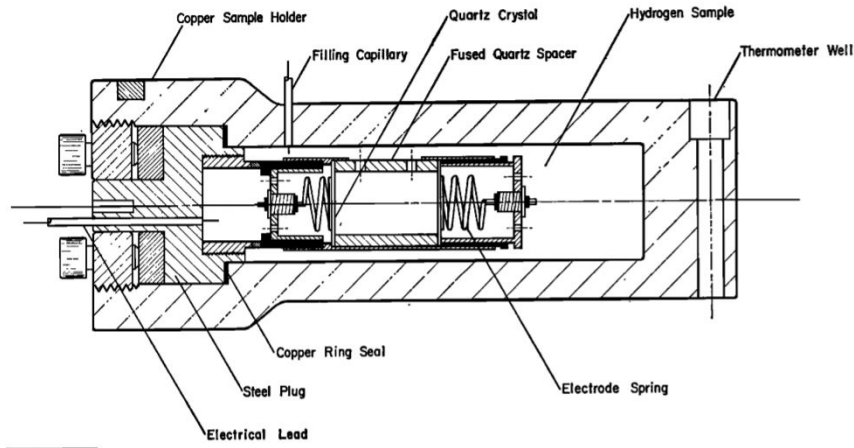


Figure 7.4: Scheme of the sample holder used within the apparatus as described in Younglove [86].

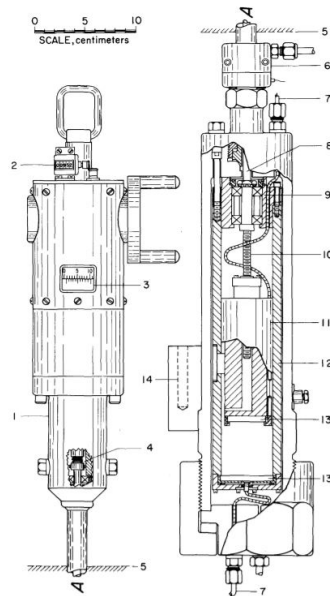


Figure 7.5: Diagram of the interferometer used by Gammon and Douslin [42]. ¹ packing gland; ² mechanical counter; ³ vernier; ⁴ bellows coupling; ⁵ bath insulation; ⁶ tempering block; ⁷ crystal lead; ⁸ drive shaft; ⁹ bearing assembly; ¹⁰ micrometer screw; ¹¹ piston; ¹² cylinder; ¹³ X-cut quartz crystal; ¹⁴ thermometer well

(see Table 7 and 8 in Appendix 10.7) selected for the formulation of the equation of state of methane [23], belongs specifically to this work. The experimental apparatus, shown in figure 7.5, consisted of a double-crystal cylindrical type interferometer, filled with the measurement sample. At its ends there were two X-cut quartz crystals, with a resonance frequency of 0.5 MHz. The one at the lower end

serves as a transmitter, while the upper end is used as a receiver for sound propagated through the fluid. The distance between the two crystals could be varied while keeping the volume of the fluid constant. The instrument could be used in two operating modes. When signal shows small attenuation, as a resonance tube with a length equal to a multiple of half the wavelength of the acoustic wave. When the attenuation was greater, it was used as a continuous wave system, where the phase shifts were determined by a dual-track oscilloscope.

The last essential work that has to be mentioned in this short review is the research carried out by Baidakov in 1982 [45]. In his paper results for ultrasonic speed of liquid methane are published in the temperature interval from (150 to 183) K and within a pressure range from atmospheric pressure up to 4 MPa (see Table 9 in Appendix 10.7). The innovation of this work is that values for metastable methane have been obtained for the first time during these measurements. Measurements in metastable liquid were made up to 0.94 MPa below the saturation curve. In order to reach this result Baidakov used a pulse technique, which is the most suitable method to carry out measurements in metastable phases of fluids, since it allows the system to be perturbed as little as possible. The declared uncertainty of speed of sound, ignoring any side error which may occur across the saturation line, was from (0.1 to 0.3) %.

Table 7.1 reports the most important measurements concerning the speed of sound in liquid methane. Their importance is highlighted by the fact that the data shown obtained are, for the most part, the values used to realize the equation of state of methane [23]. Table 7.1 summarises the experimental techniques used in the respective works, the involved temperature and pressure ranges, as well as the uncertainties declared by authors. Finally, in Figure 7.6 are shown all the points (p, T) where measurements of speed of sound were obtained, classified according to their authors.

Authors	Technique	T / K	p / MPa	Declared uncertainty / %
Van Itterbeek <i>et al.</i> (1949)	Acoustic interferometer	90 - 112	<0.1	(2 - 5)
Van Deal <i>et al.</i> (1965)	Pulse superposition technique	94 - 190	<4.6	0.1
Balgori (1967)	Acoustic interferometer	91 - 178	<3.2	(0.3 - 1)
Van Itterbeek, Thoen (1967)	Pulse superposition technique	111- 190	0.1-18	0.1
Singer (1969)	double pulse-echo	94 - 145	0.2 - 9	0.5
Straty (1974)	Pulsed technique	91 - 300	1.6 - 35	(0.05 - 0.2)
Straty (1975)	Brillouin scattering technique	112 - 300	<17.6	0.5
Gammon <i>et al.</i> (1975)	Acoustic interferometer	113 - 323	0.1 - 24	(0.01 - 1)
Baidakov (1982)	Pulsed technique	150 - 183	<4	(0.1 - 0.3)

Table 7.1: List of speed of sound experimental data of methane at cryogenic temperature.

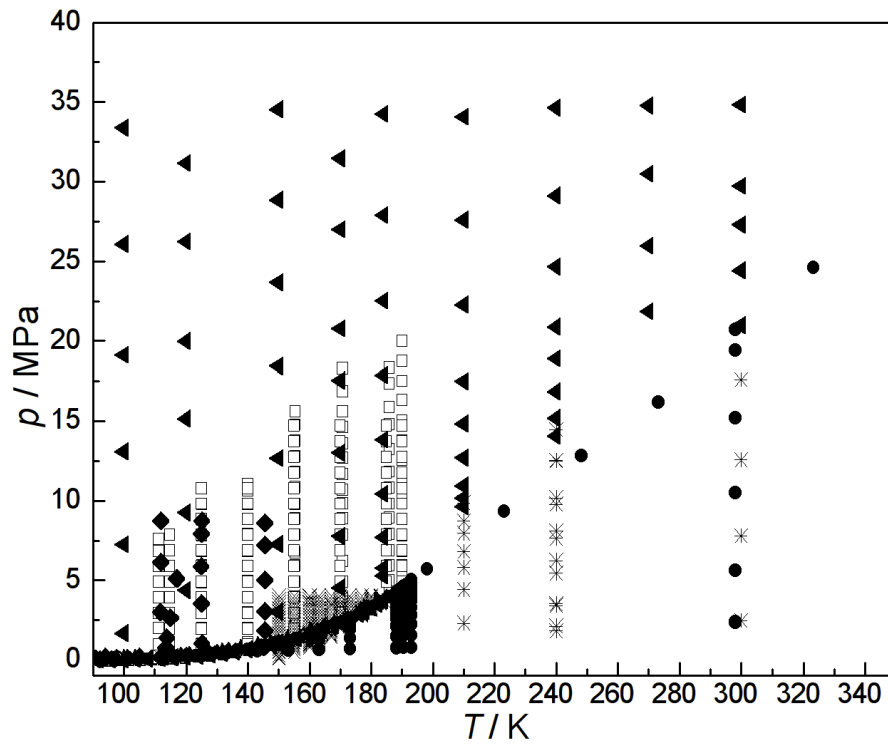


Figure 7.6: $T - p$ Diagram of speed of sound experimental data of liquid methane available on literature.

Chapter 8

Experimental Apparatus

In the present work, the speed of sound of pure liquid methane (99.9995 %, weight provided by SIAD, ITALY, see Table 8.1) has been obtained for temperatures between (130 and 162) K and for pressures up to 10 MPa. The apparatus is based on the *double pulse-echo* technique, already described in Chapter 6.

Measuring the time, τ , that the emitted wave needs to travel from the acoustic source to two reflector walls and back to the transducer and knowing the difference between the two acoustic paths, ΔL , it is possible to determine the speed of sound in the sample with a considerable accuracy and resolution.

Chemical name	Source	Initial Mole Fraction Purity	Purification Method	Final Mole Fraction Purity	Analysis Method
Methane (CAS name: 74-82-8)	SIAD (ITALY)	0.999995	none	-	-

Table 8.1: Sample table.

8.1 The ultrasonic cell

The core of the experimental apparatus is the ultrasonic cell, realized in stainless steel AISI 316L, with two spacers of different lengths. Figure 8.1 shows a longitudinal section of the measurement cell used in this work.

The piezoelectric transducer (DuraAct^U patch, P-876K025, Piezo Technology, see Figure 8.2) has an active diameter section of 7 mm and is used both as source and receiver. Two 6 mm thick stainless steel reflectors (number 1 in the picture) are screwed to the ends of the cell. In order to minimize the effect of the back-reflections into the cell, the outer planes of reflectors were built with a series of pyramid-shaped cutting. Furthermore, the piezoelectric transducer is clamped between two cone-shaped supports (number 3 in the picture) that are used to reflect,

away from the receiver, the components of the signal that are out of the cylinder axis. Finally, on the lateral surface of the measuring cell there are eight eyelets (number 2 in the picture) which allow the cell to be completely filled and immersed within the measuring fluid. The measuring cell is placed in a stainless steel pressure vessel (see Figure 8.4 and Figure 10 in Appendix 10.7) capable of operating at up to 70 MPa. The inserting of the cell inside the pressure vessel, as well as its stability during the assembly of the entire apparatus and during the measurement operations, are provided by two steel coupling holders fixed to one of the vessel stopper, as shown in Figure 8.3, where the connection set-up is shown.

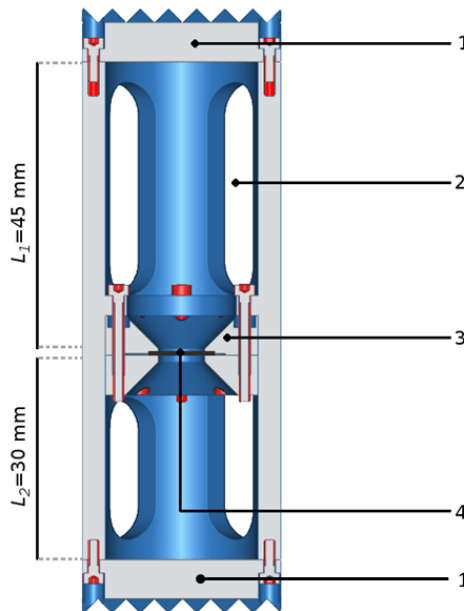


Figure 8.1: Front section of the ultrasonic cell. (1) Stainless steel reflector; (2) Cell eyelet; (3) Cone-shaped support; (4) Ultrasonic transducer.



Figure 8.2: Ultrasonic piezoelectric transducer.



Figure 8.3: Ultrasonic cell and vessel stopper with coupling holders.

8.2 Thermostating system

The thermal unit consists of a copper shield that is used to control the heat flux between an heat exchanger, where liquid nitrogen circulates, and a pressure vessel containing the liquid methane. Figure 8.5 reports a scheme of the thermostating



Figure 8.4: Stainless steel pressure vessel used to carry out speed of sound measurements at high pressure.

system.

In order to thermally insulate the apparatus from the outside environment, the entire system is housed in a vacuum chamber. The pressure vessel is cooled by an aluminium cylindrical heat exchanger, which is shown in Figure 8.6 (see also Figure 11 in Appendix 10.7). It contains a coil, which covers its entire height, inside which liquid nitrogen (LN_2) flows. Since the specific heat of aluminium is relatively high, about $880 \text{ J}/(\text{kg K})$ at $T = 25 \text{ }^\circ\text{C}$ and atmospheric pressure, the heat exchanger is very suitable for heat transfer, thus allowing the system to be cooled quickly.

If, on the one hand, this ability to effectively cool down the apparatus is an advantage since it allows to considerably reduce the time constants of the system, on the other hand, it introduces a number of problems. For example, if the sample fluid is cooled too rapidly, the measuring cell can be subjected to thermal stresses which are so high that it can be plastically deformed. In this case the screws used to fasten the reflectors and the acoustic transducer supports can bend until they crack. In addition, the piezo-ceramic transducer used as an acoustic source, when subjected to thermal shock, suffers from deformations that can break it (see Figure 8.7). When this happens, it is impossible to continue the measurements and, moreover, it is necessary to completely disassemble the apparatus in order to replace it.

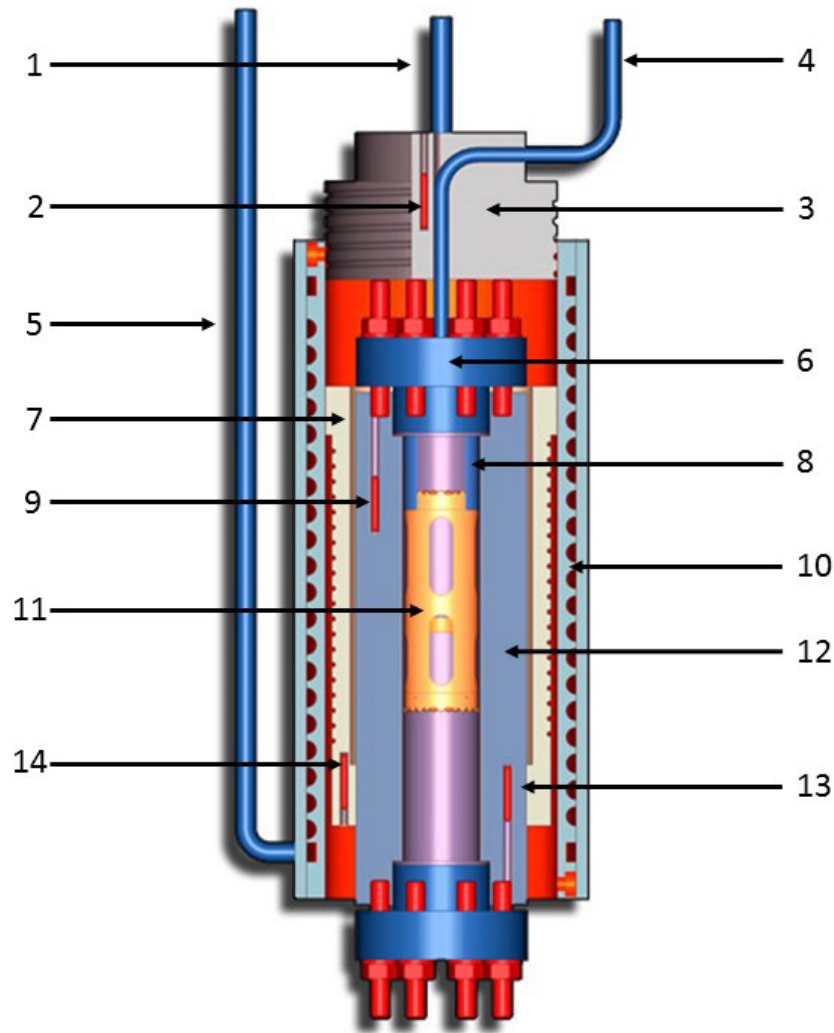


Figure 8.5: Cryogenic thermal apparatus:(1) LN₂ inlet; (2) Aluminium bridge thermometer, PT100; (3) Aluminium bridge; (4) CH₄ inlet; (5) LN₂ outlet; (6) Vessel stopper; (7) Thermal shield; (8) Coupling holders; (9) Upper thermometer, PT100; (10) Heat exchanger; (11) Measuring cell; (12) Pressure vessel; (13) Lower thermometer, PT100; (14) Thermal shield thermometer, PT100.

Therefore, it is indispensable to design a heat exchange system capable to control the speed of temperature changes, preventing the formation of many kelvin thermal gradients along the pressure vessel. A large part of the design and development work has been dedicated to the realization of the thermal shield.

Among the different solutions tested and subsequently discarded, the thermal shield shown in Figure 8.8 can be described as an example of one of the not used versions in the final configuration of the apparatus. In this case, a thermal bridge made up of a digged aluminium cylinder was used. This was placed between the heat

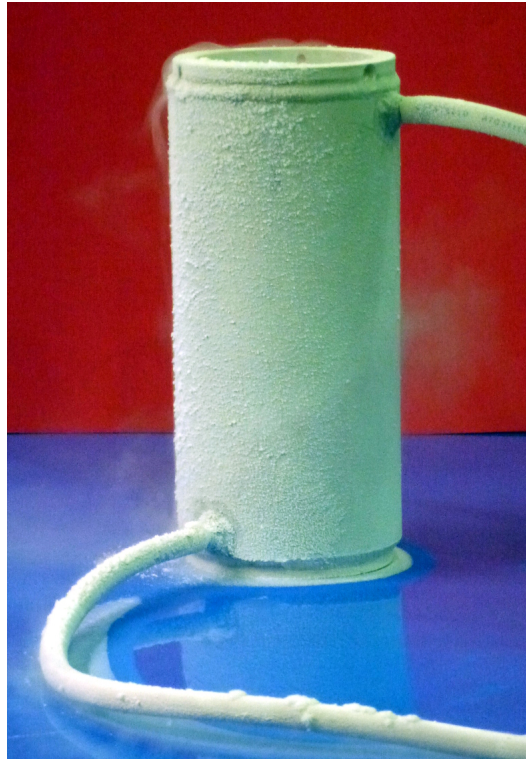


Figure 8.6: Picture of the aluminium heat exchanger during the first cooling test under uncontrolled humidity conditions.

exchanger and the pressure vessel, ensuring thermal contact on the whole of both its external and internal surfaces. The external surface, in direct thermal contact with the heat exchanger, was fitted with a coil designed to be the housing for an electric wire covered with Kapton (DUPONT™KAPTON®) insulation. This was heated in order to contrast the cooling of the pressure vessel by regulating its temperature. Despite succeeding in achieving a rapid and efficient cooling of the apparatus, it was not possible to adopt this solution due to a number of problems encountered after several refrigeration tests. For example, since the heating wire was placed on the interface between the heat exchanger and the thermal bridge, both made of aluminium, the heat was more effectively exchanged towards the heat exchanger rather than towards the pressure vessel (made of 316L stainless steel with a specific heat capacity of 490 J/kg K at $T = 25 \text{ °C}$ and atmospheric pressure). In this way it was difficult and time-consuming to control the temperature of the pressure vessel, especially when approaching the thermal equilibrium, where the temperature stability was worse than expected (better than 50 mK) by more than one order of magnitude. In addition, a major problem with this system configuration was the development of thermal gradients between the lower and upper part of the vessel. These thermal gradients could range from about 0.5 K , for higher



Figure 8.7: Picture of a broken piezo-ceramic transducer, after a thermal shock.

temperatures and up to 5 K, for lower temperatures, making it virtually impossible to associate an accurate temperature to the liquid methane contained in the vessel and, consequently, to the speed of sound measurements. This was mainly due to two factors. First, the system containing the heat exchanger and thermal bridge was asymmetrical. In fact, the inlet point of the liquid nitrogen was located in the upper part of the exchanger, while the outlet point is located in the lower part. In this way, the heat exchange takes place in an increasingly less effective way, as the liquid nitrogen, flowing downwards and absorbing heat from the walls of the heat exchanger, warmed up.

Secondly, one of the causes of the thermal gradients generation was the existence of a steady heat flow from the inside of the pressure vessel to the outside of the system. This heat flux is due to the temperature gradient between the liquid methane contained inside the pressure vessel, at cryogenic temperature, and that of the methane in the inlet tube, which reaches the same temperature as the laboratory. Although the surface of the inlet tube is relatively small, the temperature gradients become so high to produce a non negligible heat flux which perturbs the thermal equilibrium of the system. The temperature was measured with two platinum resistance thermometers (PT100), shown in Figure 8.9, placed in the walls of the aluminium heat exchanger. In this way, because of the problems met by the system in reach-



Figure 8.8: Picture of the first version of the aluminium thermal bridge used to cool down the pressure vessel.

ing thermal equilibrium, very unstable temperature measurements were obtained and, above all, these were very different (up to about 8 K higher) from the real temperature of the pressure vessel and therefore of the methane. The proof of this was given during one of the cooling checks carried out during the testing phase of the apparatus. In fact, it happened that the methane contained in the vessel solidified, even though the temperature measured by the thermometers was above the solidification temperature. The phase change of a fluid from liquid to solid can be easily detected by reading the pressure readings. When this happens, there is a sudden drop in pressure due to the fact that the volume occupied by the fluid inside the pressure vessel changes by order of magnitude. This was exactly the case while testing the possibility of cooling the apparatus down to 100 K. During this test, despite the fact that the thermometers were measuring a temperature of about 100 K, the pressure of the system fell below the atmospheric pressure, indicating that the methane had solidified and, therefore, its temperature was lower than the triple point temperature ($T = 90.69$ K).

In order to deal with these issues, it was therefore essential to design a different heat exchange system that, at the same time, was able to efficiently cool the vessel, preventing the formation of temperature gradients and limiting any unwanted heat



Figure 8.9: Picture of the two platinum resistance thermometers used to measure the system temperature.

flows.

The solution was reached by designing two distinct elements to be introduced into the apparatus to replace the existing aluminium thermal bridge: a copper thermal shield and a second aluminium thermal bridge.

The first component is a thermal shield (number 7 in Figure 8.5), whose shape and material have been chosen to enable the best possible regulation of the system temperature. Figure 12 in Appendix 10.7 shows the design schematics of this element, which can be thermally controlled by a manganin heating wire, coiled around the outer face of the copper shield in order to counteract the sudden freezing of the vessel and to stabilize the temperature at the necessary values (see Figure 8.10). It is made by copper which, having an heat capacity which is more than two times greater than that of aluminium, is suitable for a slower heat transfer from the heat exchanger to the vessel. In this way the time constants of the system are longer, but there is a significant improvement in the temperature control and stability at the equilibrium. The specific shape of the thermal shield has also been designed to avoid temperature differences between the top and bottom of the pressure vessel. As shown in Figure 8.11, this element is in a thermal contact with the bottom of the pressure vessel and the upper part of the aluminium cylindrical heat exchanger (number 10 in Figure 8.5). This special design ensures, when the system reaches a thermal equilibrium, a temperature stability better than 50 mK during the entire measurement cycle.

A platinum resistance thermometer, PT100, in thermal contact with the baseplate

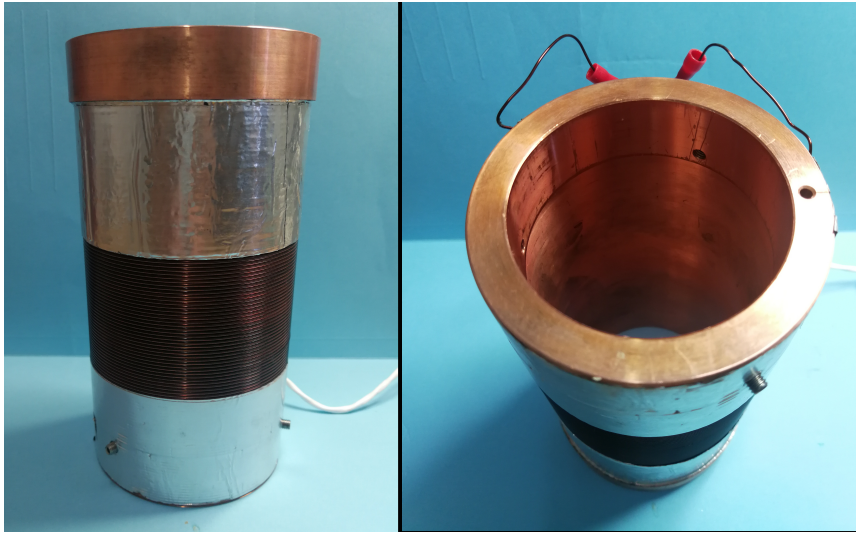


Figure 8.10: Copper thermal shield, wrapped in manganin heating wires.

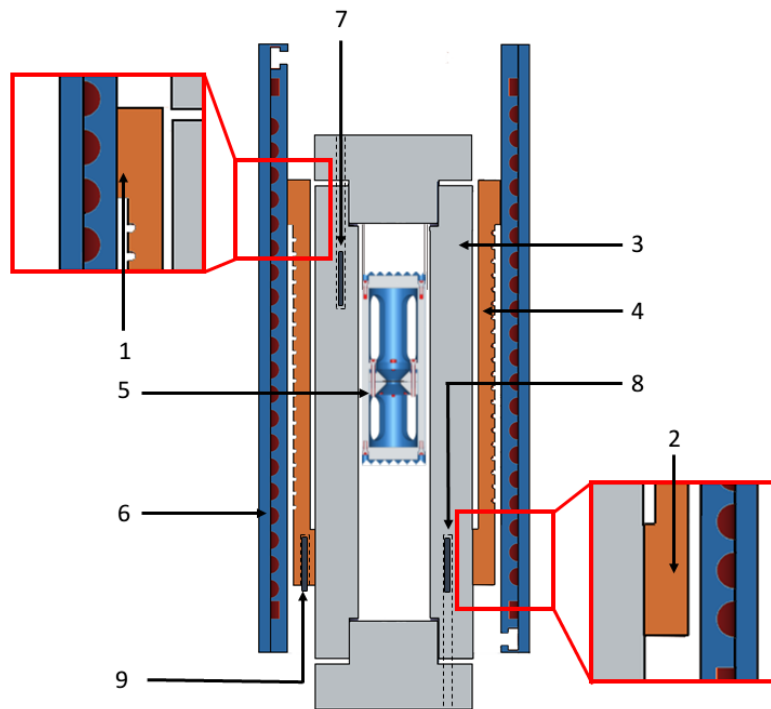


Figure 8.11: Schematics showing the heat coupling between heat exchanger, thermal shield and pressure vessel. (1) Thermal contact between heat exchanger and thermal shield; (2) Thermal contact between thermal shield and pressure vessel; (3) Pressure vessel; (4) Copper shield; (5) Ultrasonic cell; (6) Heat exchanger; (7) Upper PT100; (8) Lower PT100; (9) PID thermometer.

of the copper shield, provides the temperature of that part of the thermal shield that is the only section in contact with the pressure vessel. Two thermometers are inserted directly into the pressure vessel walls, as shown in Figure 8.12, so as to be as close as possible to the methane contained within it. In this way, unlike the



Figure 8.12: Thermometer housings into the pressure vessel walls.

previous aluminium heat exchanger, the measured temperatures at thermal equilibrium can be associated with the actual temperature of the fluid.

Despite the fact that the whole system is placed in a vacuum chamber, the inner part of the vessel is not completely thermally insulated from the outside. In fact, to inject methane into the vessel, a high pressure 1/4" inlet tube, which is directly in contact with the laboratory temperature, is connected to the upper stopper of the vessel. This configuration can lead to thermal gradients between the upper and lower edges of the vessel that can easily reach values above 5 K, at cryogenic temperatures. To eliminate this gradient, a further thermal bridge is used to cool down the upper part of the system. This component is a 6 cm high aluminium cylinder (see Figure 8.13 and Figure 13 in Appendix 10.7) that is mounted on top of the pressure vessel to cool the inlet tube through which the methane flows. A manganin heating wire wrapped around the bridge is used to control its temperature which is measured with a PT100 thermometer placed near the methane inlet tube. Finally, to further reduce the vertical thermal gradient that may occur in the system, two additional heating wires are mounted around the stoppers of the pressure vessel. These heaters can be activated separately and they operate as thermal balancers slightly heating the part of the vessel that is colder.



Figure 8.13: Aluminium thermal bridge used to cool down the inlet tube of methane.

8.3 Experimental apparatus and procedure

Each of the items and sensors constituting the apparatus is controlled by a different laboratory instrument. Figure 8.14 shows a schematic diagram describing how the apparatus is controlled and works. The temperatures of the aluminium thermal bridge, as well as that of the copper heat shield, are measured by readings the resistance values of two PT100, provided by two multimeters (Keithley 2000). Temperature of measuring cell is obtained as the mean value of the resistances measured by two PT100 placed inside the walls of the pressure vessel. The latter two thermometers are calibrated according to the international temperature scale ITS-90 [87], using the triple point of argon, the triple point of mercury and the triple point of water as calibration points, with an uncertainty of ± 0.02 K. A two-channels 8.5 digits multimeter is used to read the resistance values of both these PT100. The manganin heating wires acting on the aluminium bridge and on the thermal shield are activated by two power supplies, while the two thermal balancers are controlled by a two-outputs power supply. Cooling of the system is provided by liquid nitrogen contained in a 120 l dewar. An electro-controlled valve (Auma, Industry & Marine GmbH) is mounted between the dewar and the thermostat system. This valve is specifically designed to operate at cryogenic temperatures and it is used to adjust the flow of liquid nitrogen inside the heat exchanger.

Considering that the cooling time-constant of the system is in the order of 8÷10 hours and that the time required to take a measurement along an entire isotherm needs other 8 hours, the cryogenic valve is also used to save liquid nitrogen so that it does not run out throughout the measurement cycle. Therefore, during the cooling process from room temperature down to cryogenic temperatures, the valve is opened or closed by means of a remote control, so that the liquid nitrogen flows into the heat exchanger for 30 minutes every one hour and a half. Instead, during the measurement cycles, the valve is left open with the minimum opening to leave the system to cool down at a rate of less than 1 K/h.

Measurements are carried out for each isotherm, starting from the highest to the

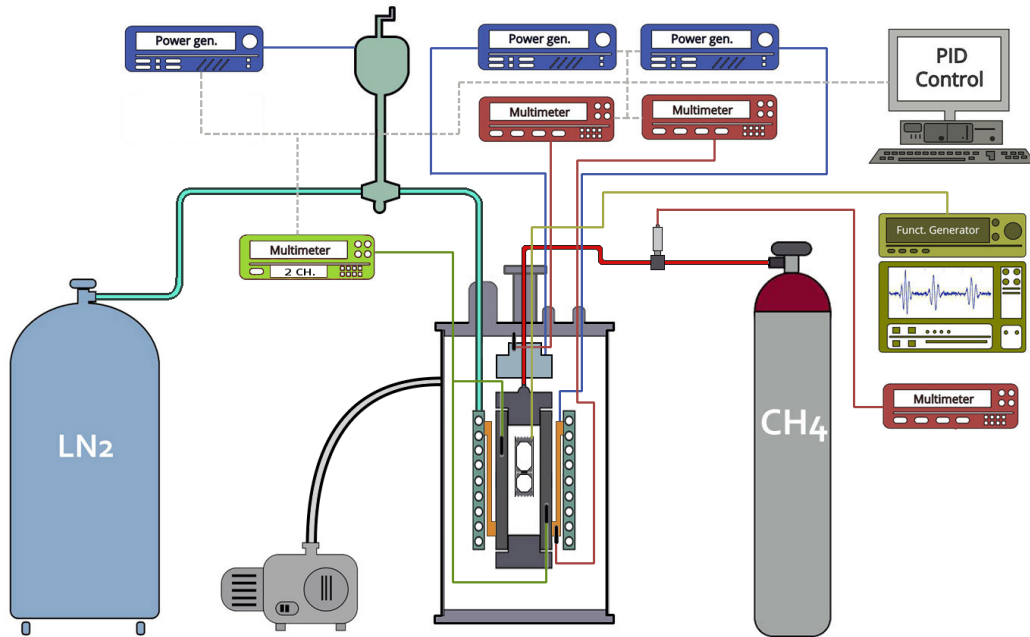


Figure 8.14: Cryogenic apparatus for measurements of speed of sound.

lowest pressure, gradually venting the methane from the pressure vessel to the atmosphere. Since, for safety reasons, it is not possible to stock liquid methane inside the pressure vessel between the isotherms, the system must be evacuated at the end of each measurement cycle, increasing the fluid temperature and opening a vent line to the outside. Pressure of the fluid within the measuring cell is measured by a temperature controlled pressure transducer (Honeywell Super TJE) placed on the hydraulic inlet line of methane, with an accuracy of ± 0.025 MPa and a working range up to 51.7 MPa. The whole system is isolated from the environment and placed in a vacuum chamber that is evacuated at a pressure of about $5 \cdot 10^{-3}$ mbar.

Chapter 9

Results and comments

Measurements were carried out along five isotherms (130, 134, 140, 150 and 162) K. For each isotherm, measurements started at the pressure of 10 MPa, down to 2 MPa with steps of about 2 MPa. Table 9.1 lists the obtained experimental results of speed of sound in liquid methane, while Figure 9.1 plots the values as a function of pressure. At any decrease of pressure, although moderate and slow over time, leads to a decrease in the methane temperature due to the expansion inside the pressure vessel. This means that it took from 30 minutes to more than an hour, depending on the temperature at which the measurements were carried out, to restore the thermal equilibrium every time the pressure was changed. The nominal pressures taken into account for each isotherm were (10, 9, 8, 6, 4 and 2) MPa, except for the isotherm at (162, 134 and 130) K, where it has been opted to perform the measurements at (4 and 8) MPa for $T = 134$ K, at 9 MPa for $T = 130$ K and at 6 MPa for $T = 162$ K. This decision has been taken because, during these measurements, it took longer to reach thermal equilibrium and, therefore, the consumption of liquid nitrogen to cool the system was higher, with the risk that it would run out before reaching the lowest pressures.

To verify the possibility that thermal stresses could lead to plastic deformation during the measuring cycles, the ultrasonic cell has been calibrated four times. The first calibration was performed before the measurement at (134 and 140) K, then before the measurement at 162 K, then a further calibration was done before the isotherms at (130 and 150) K. Finally, the cell was calibrated again after the measurements were concluded. The values of $2\Delta L$ calculated after each calibration was randomly distributed in a range of 0.01 %, showing that the cell was stable before and after each measurement.

Figure 9.1 shows the increasing trend of speed of sound with respect to increasing pressures, while it is clearly that its value increases at lower temperatures. It is also possible to see that the speed of sound is increasingly dependent on pressure, the closer it gets to the critical point ($T_c = 190.56$ K, $p_c = 4.59$ MPa).

T / K	p / MPa	$w / \text{m s}^{-1}$	T / K	p / MPa	$w / \text{m s}^{-1}$
130.03	2.13	1188.9	150.07	2.35	949.7
129.99	4.06	1212.7	150.05	4.34	988.4
129.99	6.13	1236.7	150.04	6.17	1020.3
130.06	8.05	1257.1	150.05	8.25	1053.9
130.02	10.12	1278.1	150.04	9.35	1069.7
			150.06	10.34	1082.7
133.65	2.07	1144.9	162.06	2.32	788.6
133.58	6.29	1200.3	162.07	4.16	840.2
133.68	9.22	1232.0	162.08	8.19	929.5
133.64	10.25	1243.2	162.07	9.23	949.5
			162.06	10.13	965.5
139.66	2.19	1075.3			
139.66	4.15	1104.5			
139.65	6.15	1132.5			
139.65	8.13	1158.8			
139.65	9.18	1171.4			
139.66	10.18	1184.1			

Table 9.1: Experimental values of speed of sound in liquid methane.

9.1 Uncertainty analysis

The measurement technique used in this work is based on the independent determination of both the acoustic path, ΔL , and the time of flight, τ , that an acoustic wave needs to cover the entire length within the measurement cell. In this way, by measuring the values of T and p associated with the experimental results, it is possible to calculate the speed of sound, $w(T, p)$. The uncertainty of the measurements has been estimated taking into account the different sources contributing to its total budget, so that the estimated relative uncertainty can be calculated by using the following equation for error propagation:

Relative uncertainty source	Contribution / %
Acoustic path length	0.026
Time of flight	0.004
Temperature	0.095
Pressure	0.072
Repeatability	0.177
Estimated expanded relative uncertainty ($k=2$)	<0.42

Table 9.2: List of the uncertainty sources for the calculation of the overall expanded relative uncertainty ($k = 2$) of speed of sound.

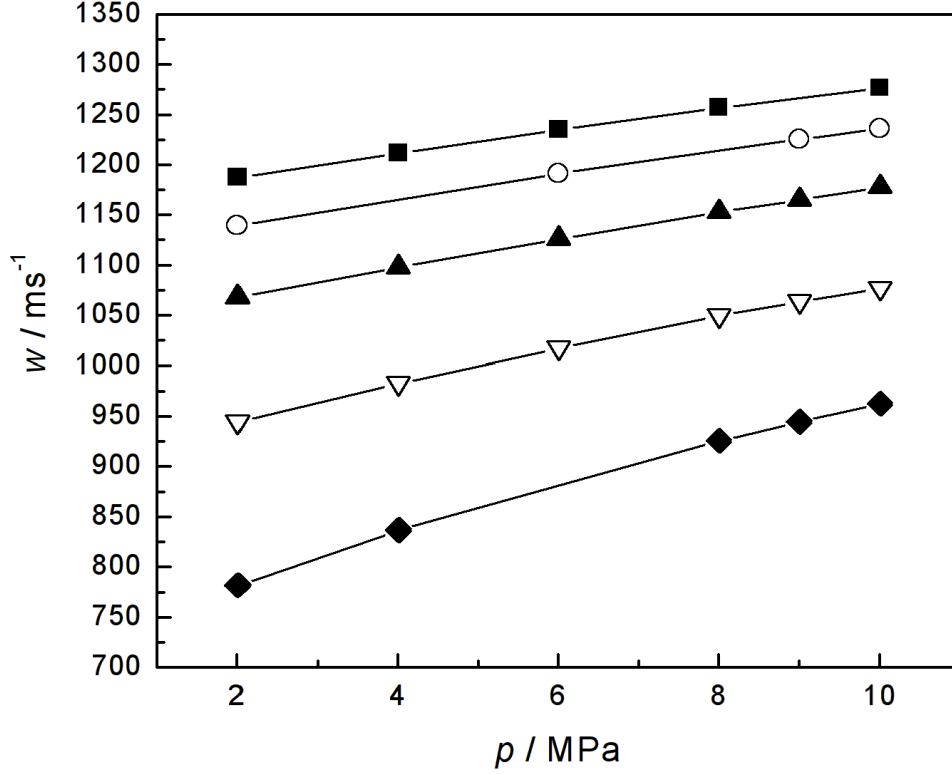


Figure 9.1: Experimental values of speed of sound in liquid methane along five isotherms. (■) $T=130$ K ; (○) $T=134$ K ; (▲) $T=140$ K ; (▽) $T=150$ K; (◇) $T=162$ K .

$$\frac{\sigma(w)}{w} = \sqrt{\left(\frac{\sigma(\Delta L)}{\Delta L}\right)^2 + \left(\frac{\sigma(\tau)}{\tau}\right)^2 + \left(\frac{\sigma(T)}{w} \frac{\partial w}{\partial T}\right)^2 + \left(\frac{\sigma(p)}{w} \frac{\partial w}{\partial p}\right)^2 + (R)^2}, \quad (9.1)$$

where R is the repeatability.

The term $\sigma(\Delta L)/\Delta L$ is the relative uncertainty associated to the acoustic path determination. Since this quantity is obtained by means of a cell calibration, using the same experimental technique adopted for the determination of speed of sound, taking as reference value the speed of sound in water, w_w , at ambient temperature, T_0 , and atmospheric pressure, p_0 , its uncertainty is calculated in a similar way as for the uncertainty of speed of sound.

$$\frac{\sigma(\Delta L)}{\Delta L} = \sqrt{\left(\frac{\sigma(w_w)}{w_w}\right)^2 + \left(\frac{\sigma(\tau)}{\tau}\right)^2 + \left(\frac{\sigma(T_0)}{w_w} \frac{\partial w_w}{\partial T_0}\right)^2 + \left(\frac{\sigma(p_0)}{w_w} \frac{\partial w_w}{\partial p_0}\right)^2}. \quad (9.2)$$

The uncertainty associated with time of flight $\sigma(\tau)$ is taken to be 10 times the oscilloscope sampling interval, namely $0.4 \cdot 10^{-9}$ s. The temperature is measured with an uncertainty of 0.02 K, which is the uncertainty related to the calibration of the thermometers, while the uncertainty associated with the pressure measurement is 0.025 MPa. Both temperature and pressure dependency factors, $\partial w/\partial T$ and $\partial w/\partial p$, are derived by fitting the experimental results of speed of sound. Finally, the repeatability value is estimated to be better than 0.18 %. This value has been determined after three different repeatability measurements at (134, 140 and 150) K. So, the expanded relative uncertainty in sound speed values is estimated to be less than 0.42 %, with a coverage factor $k=2$, over the entire region of measurements.

Table 9.2 shows the values obtained for the main uncertainty sources as well as the estimated value of the overall uncertainty of the experimental measurements of speed of sound.

9.2 Comparison of experimental SoS values to available data

The obtained experimental speed of sound values were compared with those found in literature, by interpolating the speed of sound values from the experimental data to the literature declared reference temperatures and pressures. Surprisingly, the available data are quite few in the range of temperatures and pressures involved in this work. In fact, despite there are a lot of speed of sound measurements in pure methane in the gas phase, only a few works have been carried out in liquid phase so far.

In Van Itterbeek *et al.* [44] there are 6 measurements of speed of sound at 140 K and other 6 at 155 K. Both series were carried out for pressures up to 10 MPa. Singer [84] measured 4 points at 145.6 K for pressures up to 8.5 MPa, while only two of the measurements given in Straty [43], those at 150 K and pressures of (3 and 7) MPa, are within the temperature range useful for the comparison with the results of this work. Furthermore, Baidakov [45] carried out a series of measurements at pressures between (2 and 4) MPa, providing 11 values at 150 K and 15 at 160 K, where only two points corresponding to the pressures chosen in our measurements, (2 and 4) MPa, were taken into account for the comparison. Finally, no data are currently available for speed of sound in liquid methane for temperatures between (130 and 140) K and pressures from (2 to 10) MPa.

Table 9.3 contains a list of all the available experimental values of speed of sound in liquid methane within the phase region under investigation. In this table their deviations from the values predicted by the reference equation of state of Setzmann and Wagner and by the GERG-2008 model are shown together with the deviations from the values obtained in this work, which are plotted also in Figure 9.2.

The only measurements currently available at 160 K are those of Baidakov *et al.* and deviate from the obtained measurements by less than 0.15 %, which is the uncertainty declared by the methane reference equation of state at this temperature. Otherwise, the two points at 150 K show deviations of about 0.3 %, but they are still in agreement.

The experimental results of Singer at 145.6 K show the highest deviations with respect to both the reference equation of state and the GERG-2008 model, especially for pressures at (3 and 5) MPa. These measurements, having a declared uncertainty of 0.5 %, have been excluded by Setzmann and Wagner's equation of state. However, by comparing them with the experimental results of this work, it can be observed the agreement is better than 0.18 %.

The two available measurements carried out by Straty at 150 K show the best agreement with the obtained measurements, deviating by less than 0.13 % at 7 MPa and by 0.03 % at 3 MPa. These data also show a very good agreement with the values obtained using the GERG-2008 model, deviating from them by less than 0.02 %, while the deviations from the values obtained using the reference equation of methane are slightly higher, but still less than 0.12 %.

Results and comments

Author	T / K	p / MPa	$w / \text{m s}^{-1}$	dev. from	dev. from	dev. from
				Setzmann & Wagner / %	GERG-2008 / %	INRIM / %
Van Itterbeek <i>et al.</i>	140.03	1.988	1059.5	0.01	-0.09	-0.79
	140.03	3.9344	1089.1	0.04	-0.08	-0.76
	140.03	5.8991	1117.9	-0.02	-0.17	-0.64
	140.03	7.8932	1145.3	-0.09	-0.25	-0.55
	140.03	8.8355	1157	-0.06	-0.23	-0.51
	140.03	9.788	1169.5	-0.12	-0.29	-0.48
	155.43	2.1451	872.9	0.23	0.30	-0.75
	155.43	3.9811	915.1	0.17	0.20	-0.55
	155.43	5.9295	954.5	0.14	0.12	-0.37
	155.43	7.8426	990.5	-0.01	-0.07	-0.16
	155.43	8.8761	1007.7	0.02	-0.07	-0.078
	155.43	9.7779	1022.5	-0.01	-0.11	0.16
Singer	145.6	8.5808	1100	-0.18	-0.03	-0.08
	145.6	7.2079	1080	-0.12	0.01	-0.18
	145.6	5.021	1050	-0.42	-0.32	0.09
	145.6	3.0597	1020	-0.66	-0.59	0.13
Straty	150	7.263	1036.6	-0.12	-0.02	-0.13
	150	3.02	962.1	-0.01	-0.03	0.03
Baidakov <i>et al.</i>	150	4.001	980.7	-0.01	-0.05	-0.27
	150	3.807	977.2	-0.02	-0.05	-
	150	3.625	973.5	0.01	-0.02	-
	150	3.419	970.0	-0.03	-0.06	-
	150	3.219	965.7	0.02	-0.01	-
	150	3.022	962.3	-0.03	-0.05	-
	150	2.825	958.1	0.01	-0.01	-
	150	2.631	954.5	-0.02	-0.03	-
	150	2.437	950.5	-0.01	-0.01	-
	150	2.242	946.3	0.02	0.01	-
	150	2.045	942.1	0.03	0.03	-0.37
	160	3.998	861.2	-0.04	0.05	0.09
	160	3.981	861.1	-0.08	0.01	-
	160	3.805	856.5	-0.04	0.05	-
	160	3.787	856.4	-0.08	0.01	-
	160	3.621	852.2	-0.08	0.02	-
	160	3.608	851.9	-0.08	0.02	-
	160	3.588	851.3	-0.07	0.03	-
	160	3.419	847.3	-0.10	0.00	-
	160	3.23	842.3	-0.09	0.02	-
	160	3.033	837.0	-0.07	0.04	-
	160	2.826	831.3	-0.05	0.07	-
	160	2.613	825.4	-0.04	0.08	-
	160	2.434	820.4	-0.04	0.09	-
	160	2.24	814.8	-0.03	0.11	-
	160	2.043	809.0	-0.01	0.13	0.13

Table 9.3: Available values of speed of sound in liquid methane with deviations from the predictions of the equation of state of Setzmann and Wagner and the GERG-2008 model.

Finally, the highest number of experimental speed of sound values that can be compared with our measurements is found in Van Itterbeek *et al.* For these measurements, methane with a declared purity higher than 99.95 % was used. While our experimental results are all in agreement with those of the other works found in literature, they show systematic deviations from those of Van Itterbeek. In particular, the points at 150 K are in agreement only for pressures above 6 MPa, while those at 140 K are all in disagreement with the results of this work. Since the Van Itterbeek measurements cover a wide range of pressures and temperatures and also have an uncertainty of 0.1 %, which is the lowest uncertainty among the measurements obtained in this $T - p$ region, the vast majority of them have been taken as reference values for the formulation of the equation of state [23]. Nevertheless, it

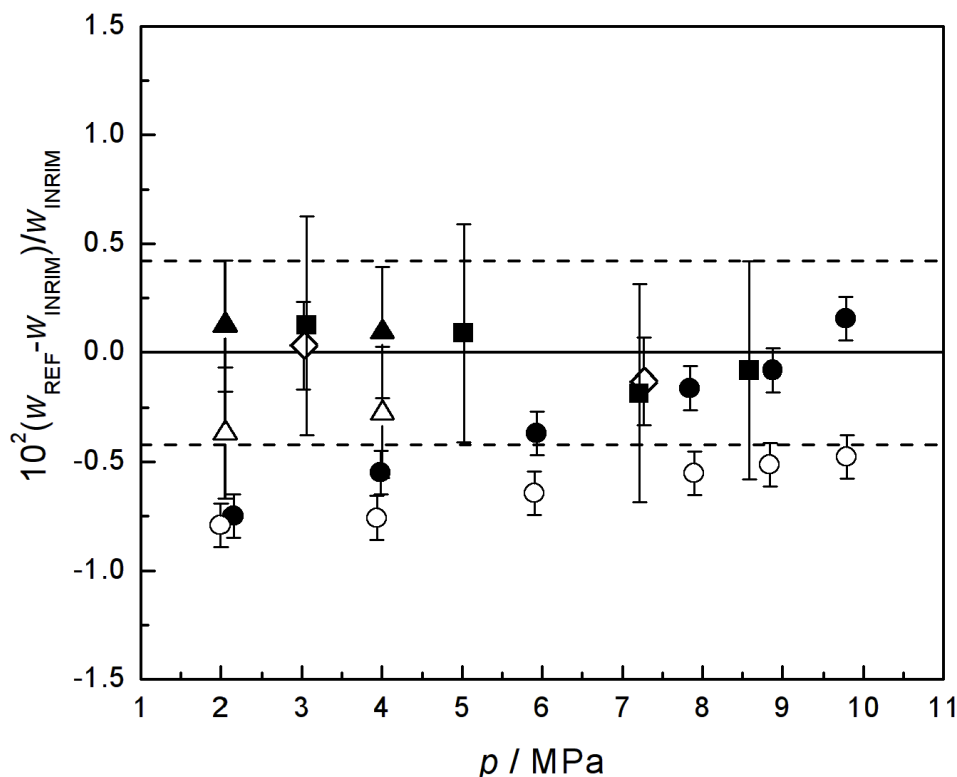


Figure 9.2: Deviations between the available experimental values of speed of sound in liquid methane, w_{REF} , and the new results obtained in this work, w_{INRIM} , for $T=160$ K and pressures between (2 and 4) MPa. (\blacktriangle) Baidakov *et al.* [45] $T = 160$ K; (\triangle) Baidakov *et al.* [45] $T = 150$ K; (\bullet) Van Itterbeek *et al.* [44] $T = 155.43$ K; (\circ) Van Itterbeek *et al.* [44] $T = 140.03$ K; (\diamond) Straty [43] $T = 150$ K; (\blacksquare) Singer [84] $T = 145.6$ K; (– –) Overall experimental uncertainty (0.42%).

is important to remark that the uncertainty associated with these measurements is not explicitly indicated in the paper of Van Itterbeek *et al.* [44]. In fact, in their work, it is stated that an accuracy of 0.1 % has been obtained after the interpolation of the values from the experimental data to the pressures and temperatures tabulated by Staes [88] in his list of density data for liquid methane. In this way, a rigorous comparison between the measurements is difficult, as the nature of the uncertainties associated with the speeds of sounds measured in this work and those associated with the Van Itterbeek measurements are substantially different.

9.3 Comparison of the results with equations of state predictions

The obtained experimental results have been also compared to the fundamental equation of state of methane [23] and to the GERG-2008 model [53]. Figure 9.3 shows that only the experimental results obtained at (150 and 162) K are consistent with the values predicted by the equation of Setzmann and Wagner, while, considering the uncertainty associated with the measurements, the results obtained at 140 K are in agreement with the equation for the highest pressures and slightly outside the tolerance limit for pressures at (2 and 4) MPa. Conversely, the measurements carried out on the isotherm at (130 and 134) K are outside the uncertainty of the equation. The experimental results were then compared with the reference values predicted by the GERG-2008 model, implemented by REFPROP [89], and the equation of state of Setzmann and Wagner, implemented from the coefficients found in the published paper [23]. Figure 9.3 shows the deviations between the experimental values of speed of sound with respect to those calculated by Setzmann and Wagner's equation, which has an estimated uncertainty for speed of sound that varies from 0.15 %, for temperatures higher than 150 K, to 0.3 % for lower temperatures. Figure 9.4 shows the deviations with respect to the GERG-2008 model. This model has been developed within the GERG group (Groupe Européen de Recherches Gazières) and is adopted as an ISO Standard (ISO 20765-2) for the calculation of thermodynamic properties of natural gases and similar mixtures. The state-of-the-art equation of state of methane, developed by Klimeck [56] in 2000, is used in the GERG-2008 model to calculate thermodynamic properties of pure methane. The estimated uncertainty for the speed of sound over the investigated pressures and temperatures, ranges from 0.5 %, above 150 K, to 1 % for lower temperatures.

Otherwise, for the GERG-2008 model the declared uncertainties in the investigated range are higher than those declared into the reference equation of Setzmann and Wagner. Figure 9.4 shows that experimental results of speed of sound are all in agreement with the values obtained from GERG-2008 except for values at 130 K and for the lower pressures of the isotherm at 134 K. Comparing our results with the values predicted by both the reference equation of methane and the state-of-the-art equation of the GERG-2008 model, it is observed that deviations increase for temperatures below 140 K. To exclude potential procedural errors or poor stability conditions during the measurement cycles at these temperatures, the measurements at 134 K were repeated three times. Figure 9.5 shows the deviations of the three repetitions with respect to the mean value of the speeds of sound measured at each pressure. The repeatability of these repeated measurements is below 0.18 %.

The disagreement between experimental values and expected values below 140 K can be explained by analysing the lack of available data in literature for speed of

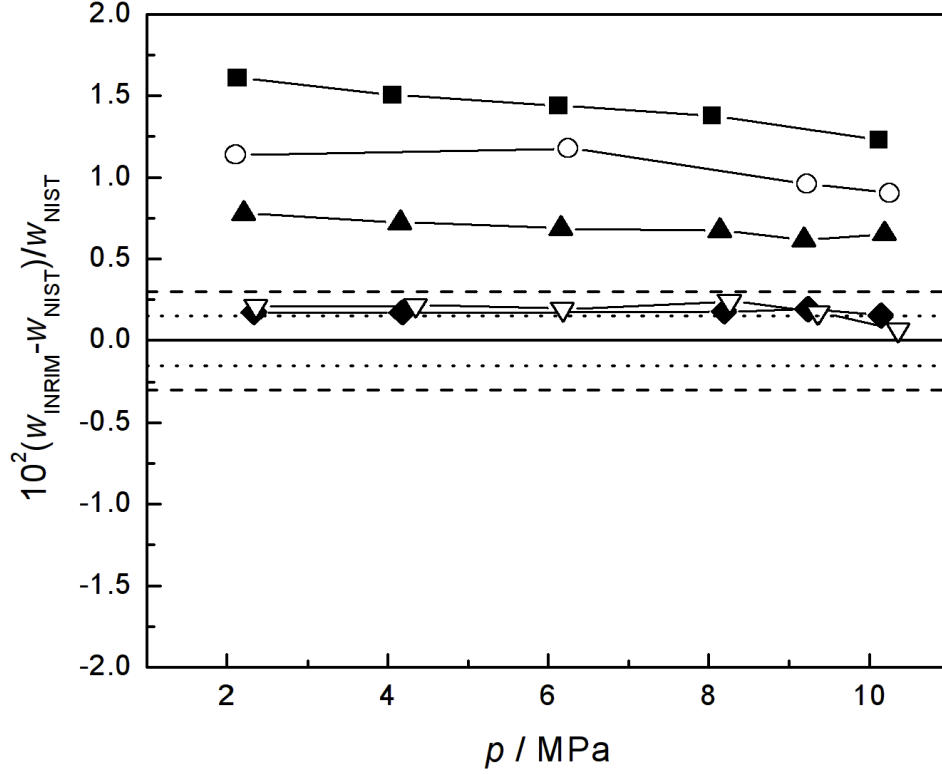


Figure 9.3: Deviations of experimental speed of sound (w_{INRIM}) of liquid methane from Setzmann and Wagner's equation (w_{NIST}). (■) $T=130$ K ; (○) $T=134$ K ; (▲) $T=140$ K ; (▽) $T=150$ K ; (◇) $T=162$ K ; (...) Tolerance for speed of sound below 150 K (0.15%); (--) Tolerance for speed of sound above 150 K (0.3%).

sound. At present there are no experimental data at all of speed of sound in methane at 130 K and for pressures between (2 and 10) MPa. Finally, it should be considered that, since the measurements of Van Itterbeek *et al.* represent the largest number of points used for fitting the equation of state, especially for $T = 140$ K, and since, at the same time, they are the only measurements that disagree with our results, it is possible that the increasing divergences, between (130 and 140) K of the experimental results here obtained with respect to those predicted by both the equation of state developed by Wagner and Setzmann and the GERG-2008 model, are mainly due to the disagreement with the results of Van Itterbeek.

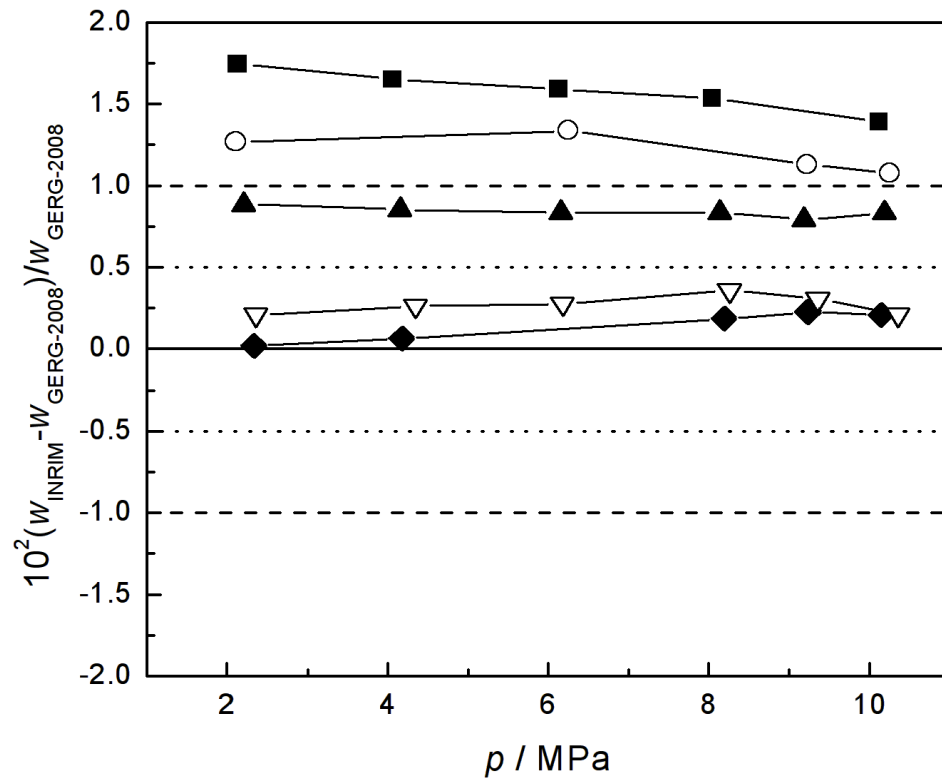


Figure 9.4: Deviations of experimental speed of sound (w_{INRIM}) of liquid methane from GERG-2008 model ($w_{\text{GERG-2008}}$). (■) $T=130$ K ; (○) $T=134$ K ; (▲) $T=140$ K ; (▽) $T=150$ K; (◇) $T=162$ K; (...) Tolerance for speed of sound below 150 K (0.5%); (--) Tolerance for speed of sound above 150 K (1%).

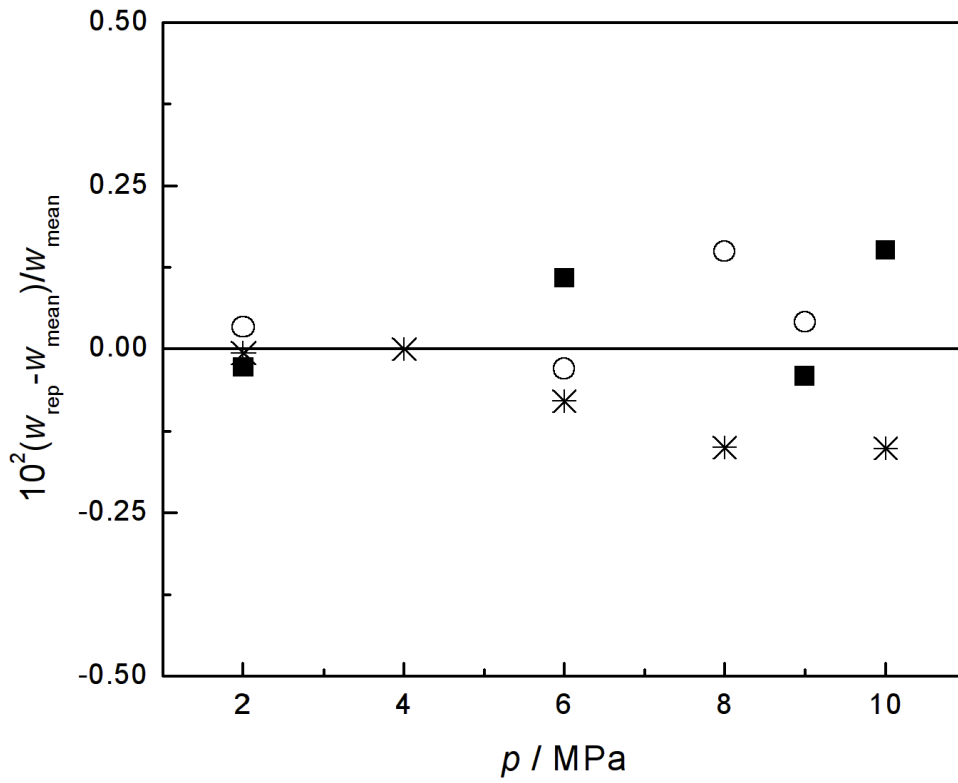


Figure 9.5: Deviations of speed of sound of three repeated measurements (w_{rep}) at $T = 134$ K from their mean value (w_{mean}). (■) First measurement (selected) ; (○) First repetition ; (*) Second repetition

Chapter 10

Density measurements of LNG mixtures

Besides the speed of sound, density is another thermodynamic property of primary importance for the development and the improvement of equations of state. Furthermore, in particular for liquefied natural gas, accurate density determination is essential for the improvement of simulation models in terms of both economic and ecological, allowing the optimization of the design of LNG distribution lines as well as the determination of the net energy transferred during the custody transfer process.

For these reasons, density measurements of a methane-isopentane mixture has been carried out for temperatures between (100 and 160) K and for pressures up to 10 MPa. The adopted experimental apparatus is described extensively in Richter *et al.* [90]. The measurement consists of weighing a silicon sinker in vacuum and when immersed in the sample. In the latter condition, only the apparent mass is weighted because of the effect of buoyancy directly traceable to the density of the fluid and the volume of the sinker. A special feature of this cryogenic densimeter is the introduction of a magnetic suspension that ensures the connection between the sinker and a precision weighing system. In this way it is possible to isolate the measuring cell containing the sample from the external environment. Therefore, it is possible to measure its density even at high pressures, as well as at extremely low temperatures.

The apparatus is equipped with a special liquid-vapour separation cell, the VLE-cell (VLE, Vapour-Liquid Equilibrium). This cell is connected directly to the fluid inlet line, above the measuring cell and after the pressure measurement circuit. The inclusion of this element ensures that the vapour-liquid equilibrium surface always takes place outside the measuring cell. This is essential to ensure that the decomposition caused by condensation and evaporation processes at the VLE interface remains restricted to the VLE-cell. In this way, changes in the composition of the

LNG mixture do not affect density measurements. To further avoid possible diffusion problems through the connection line between the VLE-cell and the measuring cell, a special high pressure hydraulic line has been designed. This connection line is a thin helical capillary tube with an inner diameter of 2 mm. Finally, to avoid change in composition, the cell is filled maintaining the sample in supercritical conditions.

10.1 Density measurement technique

In order to carry out accurate density measurement, a single-sinker method has been used. This method relies on a magnetic suspension coupling and a load compensation system. The sinker, which is a single-crystal silicon with a volume, $V_S \approx 26.16077 \text{ cm}^3$, and mass, $m_S \approx 60.95045 \text{ g}$, is immersed in the fluid inside the measuring cell. In this way the mass of the sinker while it is immersed in the fluid, $m_{S,\text{fluid}}^*$, can be calculated as:

$$m_{S,\text{fluid}}^* = m_S - \rho_{\text{fluid}} V_S(T, p), \quad (10.1)$$

where ρ_{fluid} is the density of the fluid.

However, measuring the mass of the sinker in a vacuum, $m_{S,\text{vac}}^*$, a non negligible force transmission error occurs and then $m_{S,\text{vac}}^* \neq m_S$. Then, the density of the fluid can be obtained rearranging equation 10.1:

$$\rho_{\text{fluid}} = \frac{m_{S,\text{vac}}^* - m_{S,\text{fluid}}^*}{V_S(T, p)}. \quad (10.2)$$

The measurements are carried out in two steps involving different positions of the sinker within the measuring cell. In the tare position, the sinker is set at the bottom of the cell and is not connected to the balance. In this position the balance can be tared. In the measuring position, instead, the permanent magnet is moved upward (about 1 mm) by an electromagnet placed outside the pressure-separating wall. In this position the sinker is connected to the balance via magnetic coupling and its mass can be measured. This procedure is repeated several times (at least 15 times) so that an average value of mass can be calculated.

Two compensation masses are used in order to significantly reduce drift errors of the balance. One of the reference masses is made of tantalum, $m_{\text{Ta}} = 82 \text{ g}$ ($V_{\text{Ta}} = 4.9 \text{ cm}^3$), while a second one is made of titanium, $m_{\text{Ti}} = 22 \text{ g}$ ($V_{\text{Ti}} = 4.9 \text{ cm}^3$). In the tare position the tantalum mass is placed on the balance pan, while in the measuring position the tantalum mass is removed by an automatic switching device and is replaced by the titanium mass. The advantage of having two compensation masses with the same volume is that, in this way, it is possible to eliminate the buoyancy effect of air on the masses. The balance housing is filled with gaseous

nitrogen to reduce the relative humidity and avoid the freezing of water inside the magnetic coupling house, when it reaches cryogenic temperatures.

Finally the force transmission error (FTE) of the magnetic suspension coupling has to be taken into account. This systematic error is due to the magnetic interference of the coupling house on the top of the measuring cell, which is not magnetical neutral. Furthermore the sample fluid itself is always diamagnetic or paramagnetic. This FTE effect is well described and explained in Wagner and Kleinrahm [91] and McLinden *et al.* [92]. This error can be determined by measuring the sinker mass when it is in vacuum, $m_{S,vac}^*$, and then by comparing this value with the actual mass, m_S , obtained calibrating the sinker. In this way the FTE error in vacuum, ϵ_{vac} , can be calculated as:

$$\epsilon_{vac} = \frac{m_{S,vac}^* - m_S}{m_S}. \quad (10.3)$$

Typically, the ϵ_{vac} value is less than $2 \cdot 10^{-5}$ at 293.15 K, but it reaches larger values for low temperatures. In particular, it has been estimated to range between $6.6 \cdot 10^{-5}$ at 135 K and $36.6 \cdot 10^{-5}$ at 95 K.

A additional FTE error is caused by the sample fluid, since it is not magnetic neutral. This effect can be calculated as follows

$$\epsilon_{fse} = \frac{\Delta\rho}{\rho_{fluid}} = \epsilon_\rho \left(-\frac{\chi_S}{\chi_{S0}} \right) \left(\frac{\rho_S - \rho_{fluid}}{\rho_0} \right), \quad (10.4)$$

where ρ_{fluid} is the density of the sample fluid, $\Delta\rho$ is the deviation in density due to the fluid-specific FTE error ϵ_{fse} , ϵ_ρ is an apparatus-specific constant (estimated to be $\epsilon_\rho = (5 \pm 1) \cdot 10^{-5}$ and χ_S is the specific magnetic susceptibility related to the fluid which is measured. Finally, ρ_0 and χ_{S0} are reducing constants ($\rho_0 = 1000 \text{ kg m}^{-3}$ and $\chi_{S0} = 10^{-8} \text{ m}^3\text{kg}^{-1}$).

The introduction of these corrections have to be applied to equation 10.2, which becomes

$$\rho(T, p) = \frac{m_{S,vac}^*(T) - m_{CM} - m_{S,fluid}(T, p)}{V_S(T, p)} \left(1 - \frac{\rho_{N_2}}{\rho_{St}} \right) (1 - \epsilon_{vac} - \epsilon_{fse}), \quad (10.5)$$

where $m_{CM} = m_{Ta} - m_{Ti}$ is the compensation mass, while the term $1 - \rho_{N_2}/\rho_{St}$ is the correction of the buoyancy effects on the balance, where ρ_{N_2} is the density of the dry gaseous nitrogen in the balance housing and ρ_{St} is the density of the balance calibration masses, which are made of stainless steel.

10.2 Experimental apparatus

The single-sinker densimeter used was specifically designed for cryogenic measurements of liquid mixtures. The scheme of the core apparatus is shown in figure 10.1. The measuring cell (number 7 in figure 10.1) is made of copper-berillium

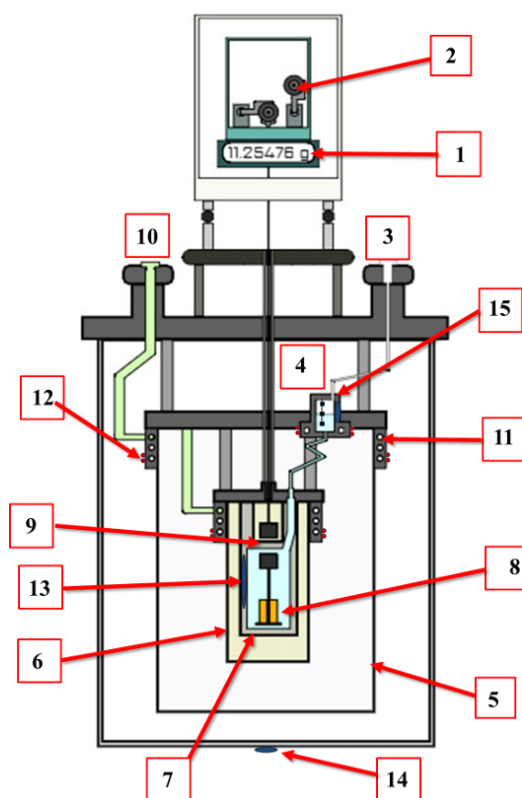


Figure 10.1: Schematic diagram of the core apparatus of the single-sinker densimeter. (1) Analytical balance; (2) Compensation weights; (3) Sample inlet; (4) Vapour-liquid equilibrium cell; (5) Intermediate shield; (6) Measuring cell shield; (7) Measuring cell; (8) Silicon sinker; (9) Magnetic coupling; (10) Liquid Nitrogen inlet; (11) Heat exchangers; (12) Electrical heaters; (13) PT25 thermometer; (14) PT 100 thermometer; (15) Liquid-level sensor.

and is connected to the intermediate heat exchanger by three stainless steel tubes. It contains the silicon sinker (number 8 in figure 10.1) and the magnetic suspension coupling (number 9 in figure 10.1). The VLE-cell (number 4 in figure 10.1) is placed at the same level as the intermediate heat exchanger and is connected to the measuring cell through a stainless steel coiled capillary. The VLE-cell is also connected in its upper end to the filling line (number 3 in figure 10.1), by an high

pressure tube. The liquid level in the VLE-cell can be measured by using an indicator (number 15 in figure 10.1) installed inside it. The entire apparatus is cooled by liquid nitrogen which is fed through an inlet tube (number 10 in figure 10.1) and can flow through three cooling states. The intermediate shield, the VLE-cell and the measuring cell can be independently thermally controlled by using three different dedicated heat exchangers placed on the top of each element. Liquid nitrogen flow can be modulated separately in each heat exchanger by using three flowmeters, namely three regulating valves in combination with rotameters, one for the intermediate shield, one for the measuring cell and one for the VLE-cell as reported in figure 10.2.



Figure 10.2: Picture of the flowmeters used to regulate the flow of liquid nitrogen in the VLE-cell, in the measuring cell and in the plate of the intermediate shield.

Furthermore the temperature of each element is stabilized through a PID control system with the use of three heating wires coiled on each heat exchanger. The entire system is placed inside an insulation cylinder, evacuated to a pressure below 5 Pa, which is suspended by a steel structure and connected to the analytical balance, as shown in figure 10.3. The temperature of the measuring cell is kept constant with a stability of about ± 0.5 mK, while the VLE-cell temperature is stable within ± 2 mK. The temperature of the intermediate shield is set to be 8 K below that of the measuring cell. When the thermal equilibrium is reached, no longer liquid nitrogen flows to the measuring cell, so it is exclusively cooled by the intermediate plate.

10.3 Pressure measurements

The pressure of the system can be measured by using three different highly accurate vibrating-quartz-crystal type pressure transducers (Paroscientific). These

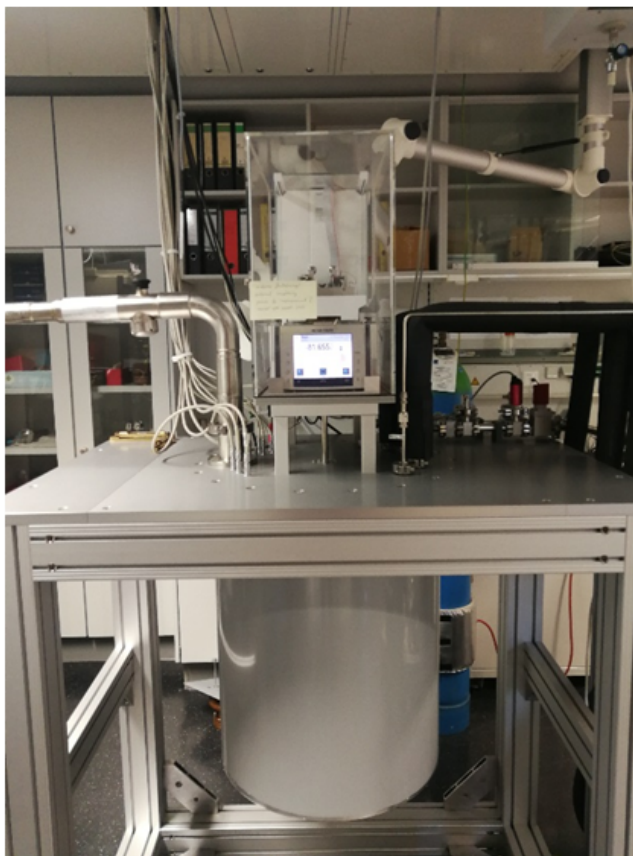


Figure 10.3: Front view of the cryogenic densimeter.

transducers are connected to the pressure line of the hydraulic circuit, on the panel of the densimeter, as shown in figure 10.4. The panel is thermostatted at 313.15 K, approximately. The transducers covers different pressure ranges with full scales of 0.69 MPa, 3.45 MPa and 13.8 MPa. For the density measurements, only the last has been used. The expanded relative uncertainty ($k=2$) associated to the pressure measurements is about 0.01% of the full scale.

10.4 Temperature measurements

To accurately measure the temperature of the measuring cell, two 25 Ω platinum resistance thermometers (SPRT, Rosemount 162D) are set into the walls of the measuring cell on opposite sides. A precision AC resistance control bridge (model F18, ASL) is used to determine their resistance ratios against a 25 Ω reference resistor (Tinsley). Both the temperatures of VLE-cell and intermediate shield are measured by two PRT 100 Ω platinum resistance thermometers (model S1059Pa,



Figure 10.4: Hydraulic circuit with the valves connected to the three pressure transmitters in evidence.

Minco) connected to a two-channel resistance bridge (millik, Isotech). Two PRT thermometers are placed to the bottoms of the radiation shields to check the vertical thermal gradients. The SPRT resistance thermometers have been calibrated at the Physikalisch-Technische Bundesanstalt (PTB) by using the ITS-90 temperature scale at the triple point of argon, mercury and water. The other PRTs thermometers have been calibrated at RUB University, by using the same fixed points, except for the triple argon point, which has been replaced by the nitrogen boiling point, using one of the SPRTs as a reference. The combined expanded uncertainty ($k=2$) for the temperature measurement, has been estimated to be about 15 mK.

10.5 Filling procedure

In order to avoid composition changes of mixtures filling the densimeter, the procedure has been shown in figure 10.5 has been used developed. The densimeter is filled at ambient temperature and at supercritical pressure (a-point). The measuring cell and the VLE-cell are cooled simultaneously until VLE cell reaches a temperature just below critical T_c at constant pressure (b-point). Then the measuring cell is cooled to the setpoint temperature T_s (c-point). At this point the sample fluid is vented from the system to reduce the pressure of the system (d-point) until the first point where a phase boundary within VLE cell appears is reached (e-point). Finally, from this point, the pressure of the system is changed by reducing temperature of the VLE cell.

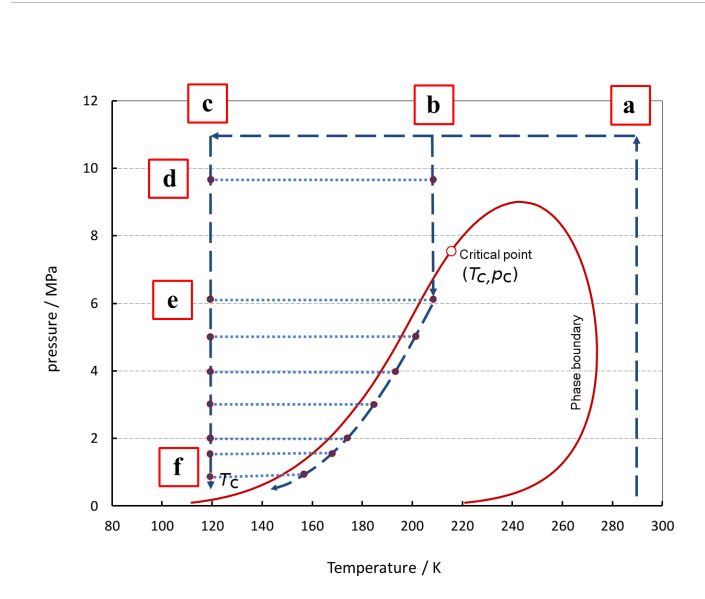


Figure 10.5: $T - p$ diagram of a typical natural gas that outlines the filling and measurement procedure.

10.6 Uncertainty budget

The determination of the uncertainty is based on the assumption that the input quantities involved during the density measurements are not correlated. The combined expanded uncertainty ($k=2$) is then given by the following equation:

$$U_c(\rho) = k \sqrt{u(m)^2 + \left(\left(\frac{\partial \rho}{\partial p} \right)_T u(p) \right)^2 + \left(\left(\frac{\partial \rho}{\partial T} \right)_p u(T) \right)^2 + u(x)^2 + u(\rho_{\text{corr}})^2 + (R)^2}, \quad (10.6)$$

The uncertainty in density $u(m)$ depends on several factors, such as the uncertainty of the analytical balance and the volume determination of the sinker. Considering all these factors, the relative standard uncertainty for this source of uncertainty is 0.0040%.

The sensitivity coefficients $(\partial \rho / \partial p)_T$ and $(\partial \rho / \partial T)_p$ can be calculated for densities of a typical natural gas from the GERG-2008 model.

The uncertainty resulting from the gas analysis $u(x)$ can be estimated as:

$$u(x) = \left(\sum_{i=1}^n \left(\frac{\Delta \rho}{\Delta x_i} u(x_i) \right)^2 \right)^{1/2}, \quad (10.7)$$

where $u(x)$ is the uncertainty of the composition of each mixture component, $\Delta \rho$ is the difference between the density calculated by using the normalized composition provided by the gas analysis certificate and the density calculated with a slightly

changed composition Δx_i of the i -th component.

The repeatability R has been determined to be better than 13 ppm.

Finally the uncertainty $u(\rho_{\text{corr}})$ related to the correction terms for the force transmission error has been calculated to be 0.0175%.

Table 10.1 shows the uncertainty budget for the measurement of the density of cryogenic liquid mixtures

Uncertainty source	Contribution / %
Density measurement	0.0040
Pressure	0.0001
Temperature	0.0030
Composition	0.0060
Repeatability	0.0013
Correction terms	0.0175
Estimated expanded uncertainty ($k=2$)	<0.0384

Table 10.1: List of the standard uncertainties for the calculation of the overall uncertainty (with $k = 2$) of density.

10.7 Preliminary results and comments

Densities of a binary LNG mixture (98% methane and 2% isopentane) along four isotherms (100, 120, 140 and 160) K and for pressures up to 10 MPa have been measured. Then, the experimental results have been compared with four equations of state. The GERG-2008 model [53], the EOS-LNG equation of state [93], which is an enhanced version of the GERG-2008 equation of state that is the best candidate to be used as an international standard for the calculation of thermodynamic properties of LNGs in the next future. Further comparisons have been carried out also with the COSTALD3 model [94], which is a well-established correlation method for the determination of densities of compressed liquids and liquid mixtures. Finally, a last comparison have been carried out by using the ERKM equation of state [95], which is an improvement of the Klosek and McKinley method, RKM [96], for density calculations of liquefied natural gas. Relative deviations between experimental data and density values calculated by these four different models (ERKM, GERG-2008, COSTALD3 and EOS-LNG) are shown in figures 10.6, 10.7, 10.8 and 10.9. Since the working range for the ERKM equation of state is for temperatures between (100 and 135) K, values at $T=140$ K have been extrapolated to be compared with the experimental results, while this model has not been included at all for the comparison at $T=160$ K. Moreover, the uncertainties declared by the ERKM for the $T - p$ of my interest is 0.1%, for temperatures below 115 K and 0.15%, for temperatures higher than 115 K. For the COSTALD model the uncertainty on the

density prediction is 0.369%, while, being EOS-LNG based on the same mathematical approach of the GERG-2008 equation, for both GERG-2008 and EOS-LNG equations of state the declared uncertainty is the same, ranging from 0.5% to 1%.

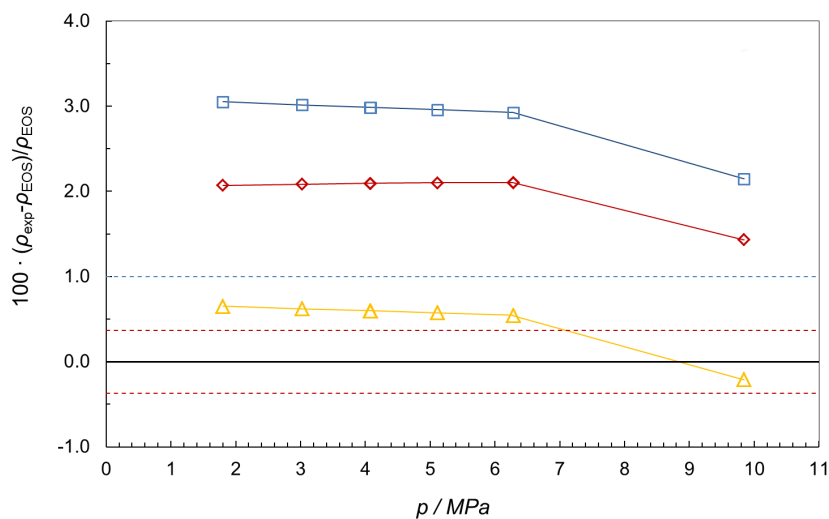


Figure 10.6: Relative deviations between experimental density measurements and the values predicted by COSTALD3 (red), GERG-2008 (blue) and EOS-LNG (yellow) for $T=160$ K. Dotted lines represent the uncertainties declared by the different equations of state. Uncertainties of experimental densities are included in the symbols.

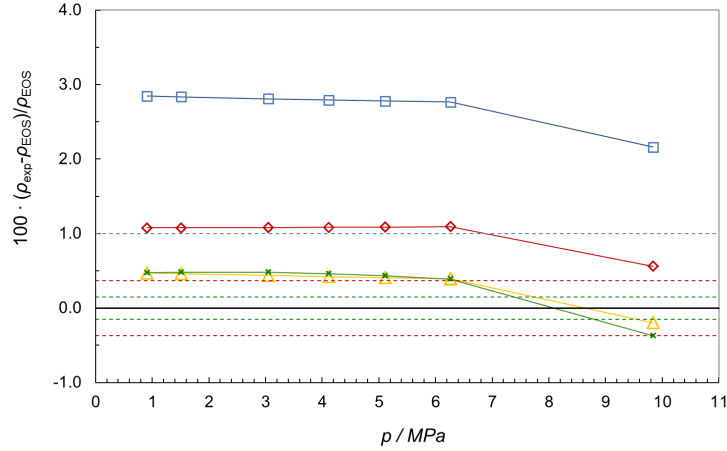


Figure 10.7: Relative deviations between experimental density measurements and the values predicted by COSTALD3 (red), ERKM (green), GERG-2008 (blue) and EOS-LNG (yellow) for $T=140$ K. Dotted lines represent the uncertainties declared by the different equations of state. Uncertainties of experimental densities are included in the symbols.

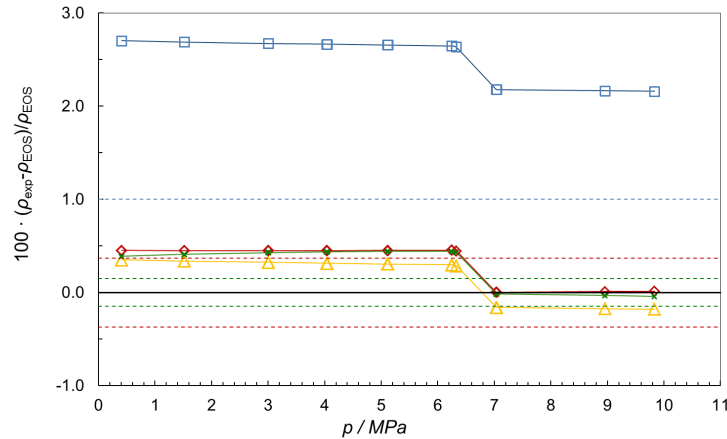


Figure 10.8: Relative deviations between experimental density measurements and the values predicted by COSTALD3 (red), ERKM (green), GERG-2008 (blue) and EOS-LNG (yellow) for $T=120$ K. Dotted lines represent the uncertainties declared by the different equations of state. Uncertainties of experimental densities are included in the symbols.

By looking at the deviation plots, it is clearly visible that GERG-2008 shows the larger deviations along all isotherms while EOS-LNG shows the best agreement with the experimental data at each temperature. In particular, the experimental results deviate from GERG-2008 calculated density by more than 2.5%. Experimental densities are not consistent with the ERKM predictions for temperature of 140 K, while a good agreement is shown for 120 K and 100 K, but only for

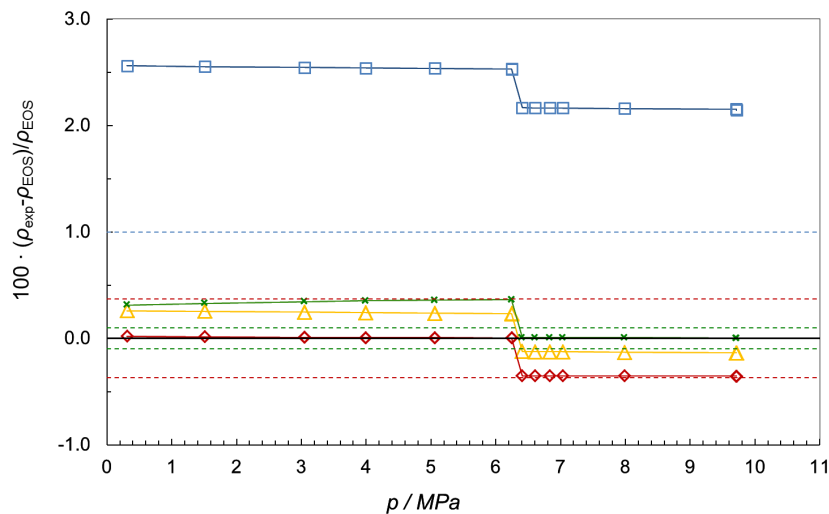


Figure 10.9: Relative deviations between experimental density measurements and the values predicted by COSTALD3 (red), ERKM (green), GERG-2008 (blue) and EOS-LNG (yellow) for $T=100$ K. Dotted lines represent the uncertainties declared by the different equations of state. Uncertainties of experimental densities are included in the symbols.

$p > 6.2$ MPa, while for lower pressures the deviations are larger than the tolerance of the equation.

Finally, COSTALD model shows a decreasing relative deviations with decreasing temperatures. Its predictions are beyond the uncertainty for (160 and 140) K, slightly over the uncertainty for 120 K at low pressures and in agreement at 100 K. In conclusion, the experimental density data obtained in this work are in excellent agreement with the values predicted by the EOS-LNG, while they are inconsistent with the data obtained with GERG-2008. This is an indication of how likely the new EOS-LNG equation of state, which was developed specifically to replace GERG-2008 as the standard for calculating the thermodynamic properties of natural gases during LNG custody transfer, performs much better in predicting the density values of LNG mixtures at the considered temperatures.

Beside these observations, a further comment can be made looking at the preliminary results. In fact, a sudden shift in relative deviation is present in each isotherms for p lower than 6.2 MPa. A possible explanation for this behavior could be some mistakes during the filling procedure, such as composition changes of the mixture, as well as a solidification of the isopentane content, which is the heaviest component of the component, at pressures higher than 6.2 MPa. To exclude any possible errors in the measurement procedure, especially in the proximity of 6.2 MPa, which is close to the saturation curve of this LNG mixture, some additional

measurements have been carried out at $T = 120$ K and $T = 100$ K between the first supercritical point (10 MPa) and the first point where mixture have been measured in its liquid phase (6.2MPa). This test has been made specifically to check whether, as the saturation curve is approached, the density changed continuously. On the contrary, as shown in figure 10.9, the deviation shift seems to be still sudden. This would be a clue that the mixture is crossing the phase boundary. In this way the isopentane could solidify during the cooling and, being heavier, could deposit somewhere between the VLE-cell and the measuring cell, thus changing the composition of the LNG mixture and, therefore, its density.

A possible solution for this type of problem could be to carry out a new cycle of density measurements, changing the filling procedure of the LNG mixture, so as to fill the measuring cell at a pressure higher than 10 MPa. Unfortunately, the pressure transmitter available for this experiment had an working pressure range up to 13.8 MPa. So, as a precaution, it was decided not to take the risk of damaging it. However, In the next future it may be possible to replace this instrument with another one with a wider working range, so that new measurements can be carried out.

Conclusions

This work of thesis described the theoretical bases that underlie the experimental measurements of speed of sound in liquid phase fluids and the principles of operation of the most used experimental techniques to obtain these measurements. A new experimental apparatus specifically designed to carry out speed of sound measurements at cryogenic temperatures and up to high pressures has been presented, describing its operation and design process, in particular, the elements of the apparatus that have been designed to cool the measuring fluid down to cryogenic temperatures. The entire apparatus has been assembled so that it can liquefy the sample without damaging the acoustic transducer and without deforming the measuring cell as a result of thermal stress. In addition, the temperature control system has been reviewed many times before being able to achieve needed performance, both in terms of stability and accuracy. Now, in a condition of thermal equilibrium, it is possible to get a thermal stability better than 50 mK needed to perform speed of sound measurements along an entire isotherm. At the same time, the apparatus has been arranged for maintaining the thermal gradient, along the measuring cell, below 80 mK. The development of this experimental apparatus was also conceived with the aim of bringing some possible technological and industrial advantages to the production and distribution of natural gas. In fact, the devices used to measure thermodynamic properties of LNG during the custody transfer process depend on calibrations of limited accuracy. This implies that even today, they cannot be calibrated with an absolute accuracy better than a few percent. The ultrasonic cell here developed can be used as transfer standard for on-line calibration of ultrasonic flowmeters used to monitor LNG, when it has been characterized in laboratory conditions by using a proper fluid or mixture at cryogenic temperature.

Accurate measurements of speed of sound in pure methane have been done for temperatures between (130 and 162) K and pressures up to 10 MPa. The expanded relative uncertainty associated to the experimental speed of sound values has been estimated to be less than 0.42 %, with a coverage factor $k = 2$, over the entire region of measurements, while the repeatability of measurements, estimated to be better than 0.18 %, have been determined by three different repeated measurements at (134, 140 and 150) K respectively.

The experimental measurements obtained in this work have been compared with the data available in the literature. This comparison showed that the results are in disagreement with those performed by Van Itterbeek, where deviations rise up to about 0.8 %, especially for lower pressures and at 140 K. A deeper insight revealed that Van Itterbeek carried out measurements covering a wide range of pressures and temperatures, stating an uncertainty of 0.1 %, but that estimation was not based on a critical analysis of the uncertainty, conversely, it was the relative residue of the fitting procedure. Unfortunately there were not enough information to try to understand the origin of the disagreement. However, all the other available experimental measurements have shown an agreement with the here reported results much better than their combined uncertainties. Nowadays, obtained measurements constitute one of the most accurate available results. For the next future, new measurements at lower temperature, below 100 K, will be carried out.

Tables of experimental speed of sound measurements

N	T / K	p / MPa	$w / \text{m s}^{-1}$	N	T / K	p / MPa	$w / \text{m s}^{-1}$
1	94.0	^a	1509.0	15	140.24	0.6512	1035.3
2	94.35	^a	1507.0	16	144.50	0.8051	986.7
3	96.10	^a	1489.8	17	149.01	0.9954	933.3
4	98.49	^a	1466.6	18	153.78	1.2337	875.7
5	101.78	^a	1433.9	19	158.01	1.4788	822.2
6	105.44	^a	1400.0	20	162.80	1.7828	759.1
7	109.09	^a	1363.8	21	167.48	2.1261	694.3
8	112.79	^a	1326.8	22	172.00	2.4997	620.2
9	116.08	^a	1293.3	23	176.42	2.9145	558.1
10	119.76	^a	1256.0	24	179.44	3.145	506.0
11	123.82	^a	1214.5	25	182.48	3.5686	449.0
12	127.97	^a	1170.3	26	185.90	3.9678	374.3
13	131.98	^a	1127.2	27	187.52	4.1943	331.5
14	136.18	^a	1081.0	28	189.57	^a	273.0

Table 2: List of experimental speed of sound of methane obtained by Van Dael *et al.* These data are referred to temperatures between (94 and 190) K along the saturation line. ^a Pressures extrapolated by using the vapour pressure data by Keyes *et al.*

Tables of experimental speed of sound measurements

T / K	p / MPa	$w / \text{m s}^{-1}$	T / K	p / MPa	$w / \text{m s}^{-1}$	T / K	p / MPa	$w / \text{m s}^{-1}$
111.33	0.1124	1340.9	125.10	0.2807	1200.6	140.03	0.6475	1038.5
	0.5046	1345.0		0.5300	1202.9		1.1115	1045.0
	0.9808	1349.6		1.0102	1209.0		1.9880	1059.5
	1.9728	1358.7		1.9910	1220.8		2.9810	1075.0
	2.9374	1367.0		2.9577	1232.1		3.9344	1089.1
	3.9324	1376.6		3.9172	1242.7		4.9305	1104.0
	4.9132	1384.8		4.8636	1253.8		5.8991	1117.9
	5.8839	1393.1		5.9235	1265.1		6.8465	1130.6
	6.8161	1402.1		6.8465	1275.0		7.8932	1145.3
	7.5690	1408.5		7.5933	1285.0		8.8355	1157.0
				8.7747	1295.0		9.7880	1169.5
				9.7880	1305.2		10.6087	1178.7
							11.0343	1183.9
155.43	1.3679	854.0	170.73	2.4024	646.8	185.88	3.9719	373.6
	2.1451	872.9		3.0012	672.2		4.5211	450.0
	2.9151	891.3		3.9567	710.2		5.0034	494.8
	3.9811	915.1		4.9153	743.7		5.9336	603.0
	4.9528	935.5		7.8426	826.0		7.8932	646.6
	5.9295	954.5		8.8761	849.9		8.9267	685.6
	6.7371	970.5		9.8285	871.1		9.8083	707.4
	7.8426	990.5		10.6898	890.3		10.8114	733.7
	8.8761	1007.7		11.6726	909.0		11.8246	766.8
	9.7779	1022.5		12.6960	927.9		13.2533	800.6
	10.8418	1038.6		13.5776	944.1		14.8137	836.3
	11.8145	1053.6		14.6110	961.4		15.8878	856.1
	12.7771	1068.6		15.6142	977.9		17.3570	884.2
	13.7701	1080.9		16.8706	995.3		18.3398	901.8
	14.7732	1094.9		18.2892	1015.6			
190	4.5525	264.2						
	4.7755	340.2						
	5.2952	415.6						
	5.9528	482.3						
	6.8405	539.8						
	7.7919	590.9						
	8.8558	634.5						
	10.1021	677.7						
	11.3484	715.7						
	12.5744	748.8						
	13.7903	778.2						
	15.0366	807.2						
	16.3336	833.3						
17.5090	855.1							
18.7350	878.5							
19.9712	900.5							

Table 3: Experimental speed of sound data by Van Itterbeek *et al.* in the temperature region between the triple point and the critical point and for pressures up to 18 MPa

T / K	p / MPa	$w / \text{m s}^{-1}$
90.0	0.01347	1531
93.6	0.01893	1509
97.7	0.02946	1472
99.9	0.03680	1444
101.1	0.04159	1430
103.6	0.05333	1406
105.2	0.06026	1388
110.1	0.09239	1347
115.5	0.14692	1285
118.2	0.18238	1262
121.0	0.22393	1236
124.7	0.29384	1201
127.3	0.36477	1173
131.6	0.44077	1125
133.7	0.50156	1101
137.7	0.67888	1063
143.3	0.84100	994
147.4	0.97779	954
152.9	1.29696	885
156.2	1.45401	848
160.1	1.76306	795
164.4	1.98597	741
168.8	2.42167	672
171.7	2.47740	637
176.5	3.05495	560
177.8	3.23227	536

Table 4: Experimental data of speed of sound shown in Blagoi *et al.*

T / K	p / MPa	$w / \text{m s}^{-1}$
94.0	0.1648	1520
105.0	0.1648	1485
111.9	3.0204	1380
112.0	8.7279	1430
112.0	0.1648	1350
112.1	6.1292	1400
113.0	0.2354	1330
113.6	0.7747	1332
114.0	1.3827	1335
115.0	2.6478	1340
117.0	5.0995	1345
124.9	5.8840	1260
125.0	7.9434	1282
125.0	3.5402	1240
125.0	0.3432	1200
125.1	8.7377	1295
125.1	1.0199	1210
145.6	8.5808	1100
145.6	7.2079	1080
145.6	5.0210	1050
145.6	3.0597	1020
145.6	1.8240	980
145.6	0.8630	970

Table 5: Experimental data of speed of sound shown in Singer [84].

Tables of experimental speed of sound measurements

T / K	p / MPa	$w / \text{m s}^{-1}$	T / K	p / MPa	$w / \text{m s}^{-1}$	T / K	p / MPa	$w / \text{m s}^{-1}$
100	33.385	1672.6	120	31.161	1517.2	150	34.530	1339.6
	26.077	1630.7		26.233	1482.8		28.845	1290.0
	19.123	1588.1		19.980	1436.0		23.669	1240.3
	13.088	1548.5		15.149	1397.0		18.433	1184.6
	7.244	1507.4		9.258	1345.2		12.667	1114.5
	1.661	1465.1		4.367	1290.5		7.263	1036.6
						3.020	962.1	
170	31.457	1183.8	184	34.254	1129.0	210	34.074	987.0
	26.994	1135.5		27.883	1055.1		27.598	898.0
	20.773	1059.2		22.511	982.8		22.264	809.8
	17.538	1013.9		17.863	909.0		17.486	711.5
	13.012	940.7		13.839	831.9		14.832	643.9
	7.774	833.5		10.436	751.2		12.703	577.5
	4.528	742.9		7.722	666.6		10.944	511.5
		5.770	579.9	10.173	477.0			
		5.301	552.8	9.646	451.2			
240	34.638	863.5	270	34.769	771.5	300	34.838	713.9
	29.111	782.7		30.486	711.2		29.732	649.5
	24.656	707.0		25.972	641.6		27.295	618.0
	20.885	632.6		21.837	572.8		24.427	580.4
	18.890	588.8					20.983	537.3
	16.841	540.2						
	15.186	498.4						
	14.071	469.8						

Table 6: Experimental speed of sound data measured by Straty along nine isotherms from (100 to 300) K

Tables of experimental speed of sound measurements

T / K	p / MPa	$w / \text{m s}^{-1}$	T / K	p / MPa	$w / \text{m s}^{-1}$	T / K	p / MPa	$w / \text{m s}^{-1}$	T / K	p / MPa	$w / \text{m s}^{-1}$	T / K	p / MPa	$w / \text{m s}^{-1}$
323.15	24.5951	574.275	190.56	4.6008	196.622	191.45	4.6464	251.747	189.97	4.5156	230.008	189.4	4.4358	239.112
298.15	2.3782	441.932	190.56	4.6017	205.441	191.45	4.6833	244.533	189.65	4.4707	235.898	188.7	4.3362	246.171
298.15	5.6265	437.143	190.56	4.6035	217.041	191.45	4.7047	236.834	189.65	4.4706	235.895	188.6	4.3255	245.951
298.15	10.4914	444.612	190.56	0.7708	350.523	191.45	4.7170	229.47	189.5	4.4475	239.293	188.15	4.2658	248.233
298.15	15.2048	474.503	190.56	1.5381	337.603	191.45	4.7248	224.5	189.65	3.8610	282.858	187.6	4.1892	251.266
298.15	19.4185	518.248	190.56	2.2034	325.269	191.45	4.7297	223.725	189.65	4.0833	274.505	187.45	4.1734	251.235
298.15	20.7023	533.881	190.56	2.7602	313.885	191.45	4.7310	224.11	189.65	4.2452	266.685	186.1	3.9933	256.148
273.15	16.1782	478.358	190.56	3.2263	303.216	191.45	4.7379	229.211	189.65	4.3568	258.907	185.9	3.9745	256.001
248.15	12.8156	430.906	190.56	3.6026	293.55	194.45	4.7483	240.216	189.65	4.4239	251.024	184.15	3.7514	260.502
223.15	9.3196	371.557	190.56	3.9022	284.674	190.85	4.5329	256.124	189.65	4.4633	240.54	183.9	3.7295	260.357
198.15	5.7043	282.593	190.56	4.1331	276.519	190.85	4.5859	248.605	188.15	0.7605	348.022	183.15	3.6410	261.707
193.05	0.7820	353.203	190.56	4.3037	268.995	190.85	4.6163	239.79	188.15	1.5147	334.755	181.55	3.4511	264.742
193.05	1.5634	340.636	190.56	4.4248	261.718	190.85	4.6316	228.869	188.15	2.1645	322.081	181.3	3.4289	264.778
193.05	2.2445	328.687	190.56	4.5012	254.701	190.85	4.6384	215.771	188.15	2.7051	310.304	178.25	3.0977	269.019
193.05	2.8196	317.712	190.56	4.5504	246.568	190.85	4.6415	205.056	188.15	3.1528	299.227	178.05	3.0798	269.133
193.05	3.3055	307.52	190.56	4.5769	236.289	190.85	4.6430	204.443	188.15	3.5090	289.084	174.25	2.6986	273.676
193.05	3.7029	298.268	190.56	4.5885	220.997	190.85	4.6433	205.086	188.15	3.7870	279.652	173.95	2.6781	273.64
193.05	4.0253	289.92	190.56	4.5915	200	190.85	4.6455	212.879	188.15	3.9947	270.868	173.15	2.6047	274.444
193.05	4.2807	282.391	190.43	4.4950	254.417	190.85	4.6500	225.867	188.15	4.1404	262.389	169.15	2.2408	278.637
193.05	4.4777	275.653	190.43	4.5433	246.106	190.63	4.5133	255.237	188.15	4.2350	253.453	168.55	2.2092	278.319
193.05	4.6258	269.52	190.43	4.5690	235.517	190.63	4.5636	247.35	183.15	0.7385	342.628	163.15	1.8030	281.891
193.05	4.7289	264.169	190.43	4.5798	218.296	190.63	4.5916	237.687	183.15	1.4648	328.612	162.65	1.7301	283.814
193.05	4.8058	258.943	190.25	4.2866	268.323	190.63	4.6046	224.475	183.15	2.0827	315.097	161.45	1.6868	282.775
193.05	4.8592	254.076	190.25	4.4049	260.914	190.63	4.6093	204.088	183.15	2.5869	302.413	155.05	1.1728	290.524
193.05	4.8968	249.849	190.25	4.4786	253.658	190.63	4.6103	191.256	183.15	2.9945	290.4	153.15	1.1964	285.785
193.05	4.9242	246.74	190.25	4.5249	244.96	190.63	4.6110	195.161	183.15	3.3068	279.153	150.65	1.0713	286.265
193.05	4.9459	245.667	190.25	4.5486	233.226	190.63	4.6110	195.541	183.15	3.5366	268.394	148.15	0.9559	286.569
193.05	4.9618	246.821	190.43	4.5816	206.833	190.63	4.6123	205.872	173.15	0.6941	331.525	143.15	0.7524	286.599
193.05	4.9659	247.511	190.37	4.5721	215.768	190.63	4.6145	219.05	173.15	1.3632	315.819	138.15	0.5330	288.183
193.05	4.9878	253.098	190.35	4.5693	215.594	190.56	4.5067	254.955	173.15	1.9145	300.423	133.15	0.4420	284.566
193.05	5.0157	263.073	190.25	4.5555	220.834	190.56	4.5565	246.931	173.15	2.3436	285.724	123.15	0.2380	279.905
191.45	4.5868	258.438	190.03	4.5233	229.711	190.56	4.5837	236.959	163.15	0.6493	319.904	113.15	0.1144	272.829
190.56	4.6005	184.178	153.15	0.6038	307.741	190.56	4.5959	222.769	163.15	1.2594	302.216			
190.56	4.6010	197.982	143.15	0.5574	294.865	190.56	4.5998	199.11	163.15	1.7396	284.621			

Table 7: Experimental speed of sound given by Gammon and Douslin remote from phase boundary and near the vapour phase boundary

T / K	p / MPa	$w / \text{m s}^{-1}$
190.50	4.5920	200.329
190.50	4.5924	203.113
190.50	4.5923	203.441
190.50	4.5924	203.650
190.50	4.5939	215.448
190.43	4.5826	209.065
190.43	4.5836	217.731
190.25	4.5563	224.454
190.25	4.5571	227.131
189.65	4.4715	259.028
189.65	4.4722	259.708
188.15	4.2669	314.120
188.15	4.2674	314.180
185.91	3.9771	374.235
183.15	3.6422	434.917
183.15	3.6425	435.018
178.15	3.0917	528.374
173.15	2.6053	610.008
170.75	2.3939	646.470
163.15	1.7315	754.098
155.44	1.3210	854.358
153.15	1.1975	882.779
143.15	0.7533	1001.887
140.02	0.6431	1037.585
133.15	0.4428	1113.923
125.09	0.2713	1200.312
123.15	0.2388	1220.555
113.15	0.1151	1322.651

Table 8: Experimental data of speed of sound measured by Gammon and Douslin near the liquid phase boundary.

Tables of experimental speed of sound measurements

T / K	p / MPa	$w / \text{m s}^{-1}$	p / MPa	$w / \text{m s}^{-1}$
150	4.001	980.7	1.459	930
	3.807	977.2	1.265	925.8
	3.625	973.5	1.068	921.5
	3.419	970	0.949	918.7
	3.219	965.7	0.871	917.1
	3.022	962.3	0.756	914.4
	2.825	958.1	0.679	912.7
	2.631	954.5	0.563	910
	2.437	950.5	0.485	908.3
	2.242	946.3	0.287	903.7
	2.045	942.1	0.168	900.7
	1.851	938.3	0.101	899.2
	1.658	934.2	0.098	899.1
	155	3.999	922.5	1.85
3.806		918.3	1.656	868.5
3.609		914.4	1.459	863.7
3.417		909.9	1.264	858.5
3.218		905.8	1.146	855.5
3.022		901.3	1.068	853.4
2.827		896.8	0.949	850.3
2.632		892.2	0.871	848.2
2.436		887.7	0.755	845.1
2.244		883	0.678	843
2.047		878.3	0.485	837.3
160		3.998	861.2	1.644
	3.981	861.1	1.542	793.8
	3.805	856.5	1.538	793.7
	3.787	856.4	1.464	791.5
	3.621	852.2	1.457	791.2
	3.608	851.9	1.44	790.8
	3.588	851.3	1.344	787.7
	3.419	847.3	1.27	785.3
	3.23	842.3	1.264	785.1
	3.033	837	1.193	782.6
	2.826	831.3	1.147	781.3
	2.613	825.4	1.066	778.4
	2.434	820.4	1	776.3
	2.24	814.8	0.951	774.7
	2.043	809	0.872	772.1
	1.85	802.4	0.868	771.8
1.737	799.8	0.794	769.8	
1.655	797.3			
163	4	823.3	1.854	757.9
	3.806	818	1.792	755.7
	3.613	812.7	1.741	753.9
	3.422	807.3	1.735	753.8
	3.223	801.5	1.658	751.1
	3.024	795.5	1.592	748.6
	2.826	789.6	1.538	746.7
	2.632	783.7	1.459	743.8
	2.435	777.3	1.397	741.6
	2.244	771.2	1.344	739.7
	2.051	764.7	1.265	737.1

Table 9: Experimental data reported by Baidakov (continue)

Tables of experimental speed of sound measurements

T / K	p / MPa	$w / \text{m s}^{-1}$	p / MPa	$w / \text{m s}^{-1}$
167	3.995	769.5	2.121	702.2
	3.802	763.1	2.104	701.5
	3.616	757.2	2.071	700.2
	3.49	752.9	2.043	698.9
	3.423	750.6	2.038	698.7
	3.219	743.8	1.967	695.8
	3.036	737.1	1.892	692.5
	2.823	729.7	1.854	690.8
	2.632	722.2	1.776	687.7
	2.462	715.8	1.62	680.4
	2.435	714.9	1.547	677.2
	2.325	710.3	1.533	676.5
	2.267	708.2	1.52	675.8
	2.24	707.1	1.463	673.1
170	4	726.4	2.354	658.6
	3.81	719.3	2.279	655
	3.608	711.9	2.244	653.2
	3.412	704.2	2.2	651
	3.217	696.7	2.168	649.3
	3.027	688.8	2.161	649.1
	2.829	680.4	2.048	643.4
	2.629	671.4	1.936	637.5
	2.434	662.4		
173	4.001	680.2	2.513	607.3
	3.806	671.9	2.475	605
	3.61	663.2	2.436	602.6
	3.419	654.7	2.381	599.5
	3.221	645.2	2.357	597.9
	3.024	635.4	2.317	595.6
	2.824	624.9	2.282	593.7
	2.628	614	2.263	592.4
	2.553	609.6	2.944	544.9
177	4.003	612.2	2.942	544.8
	3.807	601.4	2.903	541.7
	3.617	590.4	2.864	538.7
	3.61	590	2.833	536.1
	3.414	578	2.804	533.6
	3.219	565	2.774	531.1
	3.023	551		
2.982	547.9			

Experimental data reported by Baidakov (continue)

T / K	p / MPa	$w / \text{m s}^{-1}$	p / MPa	$w / \text{m s}^{-1}$
180	4	553.3	3.338	500
	3.907	547	3.284	494.7
	3.808	540	3.258	492.1
	3.716	532.9	3.255	491.6
	3.613	524.3	3.225	488.8
	3.52	516.8	3.221	488.1
	3.416	507.4	3.182	483.7
	3.346	500.9	3.148	480.1
183	3.996	482.4	3.614	436.3
	3.977	481.2	3.61	435.8
	3.912	474.4	3.6	434.2
	3.808	462.1	3.585	432
	3.731	452.8	3.575	430.5
	3.69	447.1	3.558	427.7
	3.649	441.7	3.535	424.4

Experimental data reported by Baidakov

Technical drawings

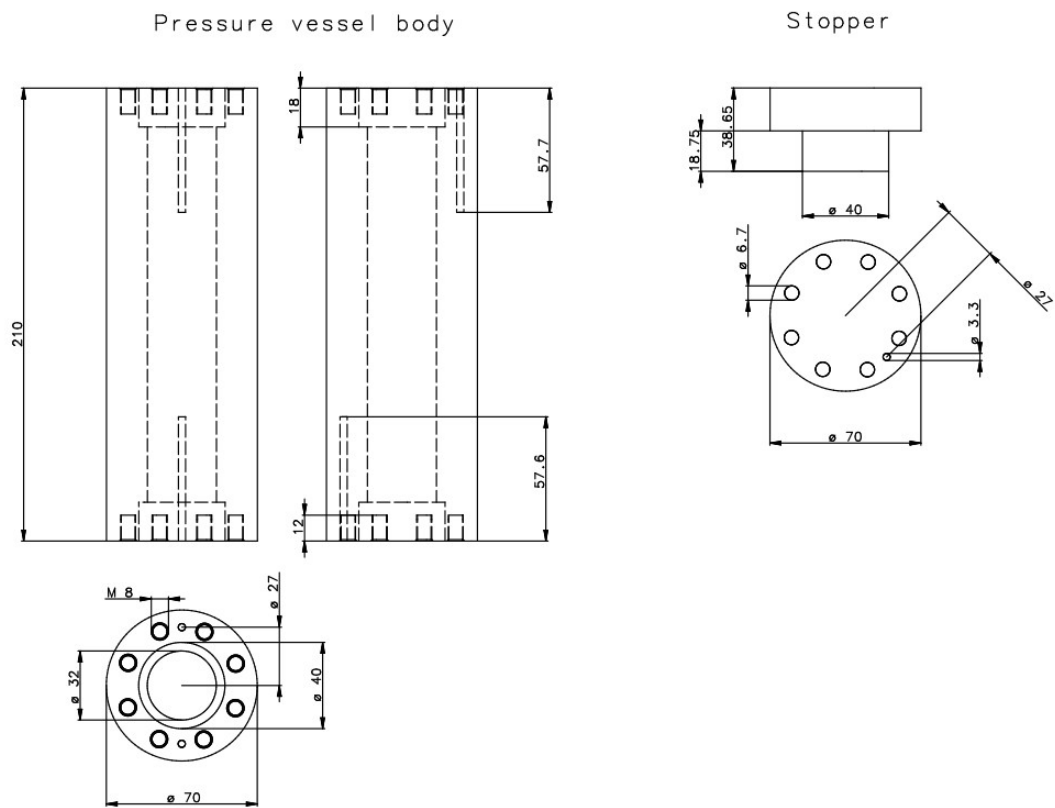


Figure 10: Schematics of the pressure vessel body and its two (upper and lower) stoppers.

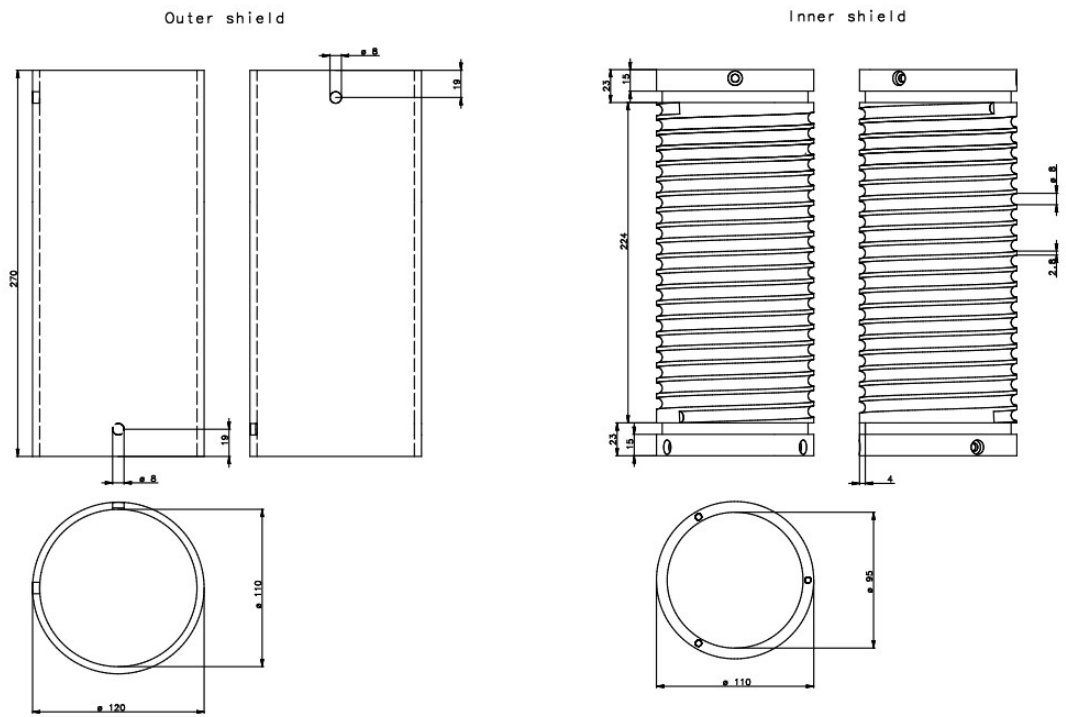


Figure 11: Schematics of the two components, the inner and the outer shields, that make up the aluminium exchanger.

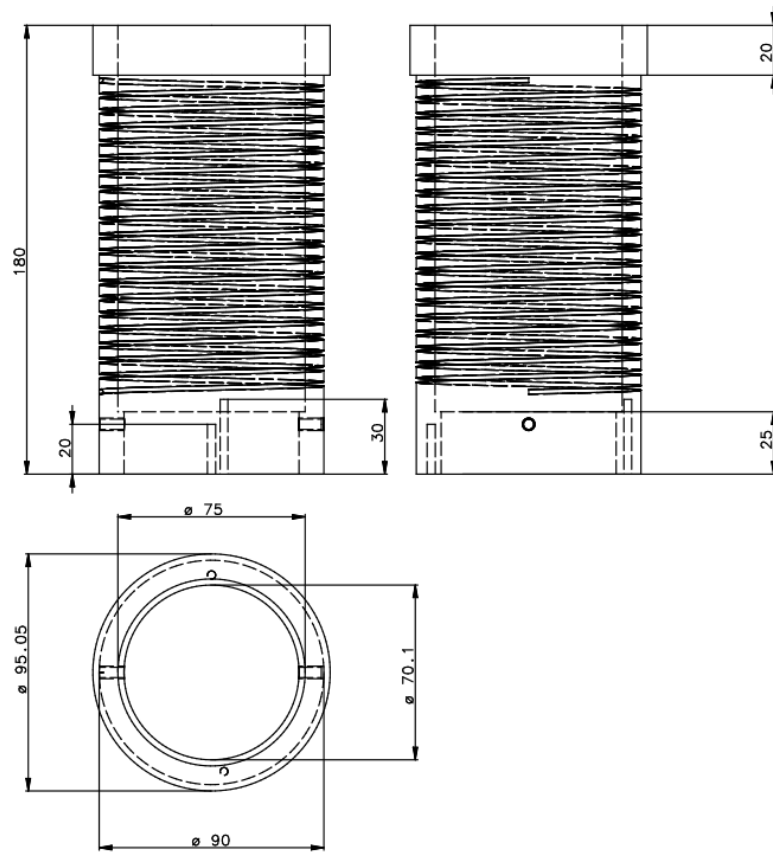


Figure 12: Schematics of the thermal shield used in the cryogenic apparatus.

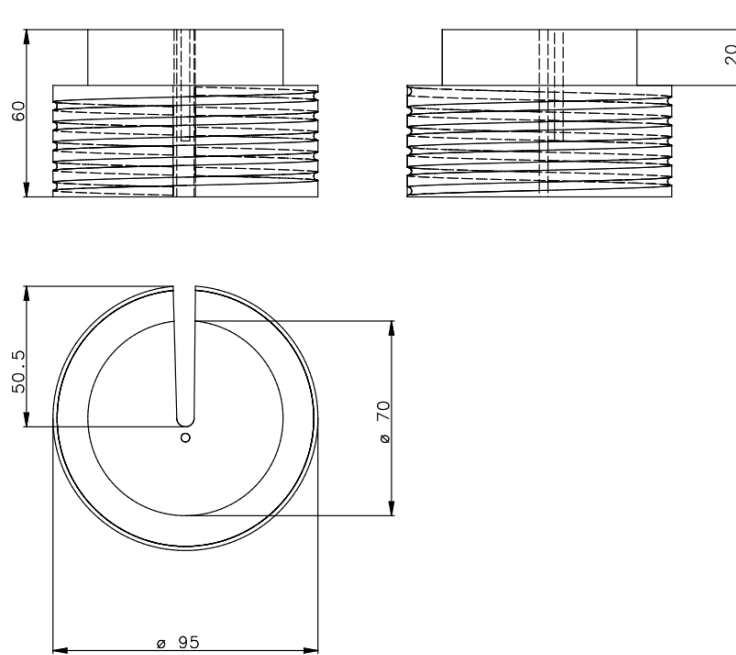


Figure 13: Schematics of the aluminium thermal bridge.

Bibliography

- [1] Selma Brynolf, Erik Fridell, and Karin Andersson. “Environmental assessment of marine fuels: liquefied natural gas, liquefied biogas, methanol and bio-methanol”. In: *Journal of cleaner production* 74 (2014), pp. 86–95.
- [2] Dave Seiler. “FUNDAMENTALS OF MULTIPATH ULTRASONIC FLOW METERS FOR LIQUID MEASUREMENT”. In: ().
- [3] Imelda S Caleon and R Subramaniam. “From Pythagoras to Sauveur: tracing the history of ideas about the nature of sound”. In: *Physics Education* 42.2 (2007), p. 173.
- [4] Otto Von Guericke. *The new (so-called) Magdeburg experiments of Otto von Guericke*. Vol. 137. Springer Science & Business Media, 2012.
- [5] Galileo Galilei. *Discorsi e dimostrazioni matematiche intorno a due nuove scienze attenenti alla meccanica ed i movimenti locali*. Gli Elsevirii, 1990.
- [6] Paolo Gozza. *Number to sound: the musical way to the scientific revolution*. Vol. 64. Springer Science & Business Media, 2000.
- [7] Luecha Ladachart. “Alternative frameworks in conceptions of sound: A historical evolution”. In: *JOURNAL OF EDUCATION KHON KAEN UNIVERSITY* 33.2 (2010), pp. 1–22.
- [8] Bernard S Finn. “Laplace and the Speed of Sound”. In: *Isis* 55.1 (1964), pp. 7–19.
- [9] Stan E Dosso and Jan Dettmer. “Studying the sea with sound”. In: *Proceedings of Meetings on Acoustics ICA2013*. Vol. 19. 1. ASA. 2013, p. 032001.
- [10] Ya Song Wei and Richard J Sadus. “Equations of state for the calculation of fluid-phase equilibria”. In: *AIChE Journal* 46.1 (2000), pp. 169–196.
- [11] Ivo Nezbeda. “On molecular-based equations of state: rigor versus speculations”. In: *Fluid phase equilibria* 182.1-2 (2001), pp. 3–15.
- [12] Andrzej Anderko. “Equation-of-state methods for the modelling of phase equilibria”. In: *Fluid phase equilibria* 61.1-2 (1990), pp. 145–225.
- [13] Jose O Valderrama. “The state of the cubic equations of state”. In: *Industrial & engineering chemistry research* 42.8 (2003), pp. 1603–1618.

- [14] Otto Redlich and Joseph NS Kwong. “On the thermodynamics of solutions. V. An equation of state. Fugacities of gaseous solutions.” In: *Chemical reviews* 44.1 (1949), pp. 233–244.
- [15] Giorgio Soave. “Equilibrium constants from a modified Redlich-Kwong equation of state”. In: *Chemical engineering science* 27.6 (1972), pp. 1197–1203.
- [16] Gerald G Fuller. “A modified Redlich-Kwong-Soave equation of state capable of representing the liquid state”. In: *Industrial & Engineering Chemistry Fundamentals* 15.4 (1976), pp. 254–257.
- [17] A Harmens and H Knapp. “Three-parameter cubic equation of state for normal substances”. In: *Industrial & Engineering Chemistry Fundamentals* 19.3 (1980), pp. 291–294.
- [18] G Schmidt and H Wenzel. “A modified van der Waals type equation of state”. In: *Chemical Engineering Science* 35.7 (1980), pp. 1503–1512.
- [19] Navin C Patel and Aryn S Teja. “A new cubic equation of state for fluids and fluid mixtures”. In: *Chemical Engineering Science* 37.3 (1982), pp. 463–473.
- [20] MA Trebble and PR Bishnoi. “Development of a new four-parameter cubic equation of state”. In: *Fluid Phase Equilibria* 35.1-3 (1987), pp. 1–18.
- [21] Yoshinori Adachi, Hidezumi Sugie, and Benjamin C-Y Lu. “Development of a five-parameter cubic equation of state”. In: *Fluid phase equilibria* 28.2 (1986), pp. 119–136.
- [22] André Pénélox, Evelyne Rauzy, and Richard Fréze. “A consistent correction for Redlich-Kwong-Soave volumes”. In: *Fluid phase equilibria* 8.1 (1982), pp. 7–23.
- [23] Ulrich Setzmann and Wolfgang Wagner. “A new equation of state and tables of thermodynamic properties for methane covering the range from the melting line to 625 K at pressures up to 100 MPa”. In: *Journal of Physical and Chemical reference data* 20.6 (1991), pp. 1061–1155.
- [24] E Bender. “Equation of State Exactly Representing The Phase Behaviors of Pure Substances”. In: *Proc. 5th Symposium on Thermophysical Properties. Am. Soc. Of Mech. Eng.* 1970, pp. 227–235.
- [25] Robert Daniels Goodwin. *The thermophysical properties of methane, from 90 to 500 K at pressures to 700 bar*. Vol. 653. National Bureau of Standards, 1974.
- [26] RD McCarty. “A modified Benedict-Webb-Rubin equation of state for methane using recent experimental data”. In: *Cryogenics* 14.5 (1974), pp. 276–280.
- [27] Selby Angus, Barrie Armstrong, and KM De Reuck. “International thermodynamic tables of the fluid state. 5. methane”. In: (1978).

- [28] VV Sytchev and GA Spiridonov. "JOINT PROCEEDINGS OF THERMAL, CALORICAL AND ACOUSTICAL EXPERIMENTAL DATA FOR COMPILATION OF THERMODYNAMIC TABLES". In: *Data for Science and Technology*. Elsevier, 1981, pp. 369–370.
- [29] James F Ely and HJM Hanley. "Prediction of transport properties. 1. Viscosity of fluids and mixtures". In: *Industrial & Engineering Chemistry Fundamentals* 20.4 (1981), pp. 323–332.
- [30] Uwe Sievers. "Die thermodynamischen Eigenschaften von Kohlendioxid". In: *Forschung im Ingenieurwesen* 50.6 (1984), pp. 192–192.
- [31] DD Erickson and TW Leland. "Application of critical-region scaling to pure-component equations of state". In: *International Journal of Thermophysics* 7.4 (1986), pp. 911–922.
- [32] BA Younglove and James F Ely. "Thermophysical properties of fluids. II. Methane, ethane, propane, isobutane, and normal butane". In: *Journal of Physical and Chemical Reference Data* 16.4 (1987), pp. 577–798.
- [33] DS Kurumov, GA Olchowy, and JV Sengers. "Thermodynamic properties of methane in the critical region". In: *International journal of thermophysics* 9.1 (1988), pp. 73–84.
- [34] Daniel G Friend, James F Ely, and Hepburn Ingham. "Thermophysical properties of methane". In: *Journal of Physical and Chemical Reference Data* 18.2 (1989), pp. 583–638.
- [35] Robert D Goodwin and R Pyrdz. "Densities of compressed liquid methane, and the equation of state". In: *Journal of Research of the National Bur Stand* 76.Section A (1972).
- [36] Donald R Douslin et al. "P-V-T Relations for Methane". In: *Journal of Chemical & Engineering Data* 9.3 (1964), pp. 358–363.
- [37] VM CHENG and WB Daniels. "MELTING PARAMETERS OF METHANE AND NITROGEN AT HIGH-PRESSURE". In: *BULLETIN OF THE AMERICAN PHYSICAL SOCIETY*. Vol. 17. 3. AMER INST PHYSICS CIRCULATION FULFILLMENT DIV, 500 SUNNYSIDE BLVD, WOODBURY ... 1972, p. 359.
- [38] Rx Kleinrahm and W Wagner. "Measurement and correlation of the equilibrium liquid and vapour densities and the vapour pressure along the coexistence curve of methane". In: *The Journal of Chemical Thermodynamics* 18.8 (1986), pp. 739–760.
- [39] R Kleinrahm, W Duschek, and W Wagner. "(Pressure, density, temperature) measurements in the critical region of methane". In: *The Journal of Chemical Thermodynamics* 18.12 (1986), pp. 1103–1114.

- [40] W Duschek et al. "Measurement and correlation of the (pressure, density, temperature) relation of nitrogen in the temperature range from 273.15 to 323.15 K at pressures up to 8 MPa". In: *The Journal of Chemical Thermodynamics* 20.9 (1988), pp. 1069–1077.
- [41] U Setzmann and W Wagner. "A new method for optimizing the structure of thermodynamic correlation equations". In: *International Journal of Thermophysics* 10.6 (1989), pp. 1103–1126.
- [42] BE Gammon and DR Douslin. "The velocity of sound and heat capacity in methane from near-critical to subcritical conditions and equation-of-state implications". In: *The Journal of Chemical Physics* 64.1 (1976), pp. 203–218.
- [43] GC Straty. "Velocity of sound in dense fluid methane". In: *Cryogenics* 14.7 (1974), pp. 367–370.
- [44] A Van Itterbeek et al. "Sound velocity measurements in liquid methane as a function of pressure". In: *Physica* 35.1 (1967), pp. 162–166.
- [45] VG Baidakov, AM Kaverin, and VP Skripov. "Measurement of ultrasonic speed in stable and metastable liquid methane". In: *The Journal of Chemical Thermodynamics* 14.11 (1982), pp. 1003–1010.
- [46] Wolfgang Lemming. *Experimentelle Bestimmung akustischer und thermischer Virialkoeffizienten von Arbeitsstoffen der Energietechnik*. VDI-Verlag, 1989.
- [47] E Terres, W Jahn, and H Reissmann. "On the knowledge of the determination of adiabatic exponents of low boiling hydrocarbons at different pressures and temperatures by measurements of the ultrasonic velocity". In: *Brennst.-Chem* 38 (1957), pp. 129–160.
- [48] W Van Dael et al. "Sound velocity measurements in liquid methane". In: *Physica* 31.11 (1965), pp. 1643–1648.
- [49] GC Straty. "Hypersonic velocities in saturated and compressed fluid methane". In: *Cryogenics* 15.12 (1975), pp. 729–731.
- [50] PJ Kortbeek and JA Schouten. "Measurements of the compressibility and sound velocity in methane up to 1 GPa, revisited". In: *International journal of thermophysics* 11.3 (1990), pp. 455–466.
- [51] A Sivaraman and Bruce E Gammon. "Speed-of-sound measurements in natural gas fluids". In: *Final Report, 1 Oct. 1984-31 Jan. 1986 IIT Research Inst., Bartlesville, OK. National Inst. for Petroleum and Energy Research*. (1986).
- [52] Anthony Robert Holmes Goodwin. "Thermophysical properties from the speed of sound". PhD thesis. University of London, 1988.
- [53] Oliver Kunz and Wolfgang Wagner. "The GERG-2008 wide-range equation of state for natural gases and other mixtures: an expansion of GERG-2004". In: *Journal of chemical & engineering data* 57.11 (2012), pp. 3032–3091.

- [54] Oliver Kunz et al. “The GERG-2004 wide-range equation of state for natural gases and other mixtures”. In: *GERG TM15*. Vol. 6. Fortschritt-Berichte VDI, 2007.
- [55] Manfred Jaeschke et al. “GERG Project: Wide-range reference equation of state for natural gases”. In: *GAS UND WASSERFACH GAS ERDGAS* 144.7/8 (2003), pp. 430–430.
- [56] Reinhard Klimeck. *Entwicklung einer Fundamentalgleichung für Erdgase für das Gas- und Flüssigkeitsgebiet sowie das Phasengleichgewicht*. na, 2000.
- [57] Ding-Yu Peng and Donald B Robinson. “A new two-constant equation of state”. In: *Industrial & Engineering Chemistry Fundamentals* 15.1 (1976), pp. 59–64.
- [58] RD McCarty. “Mathematical models for the prediction of liquefied-natural-gas densities”. In: *The Journal of Chemical Thermodynamics* 14.9 (1982), pp. 837–854.
- [59] Kenneth E Starling and Jeffrey L Savidge. *Compressibility factors of natural gas and other related hydrocarbon gases*. AGA, American Gas Association, 1994.
- [60] Eric W Lemmon and Richard T Jacobsen. “A new functional form and new fitting techniques for equations of state with application to pentafluoroethane (HFC-125)”. In: *Journal of physical and chemical reference data* 34.1 (2005), pp. 69–108.
- [61] F Peleties et al. “Thermodynamic properties and equation of state of liquid diisodecyl phthalate at temperature between (273 and 423) K and at pressures up to 140 MPa”. In: *The Journal of Chemical Thermodynamics* 42.5 (2010), pp. 631–639.
- [62] Lance A Davis and Robert B Gordon. “Compression of mercury at high pressure”. In: *The journal of chemical physics* 46.7 (1967), pp. 2650–2660.
- [63] Martin Trusler. *Physical acoustics and metrology of fluids*. CRC Press, 1991.
- [64] Michael R Moldover et al. “Measurement of the universal gas constant R using a spherical acoustic resonator”. In: *Physical review letters* 60.4 (1988), p. 249.
- [65] RM Gavioso et al. “Progress in INRiM experiment for the determination of the Boltzmann constant with a quasi-spherical resonator”. In: *International Journal of Thermophysics* 32.7-8 (2011), p. 1339.
- [66] RM Gavioso et al. “A determination of the Boltzmann constant from speed of sound measurements in helium at a single thermodynamic state”. In: *Metrologia* 47.4 (2010), p. 387.

- [67] Michael R Moldover et al. “Acoustic gas thermometry”. In: *Metrologia* 51.1 (2014), R1.
- [68] Emmanuel P Papadakis. “Ultrasonic velocity and attenuation: Measurement methods with scientific and industrial applications”. In: *Physical acoustics*. Vol. 12. Elsevier, 1976, pp. 277–374.
- [69] Emmanuel P Papadakis. “New, compact instrument for pulse-echo-overlap measurements of ultrasonic wave transit times”. In: *Review of Scientific Instruments* 47.7 (1976), pp. 806–813.
- [70] PJ Kortbeek et al. “Apparatus for sound velocity measurements in gases up to 10 kbar: Experimental data for argon”. In: *Review of scientific instruments* 56.6 (1985), pp. 1269–1273.
- [71] SJ Ball and JPM Trusler. “Speed of Sound of n-Hexane and n-Hexadecane at Temperatures Between 298 and 373 K and Pressures up to 100 MPa”. In: *International journal of thermophysics* 22.2 (2001), pp. 427–443.
- [72] Anthony Goodwin, KN Marsh, and WA Wakeham. *Measurement of the thermodynamic properties of single phases*. Vol. 6. Elsevier, 2003.
- [73] Wolfgang Wagner and Andreas Pruß. “The IAPWS formulation 1995 for the thermodynamic properties of ordinary water substance for general and scientific use”. In: *Journal of physical and chemical reference data* 31.2 (2002), pp. 387–535.
- [74] Robert Joseph Corruccini and John J Gniewek. *Thermal expansion of technical solids at low temperatures: a compilation from the literature*. 29. US Dept. of Commerce, National Bureau of Standards, 1961.
- [75] Alessandro Volta, marchese Francesco Castelli, and Carlo Giuseppe Campi. *Lettere: sull’aria infiammabile nativa delle paludi*. Giuseppe Marelli, 1777.
- [76] Oliver Kuhn. “Ancient Chinese drilling”. In: *Canadian Society of Exploration Geophysicists Recorder* 29.6 (2004), pp. 39–43.
- [77] C Zhang and J Huang. “Drilling and Gas Recovery Technology in Ancient China”. In: *Zigong Salt Industry Museum, Zigong* 44 (1997).
- [78] Harold Baily Dixon, Colin Campbell, and A Parker. “On the velocity of sound in gases at high temperatures, and the ratio of the specific heats”. In: *Proceedings of the Royal Society of London. Series A, Containing Papers of a Mathematical and Physical Character* 100.702 (1921), pp. 1–26.
- [79] A Van Itterbeek and L Verhaegen. “Measurements of the velocity of sound in liquid argon and liquid methane”. In: *Proceedings of the Physical Society. Section B* 62.12 (1949), p. 800.
- [80] W Van Dael et al. “Sound velocity measurements in liquid methane”. In: *Physica* 31.11 (1965), pp. 1643–1648.

- [81] A Van Itterbeek and W Van Dael. “Velocity of sound in liquid oxygen and liquid nitrogen as a function of temperature and pressure”. In: *Physica* 28.9 (1962), pp. 861–870.
- [82] Frederick G Keyes, Leighton B Smith, and David B Joubert. “The Equation of State for Methane Gas Phase”. In: *Journal of Mathematics and Physics* 1.4 (1922), pp. 191–210.
- [83] Yu P Blagoi et al. “VELOCITY OF SOUND IN LIQUID KRYPTON XENON AND METHANE”. In: *RUSSIAN JOURNAL OF PHYSICAL CHEMISTRY, USSR* 41.7 (1967), p. 908.
- [84] James R Singer. “Excess ultrasonic attenuation and volume viscosity in liquid methane”. In: *The Journal of Chemical Physics* 51.11 (1969), pp. 4729–4733.
- [85] Donald G Naugle. “Excess Ultrasonic Attenuation and Intrinsic-Volume Viscosity in Liquid Argon”. In: *The Journal of Chemical Physics* 44.2 (1966), pp. 741–744.
- [86] BA Younglove. “Speed of sound in fluid parahydrogen”. In: *The Journal of the Acoustical Society of America* 38.3 (1965), pp. 433–438.
- [87] H Preston-Thomas. “The international temperature scale of 1990 (ITS-90)”. In: *metrologia* 27.1 (1990), p. 3.
- [88] A Van Itterbeek et al. “A sensitive design for pressure measurements up to 3,000 kg/cm²”. In: *Cryogenics* 5 (1965), pp. 85–88.
- [89] EW Lemmon, ML Huber, and MO McLinden. “NIST Standard Reference Database 23, Reference Fluid Thermodynamic and Transport Properties (REFPROP), version 9.0, National Institute of Standards and Technology”. In: *R1234yf. fld file dated December 22* (2010), p. 2010.
- [90] Markus Richter et al. “Development of a special single-sinker densimeter for cryogenic liquid mixtures and first results for a liquefied natural gas (LNG)”. In: *The Journal of Chemical Thermodynamics* 93 (2016), pp. 205–221.
- [91] W Wagner and R Kleinrahm. “Densimeters for very accurate density measurements of fluids over large ranges of temperature, pressure, and density”. In: *Metrologia* 41.2 (2004), S24.
- [92] Mark O McLinden, R Kleinrahm, and W Wagner. “Force transmission errors in magnetic suspension densimeters”. In: *International journal of thermophysics* 28.2 (2007), pp. 429–448.
- [93] Monika Thol et al. “EOS-LNG: A Fundamental Equation of State for the Calculation of Thermodynamic Properties of Liquefied Natural Gases”. In: *Journal of Physical and Chemical Reference Data* 48.3 (2019), p. 033102.

BIBLIOGRAPHY

- [94] GH Thomson, KR Brobst, and RW Hankinson. “An improved correlation for densities of compressed liquids and liquid mixtures”. In: *AIChE journal* 28.4 (1982), pp. 671–676.
- [95] Christopher Tietz et al. “Enhancement of the revised Klosek and McKinley method for density calculations of liquefied natural gas (LNG) over the temperature range from (100 to 135) K at pressures up to 10 MPa”. In: *Fuel Processing Technology* 165 (2017), pp. 19–26.
- [96] RD McCarty. “Mathematical models for the prediction of liquefied-natural-gas densities”. In: *The Journal of Chemical Thermodynamics* 14.9 (1982), pp. 837–854.

This Ph.D. thesis has been typeset by means of the T_EX-system facilities. The typesetting engine was pdfL^AT_EX. The document class was `toptesi`, by Claudio Beccari, with option `tipotesi=scudo`. This class is available in every up-to-date and complete T_EX-system installation.